UNIVERSIDADE DE LISBOA
FACULDADE DE CIÊNCIAS
DEPARTAMENTO DE FÍSICA

Growth and Characterization of Low Dimensional Mo Selenide

Carolina de Almeida Marques

Mestrado em Física
Física da Matéria Condensada e Nano-Materiais

Dissertação orientada por:
Olinda Maria Quelhas Fernandes Conde

2016

Acknowledgments

À Prof. Olinda Conde, por me ter recebido no laboratório e ter aceite ser minha orientadora, por ter acreditado em mim desde o início, pela confiança e por estar sempre disponível para dúvidas, discussões e partilha de conhecimentos, sem as quais esta tese não seria possível.

Ao Prof. António Silvestre, pela ajuda na montagem da instalação experimental e pelo constante interesse no meu trabalho.

À Prof. Ana Viana, pelas medidas de microscopia de força atómica (AFM) e pela constante disponibilidade e amizade.

Ao Prof. Luís Santos, Instituto Superior Técnico, pelas medidas de espectroscopia Raman, pelas longas horas no laboratório e partilha de ideias.

À Prof. Maria de Jesus Gomes, Centro de Física da Universidade do Minho, por me ter recebido e facilitado o acesso ao uso do equipamento de fotoluminescência. Ao Zé Pedro Silva, por ter realizado as medidas de fotoluminescência, pelas discussões de resultados, partilha de ideias e conselhos.

À Prof. Olinda Monteiro, por me ter facilitado o acesso ao seu laboratório para a utilização da balança, necessária para a pesagem dos pós de MoO_3 e selénio.

Aos meus pais, por me apoiarem e incentivarem sempre, por acreditarem em mim, e por toda a confiança e paciência. Aos meus avós, por estarem presentes e acreditarem que sou capaz. À minha irmã, por tudo e mais alguma coisa, por me ouvir, pela partilha de experiências, pela constante preocupação e pelas tardes a ver séries no sofá. Ao Zé Miguel, pelos conselhos por telefone e pela paciência para me ouvir.

À Isabel, ao Bifídos e à Ana Patrícia, que sempre estiveram presentes, por compreenderem as minhas ausências, pelos desabafos, brincadeiras, e por tudo o que partilhámos. Ao Vitorino e ao Carlos, pelos almoços, cafés e conversas, que foram sempre enriquecedoras. Ao Tiago, Bernardo, Patrícia F., Cláudio, Patrícia M. e Libório, sem os quais o caminho até aqui teria sido muito mais difícil.

Ao Brito, por olhar sempre para o lado positivo das coisas, por nunca me deixar ir a baixo, por tudo.

Abstract

The fascinating properties of graphene make it the perfect material for the development of new technological applications. The fast progress in the study of graphene and the absence of a bandgap has led to the exploration of other layered materials that could be thinned down to one atomic/molecular layer, like the transition metal dichalcogenides (TMD).

Two-dimensional semiconductor TMD, such as MoS_2, WS_2 and $MoSe_2$, have recently attracted great attention due to their direct band gap, high electron mobility and strong spin-valley coupling, which makes them ideal for low dimension electronic and optoelectronic applications. Chemical Vapour Deposition (CVD) has been reported to enable the deposition of $MoSe_2$ monolayers on SiO_2/Si substrates, with high crystallinity and excellent electronic properties. However, the low chemical reactivity of Se makes the optimisation of CVD parameters as well as the formation of large-area continuous monolayer films challenging. Moreover, the reproducibility of experiments is not efficient in different CVD reactors, which is crucial for the applications of such layers.

In this work, mono- to few-layer $MoSe_2$ nanofilms were synthesised onto SiO_x/Si substrates by CVD, using MoO_3 and Se powders as solid precursors. The experiments were carried out at atmospheric pressure, using Ar as the carrier gas and H_2 as the reducing agent. Different deposition parameters were studied, such as the substrate position, the mass of the precursors and the gas flow rate, in order to understand the influence of each one on the quality of the $MoSe_2$ nanolayers produced. The samples were analysed by X-ray diffraction (XRD), Raman spectroscopy, scanning electron microscopy (SEM), atomic force microscopy (AFM) and photoluminescence (PL). The obtained results indicate that the quality of the samples strongly depends on the concentration of H_2 in the gas phase, the Mo:Se ratio at the substrate surface, the gas flow rate and the uniformity of the deposition temperature along the substrate length.

Keywords: transition metal dichalcogenides, molybdenum diselenide, two-dimensional materials, chemical vapour deposition

Resumo

A descoberta do grafeno por Novoselov *et al.*, em 2004, revelou que uma camada atómica de átomos de carbono apresenta propriedades elétricas, óticas e mecânicas excecionais, não observadas na grafite. Desde então, ficou estabelecido que as formas bidimensionais (2D) dos materiais podem ser termodinamicamente estáveis e que apresentam novas e extraordinárias propriedades, distintas da sua forma tridimensional (3D). Esta descoberta, incentivou investigadores por todo o mundo a procurar outros materiais que pudessem ser produzidos na sua forma 2D, em busca de novos fenómenos.

Os dicalcogenetos de metais de transição (TMD), de fórmula química MX_2, com M um metal de transição e X um calcogénio, formam estruturas em camadas, tipo grafite. Nos cristais de TMD, uma camada é formada por um plano de átomos M, dispostos numa rede hexagonal, entre dois planos de átomos X, ligados entre si por ligações covalentes fortes, na forma X-M-X. Diferentes camadas interagem entre si por forças de van der Waals fracas, e como tal, é possível retirar uma camada 2D do cristal macroscópico, isolando-a de modo a estudar as suas propriedades. Dependendo do metal de transição e do calcogénio envolvidos, as suas propriedades elétricas podem ser as de um semicondutor (e. g. $MoSe_2$, WS_2), um metal (e.g. $NbTe_2$) ou mesmo de um supercondutor (e.g. $NbSe_2$, TaS_2).

Recentemente, os TMD semicondutores (com $M = Mo, W$ e $X = S, Se$), têm sido foco de investigação devido à presença de hiato de energia finito, cuja natureza depende do número de camadas que constituem o material. À medida que o número de camadas diminui, a estrutura de bandas de energia do TMD altera-se devido a efeitos de confinamento quântico, de modo que o hiato de energia indireto presente no material macroscópico se transforma num hiato de energia direto na monocamada. Adicionalmente, a quebra das simetrias de inversão espacial nestas monocamadas, juntamente com o acoplamento spin-órbita, são responsáveis pelo aparecimento de um novo grau de liberdade chamado de vale. Controlando o vale que é ocupado, este tipo de material vai permitir o desenvolvimento de um novo tipo de eletrónica, a eletrónica de vale, à semelhança do controlo do spin do eletrão na eletrónica de spin.

Ao contrário do grafeno, que apresenta um hiato de energia nulo, as monocamadas de TMD semicondutores apresentam um hiato de energia finito, com valores entre 1 e 2 eV, comparáveis ao hiato do silício. Deste modo, os TMD semicondutores 2D são alternativas realistas ao silício em nanoeletrónica, sendo promissores como partes integrantes em dispositivos eletrónicos e optoelectrónicos, tais como, transístores de efeito de campo, foto-detetores, células fotovoltaicas e díodos emissores de luz. A fabricação destes dispositivos utilizando apenas como partes integrantes materiais 2D irá permitir o desenvolvimento de dispositivos de elevado desempenho e tão finos quanto possível.

Os métodos de exfoliação, primeiramente utilizados para a produção de grafeno, como a exfoliação mecânica e a exfoliação química, produzem camadas 2D muito cristalinas e com excelentes propriedades, ideiais para a sua caracterização fundamental. No entanto, estes métodos apresentam limitações no controlo do número de camadas retirado e no tamanho lateral destas, tipicamente $\leq 10 \mu m$, não sendo adequados para aplicações tecnológicas. Portanto, outros métodos têm de ser desenvolvidos na tentativa de se estabelecer uma abordagem fiável capaz de produzir camadas 2D de elevados tamanhos laterais,

necessário para o desenvolvimento de produtos a nível industrial. Nos últimos anos, a deposição química em fase vapor (CVD) tem-se mostrado um método capaz de produzir grafeno e monocamadas de nitreto de boro com áreas que podem ir até vários centímetros quadrados, sobre folhas de cobre ou alumínio. Mais recentemente, o CVD tem sido anunciado como sendo capaz de sintetizar, com sucesso, monocamadas de MoS_2, $MoSe_2$, WS_2 e WSe_2, com tamanhos laterais até vários micrómetros, sobre diversos substratos, tais como, SiO_2/Si, safira e mica. Atualmente, o CVD é o método mais promissor para a produção de monocamadas de TMD de grande área e de elevada qualidade, dizendo-se que as características das camadas depositadas, tais como, o número de camadas e os seus tamanhos laterais, poderão vir a ser rigorosamente controladas através da otimização dos parâmetros de deposição de uma experiência CVD.

Até ao momento, o TMD semicondutor mais estudado e produzido por CVD foi o MoS_2, cujos parâmetros de deposição de CVD estão otimizados para a produção de monocamadas cristalinas de elevada qualidade, com dimensões laterais superiores a $50\mu m$. Comparado com a monocamada de MoS_2, que tem um hiato direto de 1.9eV, a monocamada de $MoSe_2$, tem um hiato direto de 1.5 eV, mais próximo do valor de hiato ideal necessário para aplicações relacionadas com o espectro solar, tal como células fotovoltaicas. Apresenta uma maior energia de desdobramento no topo da banda de valência devido ao spin ($\sim 180meV$), o que o torna num material mais interessante do que o MoS_2 para eletrónica de spin. Adicionalmente, $MoSe_2$ constituído por poucas camadas ($\sim$ 10 camadas) tem os hiatos de energia indireto e direto quase degenerados, pelo que um aumento de temperatura, pode efetivamente levar o sistema de poucas camadas para o limite 2D, apresentando hiato direto. No entanto, a síntese de monocamadas de $MoSe_2$ com elevadas dimensões laterais por CVD, é mais desafiante que a síntese de monocamadas de MoS_2 devido à mais baixa reatividade química do selénio em relação ao enxofre. Isto implica que seja necessário mais tempo de deposição para a produção de monocamadas de $MoSe_2$ de elevados tamanhos laterais, o que inevitavelmente leva à deposição de filmes mais espessos. Atualmente, a otimização dos parâmetros experimentais de CVD para a produção de monocamadas de $MoSe_2$ de grandes dimensões laterais ainda precisa de ser alcançada. É necessário estudar cuidadosamente a influência de cada parâmetro de deposição nas características das camadas depositadas, de modo a que os mecanismos de crescimento sejam compreendidos, de forma a tornar o CVD num método viável na produção destas camadas 2D.

Neste trabalho, nanofilmes de $MoSe_2$ com espessuras de uma ou algumas camadas foram sintetizados por CVD, sobre substratos de SiO_x/Si, utilizando pós de MoO_3 e Se como percursores sólidos. As experiências foram realizadas à pressão atmosférica, utilizando Ar como gás de arraste e H_2 como agente redutor. Diferentes parâmetros experimentais foram estudados, numa tentativa de se compreender a influência de cada parâmetro nas propriedades dos nanofilmes de $MoSe_2$ produzidos. As amostras foram caracterizadas por microscopia ótica, microscopia eletrónica de varrimento, difração de raios-X, espectroscopia Raman, microscopia de força atómica e fotoluminescência (PL). Os resultados obtidos indicam que as características dos nanofilmes produzidos dependem fortemente da percentagem de H_2 na fase gasosa, da razão $Mo : Se$ à superfície do substrato e da taxa do fluxo de gás.

A oxidação de substratos de silício com diferentes espessuras de óxido também foi realizada no âmbito do presente trabalho. Inesperadamente, descobriu-se que os substratos de SiO_x/Si possuem um pico PL, de elevada intensidade, no mesmo comprimento de onda reportado para as monocamadas e algumas camadas de $MoSe_2$, para um comprimento de onda de excitação (λ_{ex}) de 532nm. Observou-se que este pico PL diminui de intensidade com o aumento da espessura da camada de óxido. Além disso, observou-se que o pico se desloca para comprimentos de onda menores com o aumento da energia de excitação. Assim, estudou-se o PL dos substratos de SiO_x/Si para quatro λ_{ex} diferentes, concluindo-se

que para $\lambda_{ex} = 514.5nm$ o pico PL se encontra suficientemente deslocado para comprimentos de ondas menores de modo a permitir o acesso à resposta PL das nanocamadas de $MoSe_2$. Para compreender a origem do PL nos substratos de SiO_x/Si, foram estudados filmes finos de silício amorfo sobre substratos de sílica fundida e de MgO. Os resultados sugerem que o PL é originado em estados na interface óxido de silício-silício.

Palavras-chave : dicalcogenetos de metais de transição, diseleneto de molibdénio, materiais bidimensionais, deposição química a partir da fase vapor

Contents

List of Tables

List of Figures

List of Abbreviations

2D	Two-dimensional
AFM	Atomic force microscopy
a-Si	Amorphous silicon
CBM	Conduction band minimum
CVD	Chemical vapour deposition
DFT	Density functional theory
FEG-SEM	Field emission gun - Scanning electron microscopy
FET	Field-effect transistor
FWHM	Full width at half maximum
$Mo-zz$	Molybdenum zigzag terminations
OM	Optical microscopy
PL	Photoluminescence
PLD	Pulsed laser deposition
sccm	Standard cubic centimetres per minute
$S-zz$	Sulphur zigzag terminations
TMD	Transition metal dichalcogenides
VBM	Valence band maximum
XRD	X-ray diffraction

List of Symbols

A_t	Cross-sectional area of the quartz tube
β	X-ray peak width
B	Parabolic constant
B/A	Linear constant
C	Equilibrium concentration of the oxidant in the bulk gas phase
$\delta(x)$	Boundary layer thickness
$\bar{\delta}$	Average boundary layer thickness
$\Delta(2\theta)$	Displacement length of the sample in relation to the centre of the goniometer
$\Delta(T)$	Degree of supercooling
d	Quartz tube diameter
d_{hkl}	Spacing between planes of the same *hkl* family
E_{ex}	Excitation energy
ϕ	Total gas flow rate
ϕ_{Ar}	Argon flow rate
ϕ_{H_2}	H_2 flow rate
ϕ_i	Phase shift
h	Gas-phase transport coefficient
I	Intensity
κ	Thermal conductivity
k	Chemical reaction rate constant
K	Crystalline shape constant
K_n	Knudsen number
$\bar{l}$	Mean free path
λ	Wavelength
λ_{ex}	Excitation wavelength
L	Characteristic length
μ	Viscosity of the vapour
M	Transition metal
N	Number of oxidant molecules per unit volume
n	Order of reflection
n_i	Complex refractive index
ω_0	Frequency of Raman vibrational mode
ω_i	Frequency of incident light
P_0	Standard pressure
P	Pressure

ρ	Mass density of the vapour
R	Goniometer radius
Re_L	Reynolds number
Re_x	Reynolds number calculated at position x on substrate surface
σ	Electrical conductivity
τ	Time correction parameter
$< \tau >$	Average crystallite size
θ	Angle of incidence
t	Oxidation time
T_0	Standard temperature
T	Temperature
T_e	Equilibrium temperature
$\bar{u}$	Average velocity of the carrier gas
X	Chalcogenide
x_i	Initial oxide thickness
x_{ox}	Oxide thickness

Chapter 1

Introduction

The isolation of graphene by Novoselov *et al.* in 2004 [1], not only was the first experimental evidence that atomically thin layers can be thermodynamically stable, but also unveiled outstanding new physical properties intrinsic of two-dimensional (2D) materials. These properties, not observed in graphite, inspired researchers worldwide to search for new materials that could be thinned down to one atomic/molecular layer.

Transition metal dichalcogenides (TMD) are a class of layered materials with chemical formula MX_2, where M is a transition metal and X is a chalcogen. In these materials, each layer is composed of a plane of M atoms sandwiched between two planes of X atoms by covalent bonding, and different layers are vertically stacked by van der Waals interactions [2]. Hence, just like graphite, they can be exfoliated down to a monolayer, exhibiting new properties that are absent in the bulk crystal. Depending on the metal and chalcogen involved, their electrical properties can be those of a semiconductor (e.g. $MoSe_2$, WS_2), a metal (e.g. $NbTe_2$) or even a superconductor (e.g. $NbSe_2$, TaS_2) [3].

Recently, low-dimensional semiconductor TMDs (with M=Mo, W and X=S, Se) have attracted much attention due to their tunable electronic properties dependent upon the number of layers in the material. As the number of layers decreases, the band structure of the TMD changes so that the indirect band gap in bulk and few-layer TMD crystals transforms into a direct band gap in the monolayer. Furthermore, in monolayer TMD, the breaking of inversion symmetry together with the spin-orbit interaction results in the coupling of spin and valley physics [2]. By manipulating the spin and valley degrees of freedom, a new type of electronics, called *valleytronics*, can be developed in analogy with the manipulation of the spin in *spintronics*.

Unlike graphene, which has a zero band gap and to which the introduction of a sizeable one is a difficult task, the presence of a sizeable bandgap in monolayer semiconductor TMD, in the range 1-2eV, makes them a realistic alternative to silicon for future nanoelectronic applications. The previous properties makes them promising as active layers in logic electronic and optoelectronic devices, such as field-effect transistors (FET) [4, 5], photodetectors [2, 6, 7], photovoltaic cells [8, 9] and light-emitting diodes [10, 11]. Additionally, they are efficient catalysts that are suitable for hydrogen evolution reaction [12, 13].

Exfoliation methods, such as mechanical and chemical exfoliation, enable the production of 2D layers with a high degree of crystallinity, ideal for the fundamental characterization of their intrinsic properties. However, these methods present limitations on the control of the thickness of the flakes produced as well as on their lateral sizes, that are typically $\leq 10\mu m$, not suited for technological applications. Therefore, other experimental methods have been used, such as molecular beam epitaxy, physical vapour deposition and chemical vapour deposition (CVD), in an attempt to achieve a reliable and scalable approach to the production of large-scale 2D materials, necessary for product development on an industrial level. For the past few years, CVD has proven to successfully produce graphene [14] and boron nitride [15] monolayers with areas up to several square centimetres on copper and platinum foils. More recently, CVD has also been reported to successfully grow low-dimensional layers of MoS_2 [16–18], $MoSe_2$ [2, 19–21], WS_2 [22] and WSe_2 [23, 24], with lateral sizes up to several micrometers, on various substrates, such as SiO_2/Si, sapphire and mica substrates. Currently, it is the most promising method for the production of large-area TMD monolayers of high quality, allowing for a careful control of the characteristics of the deposited layers, such as the number of layers deposited and their lateral sizes, by tuning the deposition parameters in a CVD experiment.

Until now, the most produced and studied 2D TMD semiconductor is MoS_2, for which the CVD deposition parameters are tuned for the production of high-quality 2D crystalline layers of lateral dimensions higher than $50\mu m$ [16]. Compared to monolayer MoS_2, which has a direct bandgap of 1.9 eV, monolayer $MoSe_2$ has a direct bandgap of 1.5 eV, closer to the optimal bandgap value needed for solar spectrum related applications, such as single-junction solar cells and photoelectrochemical cells. Also, it has a larger spin-splitting energy of $\sim 180meV$ at the top of the valence band, making it a more interesting material than MoS_2 for *spintronics* [2]. Moreover, few-layer $MoSe_2$ has nearly degenerate indirect and direct bandgaps, and an increase in temperature can effectively drive the system towards the 2D limit [25]. However, the CVD synthesis of large-scale monolayer $MoSe_2$ is more challenging than the synthesis of MoS_2 due to the lower chemical reactivity of selenium when compared to sulphur. This implies that longer reaction times are usually needed for large-scale deposition of $MoSe_2$, which inevitably leads to thicker films [20, 26]. Currently, the optimisation of the CVD experimental parameters for the production of high-quality monolayers of $MoSe_2$ with large lateral dimensions has yet to be achieved. In order for this to become possible, the influence of each deposition parameter on the characteristics and properties of the deposited layers has to be carefully studied and understood.

In this work, mono- to few-layer $MoSe_2$ nanofilms were synthesized onto SiO_x/Si substrates by CVD, using MoO_3 and Se powders as solid precursors. The experiments were carried out at atmospheric pressure, using Ar as the carrier gas and H_2 as the reducing agent. Different deposition parameters were studied, such as the mass of the precursors and the total gas flow rate, in order to understand the influence of each one on the properties of the $MoSe_2$ nanofilms produced. The samples were characterized by optical microscopy (OM), scanning electron microscopy (SEM), X-ray diffraction (XRD), Raman spectroscopy, atomic force microscopy (AFM) and photoluminescence (PL). Furthermore, silicon substrates were oxidised with different thickness of SiO_x and the PL for each SiO_x thickness was studied, using four different excitation energies.

This thesis comprises 5 chapters. Chapter 1 is the present introduction. Chapter 2 reviews the properties of monolayer $MoSe_2$ and the mechanisms behind the CVD of such layers. The description of the experimental setup used for the CVD synthesis of low dimensional $MoSe_2$ and for the oxidation of the silicon substrates is presented in chapter 3. The Results obtained using the CVD process are presented and discussed in chapter 4, as well as the results from the oxidation of the silicon substrates. Finally, chapter 5 presents the final conclusions and future work.

Chapter 2

Properties and synthesis of $MoSe_2$

2.1 Molybdenum diselenide

Molybdenum diselenide, $MoSe_2$, is a layered semiconductor TMD. Each layer has a thickness of $\sim 0.7nm$, and consists of a hexagonally packed layer of Mo atoms sandwiched between two layers of Se atoms, bonded by strong covalent forces (Figure 2.1). The bonds between atoms in the same layer are due to the hybridization of the p_z orbitals of Se atoms with the d orbitals of the Mo atoms, with Mo-Mo bonds of length 3.29Å. In the bulk and few-layer crystals, different layers are vertically stacked, coupled by weak van der Waals forces, thus allowing the crystal to be easily cleaved along the layer surface. Consequently, a single-layer of $MoSe_2$ can be simply obtained by exfoliation of the bulk crystal, in the same way as graphene, enabling the access to the exciting intrinsic properties of two-dimensional $MoSe_2$.

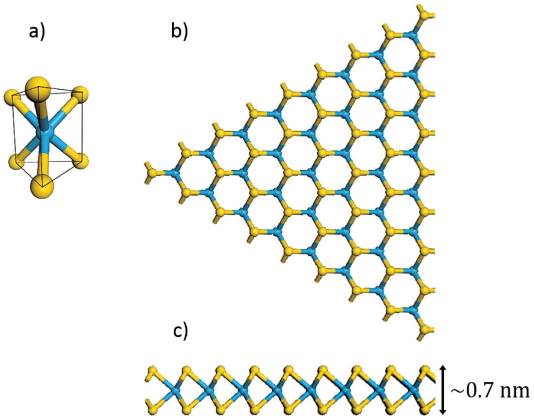

Figure 2.1: **Schematic of the crystalline structure of 2H-$MoSe_2$.** a) Trigonal prismatic polyhedron present in 2H-$MoSe_2$. b), c) Top and side view of the crystal lattice of 2H-$MoSe_2$, respectively. Blue atoms represent molybdenum and yellow atoms represent selenium. Adapted from Das *et al* [27].

The electronic band structures of $MoSe_2$ for bulk, 8-layer, 4-layer, bilayer and monolayer crystals, obtained by density functional theory (DFT) calculations [28], are shown in Figure 2.2. The indirect band gap of the bulk crystal (1.1 eV) undergoes a blue shift as the number of layers decreases from 8- to bilayer and turns to direct in the monolayer (1.5eV). This transformation is due to quantum confinement, that results in a change in hybridization between the anti-bonding p_z orbitals on Se atoms and d orbitals on Mo atoms, that are responsible for the states near the Γ-point. These states are highly sensitive to interlayer coupling, and so, suffer a transformation in energy when the number of layers decreases, causing the decrease of the valence band maximum (VBM) at the Γ-point of the Brillouin zone and the

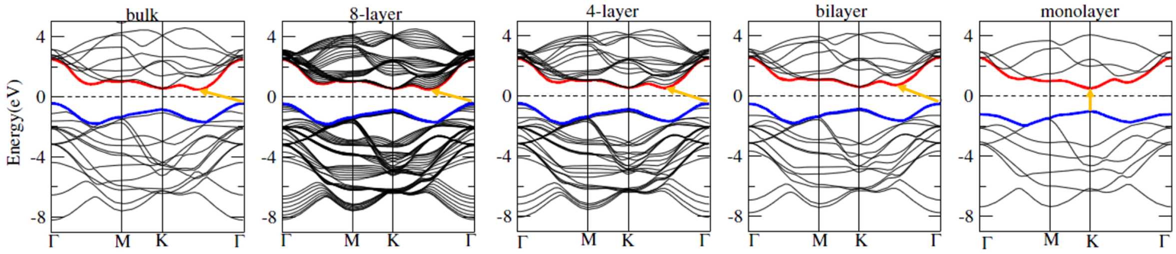

Figure 2.2: **Electronic band structure of bulk, few-layer and monolayer $MoSe_2$.** The top of the valance band (blue) and bottom of the conduction band (red) are highlighted and the Fermi level is set at 0 eV. The yellow arrow indicates the smallest value of the indirect or direct band gap. Adapted from Kumar *et al* [28].

increase of the conduction band minimum (CBM) at the middle point between the K and Γ points. On the other hand, the conduction-band states at the K-point remain independent of the number of layers because they are mainly due to localized d orbitals on the Mo atoms, that are located in the middle of the Se-Mo-Se layer, being relatively unaffected by interlayer coupling. All of the semiconductor TMDs undergo a similar indirect-to-direct band gap transformation [3,29]. This transformation is manifested as enhanced PL in semiconductor TMD monolayers, whereas in multilayer crystals only weak PL emission is observed [25].

Another exotic phenomenon that occurs in monolayer TMD, and in particular in monolayer $MoSe_2$, is the coupling of spin and valley degrees of freedom. The breaking of inversion symmetry in the monolayer (taking the M atom as the inversion center, an X atom will be mapped onto an empty location) together with a strong spin-orbit coupling (originated from the d-orbitals of the heavy metal atoms) creates two inequivalent valleys in the momentum space at the points K and $-K$, as represented in Figure 2.3. Due to the spin-orbit coupling, the degeneracy of the VBM is lifted, originating two VBM of different energies, with opposite spins. The time-reversal symmetry requires that the spin splitting at different valleys must be opposite, with K and $-K$ showing opposite situations. The valley degree of freedom can be accessed by using circularly polarized light, as is reported in the literature [30, 31]. The incidence of circularly polarized light with a certain polarization (right or left) on the monolayer, excites electrons with a particular spin (the selected spin depends on the frequency of the incident light) that only populate one of the two valleys. When these electrons relax to the ground state, they emit circularly polarized light with the same polarization, which indicates that valley polarization was achieved and preserved during the process [29,31]. The exploration of this phenomenon makes monolayers of TMD very promising for the development of a new kind of electronics, the *valleytronics*. Moreover, the strong spin-orbit coupling originates a large spin-splitting of the top of the valence bands, which in monolayer $MoSe_2$ has an energy of $\sim 180meV$, making these materials promising candidates for spintronic devices.

The electronic structure of monolayer semiconductor TMD can be tuned under applied mechan-

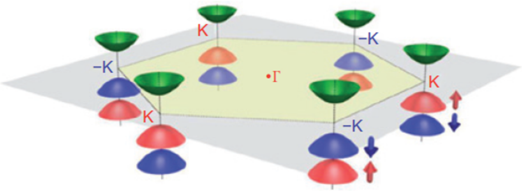

Figure 2.3: **Scheme of the first Brillouin zone of monolayer TMD.** Six valleys are shown, where K and $-K$ represent inequivalent valleys with opposite spin-orbit splitting of the valence band. The green surfaces represent the CBM and the red and blue surfaces represent the non-degenerate VBM, each of which is associated with a particular electron spin. Adapted from Chhowalla *et al* [29].

ical strain, which makes these materials very promising for applications in flexible electronic and optoelectronic devices. It has been reported, using DFT calculations [32, 33] and experimentally [34], that mechanical strains cause a direct-to-indirect bandgap transition in monolayer MX_2, reducing the bandgap so that at a critical value dependent on the type of applied strain (uniaxial, uniform, biaxial) a transition to metal occurs. For monolayer $MoSe_2$, the critical tensile strength has been estimated to be $\sim 6GPa$. Moreover, the dielectric properties have also been proven to be influenced by the type of applied strain [33].

Additionally, it was found that few-layer $MoSe_2$ crystals possess a nearly degenerate indirect and direct bandgap, implying that an increase in temperature can transform the indirect band gap of the few-layer system into direct, by thermally decoupling neighbouring layers via interlayer thermal expansion [25]. This is observed by an enhancement in the PL of the few-layer crystal with the increase in temperature, which is very similar to the PL enhancement observed when the indirect-to-direct band gap transition occurs with the decrease in the number of layers from the bulk to the monolayer crystal. This property is not observed in MoS_2, where the indirect and direct band gaps are well separated.

Recently, monolayer $MoSe_2$ has been reported to be used as an active channel in FET and photodetectors. A FET based on monolayer $MoSe_2$ shows n-type channel behaviour with a room temperature mobility of $\sim 50cm^2/Vs$ and on-off ratios larger than 10^6, for both mechanically exfoliated [4] and CVD-grown [21] single-layers. The carrier mobility of monolayer $MoSe_2$ is temperature dependent, increasing significantly when the temperature is reduced to $78K$, suggesting that phonons are a dominant scattering mechanism [4]. It has also been reported that electric double-layer transistors of monolayer $MoSe_2$, on sapphire substrates, behave like an ambipolar semiconductor, with preferred n-type and carrier mobilities of $\sim 23cm^2/Vs$ for electron transport and of $\sim 15cm^2/Vs$ for hole transport [6]. CVD-grown $MoSe_2$ monolayer has a fast response time $< 25ms$, which makes it suitable for fast photodetection applications [6]. The higher carrier mobility and faster response time of monolayer $MoSe_2$, compared to monolayer MoS_2, is attributed to the presence of less defects in the crystalline structure of 2D $MoSe_2$.

2.2 Chemical vapor deposition

2.2.1 CVD synthesis of $MoSe_2$

The CVD synthesis of monolayer $MoSe_2$ was first reported by Shaw *et al.* in 2014 [19], using a CVD reactor composed of a quartz tube placed in a tube furnace. The solid precursors used were MoO_3 (0.25g) and Se (0.50g) powders, that were placed in two different boats, at temperatures of 750 °C and 300 °C, respectively. The monolayers were deposited onto 300nm SiO_2/Si substrates, placed over the MoO_3 boat with the SiO_2 face down. The deposition occurred at atmospheric pressure, with a flow of 65sccm (standard cubic centimetres per minute) of Ar and 5sccm of H_2, where Ar was used as the carrier gas and H_2 as the reducing agent. The furnace was heated up to the growth temperature of 750 °C at a heating rate of 25 °C$/min$, and was kept at that temperature for 10 to 15min, after which it was cooled down to room temperature. The authors observed, by optical microscopy, the formation of triangular shaped $MoSe_2$ monolayers randomly distributed along the substrate surface, without any preferred orientation, and with lateral sizes $> 10\mu m$. The triangular shape was in agreement with previous reports on the deposition of other TMDs by CVD [16, 35]. The number of monolayers deposited was high, although it was observed the presence of bi- and few-layer flakes. The authors claim that without H_2 in the gas flow, no formation of $MoSe_2$ nanosheets was observed, and that the introduction of a small fraction of H_2 was sufficient for $MoSe_2$ crystals to nucleate and grow into extended 2D structures.

Using a similar CVD setup, Chang *et al.* [6] reported the deposition of single-layer $MoSe_2$ onto sapphire substrates, placed at the downstream side of the MoO_3 boat. The morphology of the monolayers was studied as a function of the distance of the substrate to the MoO_3 source. The images obtained by optical microscopy showed randomly distributed triangles with lateral sizes $\sim 5\mu m$ in the substrate region further from the MoO_3 powder, whereas in the region nearer the MoO_3 source a continuous film was observed, formed by small triangular domains. This indicated that the nucleation density increased with the proximity of the substrate to the MoO_3 powder.

The gas flow rate is one of the most important deposition parameters in CVD, because it can change the rate limiting mechanism from mass transport to surface reaction [36]. This changes the morphology of the thin film produced, due to an alteration of the nucleation rate. In the case of the deposition of low dimensional $MoSe_2$, the gas flow rate has to be tuned to enable the deposition of monolayer crystals, instead of few-layer clusters. Jung *et al.* [7] observed that a high flow rate (140sccm) was responsible for a high nucleation rate, causing the formation of hexagon shaped multilayers. On the contrary, lower flow rates (60sccm), decreased the nucleation rate, promoting the growth of mono- and bilayer $MoSe_2$ triangles.

As previously mentioned, the presence of H_2 in the flow rate was found to be crucial for the deposition of $MoSe_2$. In this sense, Lu *et al.* [20] described the synthesis of mono- to few-layer $MoSe_2$ by using only H_2 as the carrier gas. The 100nm SiO_2/Si substrate was placed 4-6cm from the MoO_3 powder, which was at the centre of the furnace, at a temperature of 800 °C. The deposition temperature was kept for 8 min, and a low pressure of $2.7kPa$ was used. The authors observed the growth of a monolayer continuous film, formed by small triangular domains, that extended along the substrate area of $1 \times 1cm^2$. The region of the substrate that was at a higher temperature (nearer the MoO_3 powder) contained more monolayers, whereas the region at a lower temperature (further from the MoO_3 powder) contained a relatively high density of few-layers. Regardless of the previous reports, Xia *et al.* [2] described the growth of monolayer $MoSe_2$ without the use of H_2 in the gas flow, using only Ar as the carrier gas. The authors observed the formation of triangular monolayers with edge lengths up to $40\mu m$. However, a much higher Se mass (0.50g) than MoO_3 mass(0.01g) was used, contrary to the previous reports, which may improve the efficiency of the reduction of MoO_3 vapours by Se, due to an excess of Se in the gas phase.

More recent reports [37, 38] use CVD systems very similar to the ones described, reporting high quality single-layer $MoSe_2$ with lateral sizes in the range $5-40\mu m$. However, the growth mechanisms for the deposition of monolayer $MoSe_2$ remain not fully understood. Studies of the change in morphology and thickness of low dimension $MoSe_2$ with the substrate temperature, MoO_3 powder temperature, H_2 fraction in the total gas flow rate, deposition time or $Mo : Se$ ratio at the substrate surface were not found in the literature. These are needed to achieve a full description and understanding of the growth mechanism of 2D $MoSe_2$, enabling the establishment of a reliable and scalable method for the deposition of $MoSe_2$ monolayers.

2.2.2 CVD growth mechanisms

Although the growth mechanism of low dimensional $MoSe_2$ has yet to be understood, there are some ideas from the study of conventional CVD of thin films [36, 39] and CVD of other low dimensional TMD [17, 18, 24, 40] that can be applied in an attempt to understand the influence of each deposition parameter on the characteristics of the $MoSe_2$ nanolayers produced. Consider the deposition of low dimensional $MoSe_2$ onto a SiO_2/Si substrate, placed over a quartz boat with the SiO_2 face down, at atmospheric pressure, using the same solid precursors and carrier gases as the ones previously described.

The gas flow in a CVD process can be characterized by the Knudsen number, K_n, which is a dimensionless parameter that assigns each type of gas flow to a particular pressure range [39]. It is given by

$$K_n = \frac{\bar{l}}{d}, \tag{2.1}$$

where $\bar{l}$ is the molecular mean free path and d is the quartz tube diameter. Since the deposition of low dimensional $MoSe_2$ is generally performed at atmospheric pressure and high temperatures (650-800 °C), the molecules frequently collide with each other, so that the mean free path of the gas molecules is significantly shorter than the dimensions of the quartz tube. In this case, $K_n < 0.01$, and the flow can be considered viscous. A viscous flow can be either laminar or turbulent. In laminar flow, the gas particles remain in the same displaced layers that are constantly parallel to each other. On the other hand, if the flow velocity is too high, these layers broken up and the fluid particles run into each other in a completely disordered way, originating turbulent flow. The Reynolds number, Re_L, is a dimensionless parameter that characterizes the flow of a viscous fluid [39], and is given by

$$Re_L = \frac{\bar{u}\rho L}{\mu}, \tag{2.2}$$

where $\bar{u}$ is the average velocity of the carrier gas, ρ is the mass density of the vapour (which can be calculated using the ideal-gas law, assuming that the vapour is diluted), L is the characteristic length (it can be taken to be the length of the substrate along the flow direction) and μ is the viscosity of the vapour. The average velocity of the gas flow is related to the gas flow rate by [41]

$$\bar{u} = \frac{\phi}{A_t}\frac{T}{T_0}\frac{P_0}{P}, \tag{2.3}$$

where ϕ is the total gas flow rate in sccm, A_t is the cross-sectional area of the quartz tube, T is the temperature in Kelvin and T_0 is the standard temperature ($273.15K$), P is the pressure and P_0 is the standard pressure ($1atm$). In the deposition of $MoSe_2$, low flow rates are usually used (≤ 80sccm), and the gas flow can be considered laminar ($Re_L < 2100$). Due to the nature of the laminar flow, a velocity gradient is formed and the velocity of the gas is zero at the substrate surface. The region in which the flow velocity changes from zero, at the substrate surface, to its bulk value is defined as the boundary layer [39]. Thus, the reactant gases flowing above the boundary layer have to diffuse through this layer to react at the substrate surface. This boundary has a thickness $\delta(x)$, given by [39]

$$\delta(x) = \frac{5x}{\sqrt{Re_x}}, \tag{2.4}$$

where Re_x is the Reynolds number at a position x on the substrate surface. It shows that the boundary layer thickness increases with lowered gas flow velocity (low Re_x) and with the distance along the substrate surface (increasing x). The average boundary-layer thickness over the whole substrate is

$$\bar{\delta} = \frac{1}{L}\int_0^L \delta(x)dx = \frac{10}{3}\frac{L}{\sqrt{Re_L}}. \tag{2.5}$$

The boundary layer determines the mass transport rate of the reactant species to the substrate surface. Since Re_L depends on the velocity of the gas molecules, the gas flow rate controls the boundary layer thickness and can change the growth regime from kinetic to thermodynamic. When the gas flow rate is too high, the boundary layer is thin and the diffusion of the reactant molecules to the substrate surface is fast. As the income of reactant species to the interface between the gas and the substrate surface is faster than the surface reaction, the latter becomes the growth limiting factor, and the products grow under kinetic conditions. In this case, the time of residency of the reactants molecules at the substrate surface may not be enough to allow the molecules to move into the right lattice locations, where the crystal domains could have had a lower surface free energy, promoting the growth of irregular crystal shapes [17]. Decreasing the gas flow rate increases the boundary layer thickness, resulting in a decrease of the mass transport rate which becomes closer to the rate of the surface reaction. If the mass transport rate is slightly higher than the surface reaction rate, the reactant molecules have sufficient time to diffuse along the substrate surface to occupy their rightful places in the crystal lattice. The crystal growth turns to the thermodynamic limit. However, when the gas flow rate is too low, the mass transport rate becomes the rate limiting factor, due to a thick boundary layer. The diffusion of the reactants towards the substrate surface is much slower than the surface reaction rate, and so the nucleation density increases, and three-dimensional and policrystalline growth are promoted. [36, 39].

Having into account the concept of boundary layer, the growth of low dimensional $MoSe_2$ can be divided into the following steps (see illustration in Figure 2.4):

1. The precursors evaporate and are transported in the downstream direction by the carrier gas, Ar. The MoO_3 powder is reduced to a Mo suboxide (MoO_{3-x}, $1 < x < 3$) by H_2 and, less frequently by Se, with the possible chemical equations:

$$MoO_3 + xH_2 \rightarrow MoO_{3-x} + xH_2O, \tag{2.6}$$

$$MoO_3 + \frac{x}{2}Se \rightarrow MoO_{3-x} + \frac{x}{2}SeO_2; \tag{2.7}$$

2. The reactant molecules diffuse through the boundary layer from the bulk vapour towards the substrate surface;

3. They are adsorbed onto the substrate surface;

4. The adsorbed molecules diffuse along the surface, and react to form $MoSe_2$ flakes:

$$MoO_{3-x} + \frac{7-x}{2}Se \rightarrow MoSe_2 + \frac{3-x}{2}SeO_2; \tag{2.8}$$

5. The gaseous by-products of the reaction are desorbed and diffuse away from the surface, through the boundary layer.

The first step defines the concentration profile of the precursors in the vapour phase along the CVD reactor and along the substrate surface. It also determines the reduction of the MoO_3 vapours, that has to be such that it promotes the reaction between the reduced MoO_3 vapours and Se. Step 2 determines the mass transport rate of the reactant species to the substrate surface and depending on the gas flow rate used, this step can be a growth limiting step because it influences the quantity of reactant molecules that arrive to the substrate surface. Then, step 3 determines the rate of adsorption of the molecules at the substrate surface, which than diffuse along the surface and react with each other to form $MoSe_2$ in step 4. If the mass transport rate in step 2 is too fast, the chemical reaction rate in step 4 becomes the rate limiting factor. Finally, in step 5, the by-products of the reaction are desorbed and diffuse away from the substrate surface, through the boundary layer.

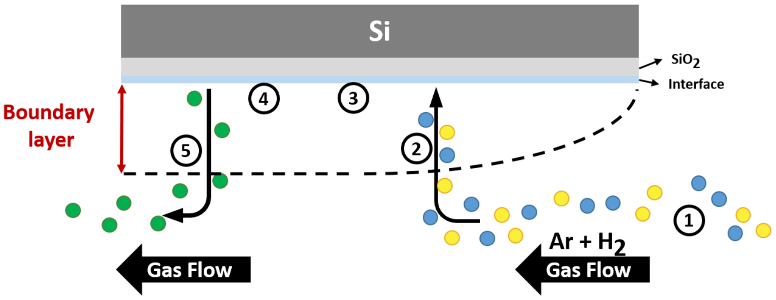

Figure 2.4: **Schematic illustration of the $MoSe_2$ growth process steps.** The yellow and blue circles represent Se and MoO_3 molecules, respectively, and the green circles represent the reaction by-products.

In CVD of thin films, the film thickness decreases along the surface of an horizontal substrate, due to the increase of the boundary layer thickness along the substrate surface [36]. As the boundary layer thickness increases, the mass transport rate decreases so that the amount of reactant species that arrive at the substrate surface decreases along the flow direction, depositing less product along the substrate length. In the case of the deposition of low dimensional TMDs, since the deposition times are small (10 to 20 min), a difference in film thickness is not observed, instead a transition from a continuous film to isolated islands [6] or a shape change of the isolated islands together with a decrease in their lateral sizes [17] are observed.

The transition from a continuous film to isolated islands can be explained in a similar way as the difference in thickness of a thin film. At the upstream edge of the substrate surface, which is the one closer to the MoO_3 powder, the boundary layer begins to form and is very thin (see Figure 2.4). Therefore, a lot of reactant molecules arrive at that region of the substrate surface, increasing the nucleation density, so that many small triangle domains merge to form a continuous film. Moving along the gas flow direction, not only the boundary layer gets thicker but also a lot of the reactant molecules have already been deposited. Thus, the number of reactant molecules available for reaction at the substrate surface decreases and randomly distributed triangle islands are grown.

In the case of the change in morphology of monolayer TMD crystals along the gas flow direction, a qualitative model was developed for MoS_2 by Wang *et al.* [17]. This model states that the change in morphology is mainly due to a change in the $Mo : S$ atom ratio along the SiO_2/Si substrate, which is a consequence of the precursors concentration gradients that form along the CVD reactor. Considering that S evaporates first and that a long distance separates the MoO_3 and S boats (which is usually the case), it is assumed that a homogeneous S atmosphere exists at the substrate region, so that the S concentration gradient in the vapour phase along the substrate surface can be negligible during the growth process. On the other hand, because the distance between the MoO_3 powder and the substrate is usually small, a sharp concentration gradient of MoO_3 in the vapour phase develops along the substrate surface. Consequently, the ratio $Mo : S$ decreases along the substrate surface, being responsible for the transformation in the shape of the MoS_2 monolayers.

According to the principles of crystal growth, the shape of a crystal is determined by the growth rate of the different crystal faces, which grow in order that the surface free energy is minimised. For monolayer MoS_2, the surface free energy corresponds to the edge free energy, and so its final shape will be related to the growth rate of the different edge terminations. The edges with lower energy will be the ones that have a lower growth rate because they are more energetically stable and so, will be the ones present at the edges of the crystal. This is because the less energetically stable edges grow faster in an attempt to minimize their edge free energy, and so they end up disappearing. The edge structures more commonly observed in monolayer MoS_2 are Mo zigzag ($Mo-zz$) terminations and S zigzag ($S-zz$) terminations. Although, in principle, they are the most energetically stable edges, S atoms in $S-zz$ edges only have two bonds with two Mo atoms, instead of three bonds with three Mo atoms (like the saturated S atoms in the middle of the layer), while the Mo atoms in $Mo-zz$ edges, have only four bonds with four S atoms, contrary to the saturated Mo that has six bonds with six different S atoms. This structural difference gives them different levels of chemical activity under different $Mo:S$ ratio conditions. The exact ratio between Mo and S atoms on the substrate surface will influence the energetic stability of the $Mo-zz$ and $S-zz$ terminations, causing a growth rate difference between the two types of terminations, which will impact on the domain shape. Hence, the crystal shape will be different for three different conditions: $> 1:2$, $1:2$ and $< 1:2$.

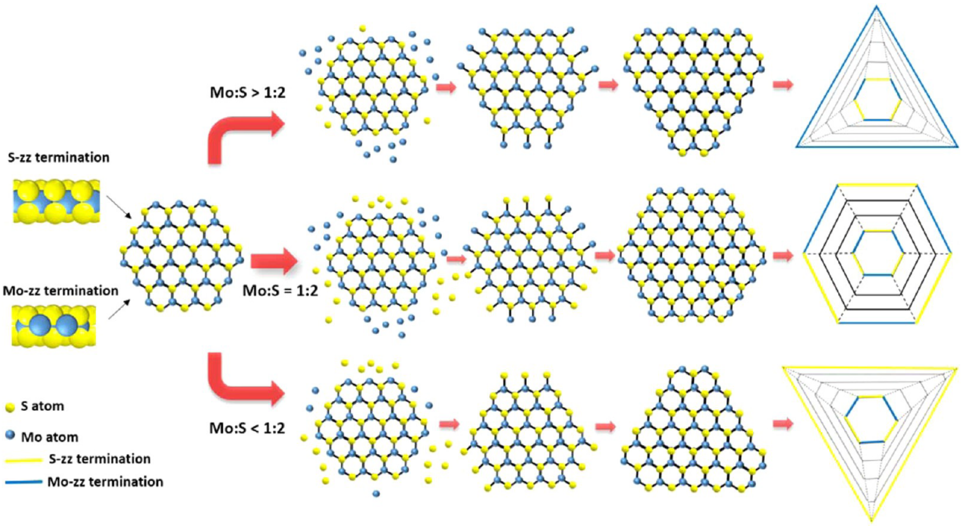

Figure 2.5: **Schematic illustration of the dependence of domain shape on the $Mo:S$ atom ratio.** The ball models on the left show two kinds of MoS_2 termination structures, S-zz and Mo-zz terminations. The ball-and-stick models in the central part show the top view microstructure of the monolayer MoS_2 crystal in different shapes. The schematic diagram on the right illustrates the domain shape changing procedure depending on the growing rates of two different terminations. Reproduced from Wang *et al* [17].

Assuming that all shapes start growing from a hexagonal nucleus with three $Mo-zz$ terminated edges and another three $S-zz$ terminated edges, the final shape of the monolayer crystal can be described for each one of the previous conditions, as illustrated in Figure 2.5:

- $> 1:2$, there is sufficient Mo in the vapour phase, the $S-zz$ terminations with unsaturated S atoms have higher probability of meeting and bonding with free Mo atoms, being more energetically unstable than the $Mo-zz$ terminations. Consequently, the $S-zz$ edges grow faster than the $Mo-zz$ edges, and the domain shape will change from a hexagon to a triangle with three sides of Mo-zz terminations;
- $1:2$, here the $Mo:S$ ratio is the stoichiometric ratio of MoS_2. The stability of each of the $S-zz$ and $Mo-zz$ terminations and the probability of the two types of edges meeting corresponding free atoms is very similar, which results in comparable growing rates. Thus, the final shape of the crystal will be a hexagon;
- $< 1:2$, there is sufficient S in the vapour phase, and the situation is opposite to the first condition. Here, the crystal shape will also transform to triangular, with three edges of $S-zz$ terminations.

Therefore, assuming a sufficient concentration of S and because the MoO_3 powder is nearer the substrate, the $Mo:S$ ratio at the upstream region of the substrate surface is $> 1:2$, and triangles with

$Mo-zz$ edges will be observed. Moving along the gas flow direction, the quantity of MoO_3 molecules that arrive at the substrate surface decreases[1], decreasing the $Mo:S$ ratio, which gets closer to $1:2$. Here, the $Mo:S$ ratio is slightly above $1:2$, so that the difference in the growth rate between the two types of terminations is small, resulting in the formation of truncated triangles. Then, at some point, the $Mo:S$ ratio becomes $1:2$, and the shape of the monolayers turns to hexagonal. Finally, as the quantity of MoO_3 molecules continues to decrease, the $Mo:S$ ratio becomes $< 1:2$, and the monolayers are again triangles, this time with $S-zz$ edges and lower lateral sizes. The decrease in lateral sizes happens because the amount of reactant species that arrives at the downstream region of the substrate surface is much smaller than the amount that arrives at the upstream region.

Another influent factor is the substrate temperature, which has to be sufficiently high to provide enough thermal energy to promote the desired reaction at the substrate surface. However, if it is too high, the reactant molecules can be desorbed right after being adsorbed or the reaction products can be dissociated after they are formed, due to an excess in thermal energy; if it is too low, the nucleation rate increases, promoting the growth of three-dimensional structures. It has been reported that in the deposition of monolayer MoS_2, an increase in the substrate temperature from 750 to 850 °C decreases the nucleation density, producing higher crystalline monolayers, and improving the homogeneity of their thickness. This can be explained by an increase in the mean free path of the precursor molecules on the substrate surface, enabling them to diffuse along the surface to attach to already formed nuclei, expanding the crystal lateral size [18].

In the case of the deposition time, it has been shown for WSe_2 that, if all of the other deposition parameters are fixed, such as the substrate temperature and the mass of the precursors, an increase in the growth time will not change the shape nor the layer number of the flakes deposited, but it will increase their lateral sizes within a certain period of time [24]. This is because the morphology and thickness of the deposited flakes are mainly influenced by the concentration of precursors in the gas phase and by the growth kinetics, which are established by the gas flow rate and the growth temperature, but not by the duration of the deposition. Hence, if the sources of the precursors would have sufficient quantity, the increase in the deposition time would allow the deposition of large-area single crystalline monolayers. However, it was observed that after a period of $\sim 15min$, the lateral sizes of the monolayers cease to increase. This is a consequence of the use of solid precursors, that are non-sustainable sources. As the deposition process proceeds, the evaporation rate of the precursors decreases due to the decrease in surface area, slowing down the lateral growth of the monolayers, that eventually ceases after a certain time period.

The study of the CVD deposition of MoS_2 and WSe_2 allows a first contact with the influence of the different deposition parameters on the characteristics of the monolayers produced. Although a quantitative description is not possible, the extracted qualitative information is very useful to conceive a first set of deposition parameters for the CVD growth of monolayer $MoSe_2$. From the previous discussion, it is seen that the deposition parameters that have a stronger influence on the characteristics of the layers produced are the gas flow rate, the mass of the precursors and the substrate temperature. Moreover, it is expected that the partial pressure of H_2 in the total gas flow rate be an influential parameter on the deposition of $MoSe_2$, because it will affect the efficiency of the chemical reaction between the MoO_3 and Se vapours.

---

[1] It is a consequence of the increase in the boundary layer thickness but it also happens because many of the molecules have already been consumed in the chemical reaction.

Chapter 3

Experimental Methods

The present chapter presents a description of the CVD experimental setup and the experimental procedure used for the synthesis of low dimensional $MoSe_2$ films, as well as the characterization techniques used to obtain the number of layers present in each sample and determine the quality of the layers produced. The experimental setup and procedure for the oxidation of the (111) Si substrates is also described.

3.1 Chemical vapour Depostion of $MoSe_2$ nanolayers

3.1.1 Experimental setup

The experimental setup used in this work is similar to the CVD systems reported in the literature for the deposition of $MoSe_2$ nanosheets [2, 19, 21]. In these systems, the vapour chemical reaction between the MoO_3 and Se solid precursors takes place inside a quartz tube placed in a tube furnace, with a flow of Ar and H_2, at atmospheric pressure. The MoO_3 and Se precursors are placed at temperatures between 700-820 °C and 220-300 °C, respectively. Substrates of SiO_2/Si, with different SiO_2 thickness, are placed with the SiO_2 face upside down over the MoO_3 boat, or near the MoO_3 powder, at the downstream side.

In our setup, the CVD reactor consists of a 1-meter long quartz tube centered inside a tube furnace (Thermolyne™ Type F21100, temperature range 100-1200 °C), as shown in Figures 3.1 a) and b). The furnace has a Single Set Point Control which enables to bring the furnace up to a setpoint temperature, with a constant heating rate and hold the desired temperature, which is measured by a type K thermocouple placed at the centre of the heating element. The quartz tube has an external diameter of 4.0cm and is closed by two KF40 stainless steel flanges and two O-rings, one at each end. The entrance flange has two openings, one for the entry of the gas flow ($Ar + H_2$), and another one for the entry of a thermocouple. This last opening is covered during the deposition experiments in order to prevent gas leakage to the exterior. The exit flange has one opening for the exit of the gas flow, which then bubbles in oil before it goes into the air exhaustion. A schematic representation of the whole setup is presented in Figure 3.1 c).

All of the experiments were performed at atmospheric pressure, using Ar as the carrier gas and H_2 as a reducing agent. The presence of a reducing agent is necessary since the reduction of MoO_3 by Se is not efficient due to the low chemical reactivity of Se [26]. A low percentage of H_2 in the total gas flow (lower than 15%) has been reported to be sufficient for the formation of $MoSe_2$ nano-crystals [6,19,26], so the influence of H_2 partial pressure in the layers produced was investigated. In our setup, the flows of Ar

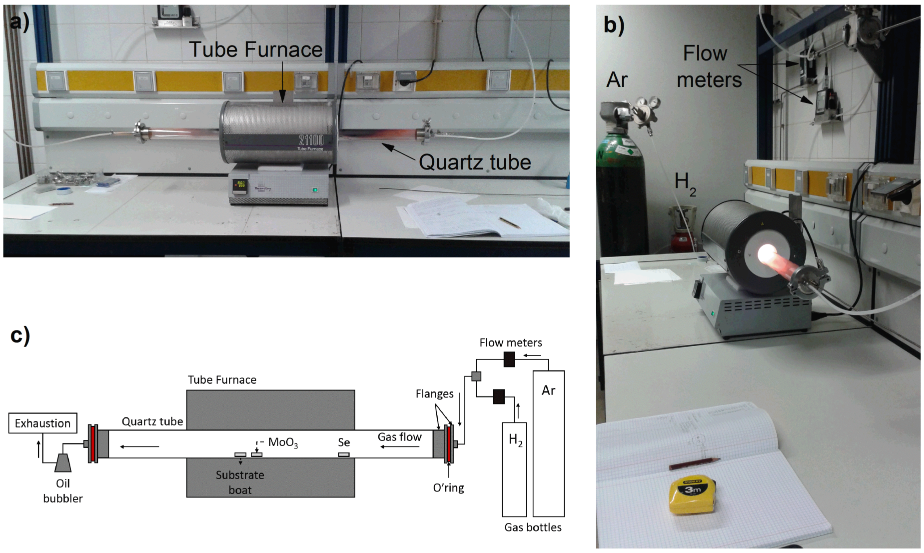

Figure 3.1: **CVD experimental setup.** a) Front view of the experimental setup, showing the tube furnace and quartz tube. b) Side view of the experimental setup, where the Ar and H_2 bottles and corresponding flow meters are seen. c) Schematic representation of the CVD setup.

and of H_2 were controlled by flow meters of maximum flow of 200sccm and 50sccm, respectively, which were monitored by a ”Multi-Gas Controller 647C” from MKS . The Ar and H_2 bottles and respective flow meters can be seen in Figure 3.1 b).

The precursors used were MoO_3 powder (Neyco, 99.99% purity) and Se powder (Alfa Aesar, 99.999% purity). The precursor holders were quartz boats, designed by us, in order for their curvature to be similar to the curvature of the interior of the quartz tube, which simplifies the positioning of the boats inside the tube. They were cut from a quartz tube of exterior diameter equal to 3.4cm and have a length of 2.0cm and a height of 1.0cm. Usually, the powders are placed at the centre of the boat, to guarantee that they are at a certain known temperature, owing to the sharp temperature gradient that exists in certain positions inside the CVD reactor (see temperature profile below). The distance between the precursors was kept constant in every experiment.

The substrates used were SiO_x/Si, produced by the dry oxidation of p-doped (111) Si wafers (see section 3.2). Typically, the Si pieces were cut with a diamond tipped pen, with the dimensions $1 \times 3.1cm^2$, in order for them to be placed over a quartz boat equal to the precursor holders with the SiO_x face down, see Figure 3.2 b). The substrate was placed at the centre of the boat, for the same reason as the precursors. The precursors and the substrate boats were positioned inside the tube with the help of a measuring tape. The typical positions used are the ones represented in Figure 3.2 a).

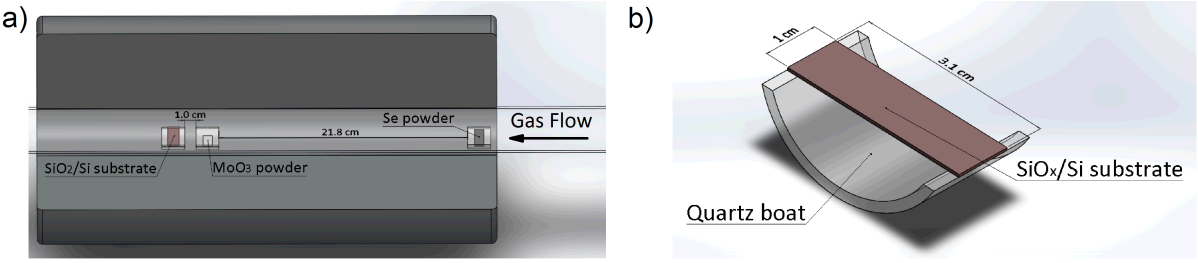

Figure 3.2: **Schematic representations** a)Schematic representation of the precursors and substrate positions inside the CVD reactor. b) Sketch of the SiO_x/Si substrate over a quartz boat.

Furnace temperature profile

To evaluate the temperature profile of the tube furnace, a 1-meter long type K thermocouple connected to a multimeter was used (measurement error ± 1 °C). The thermocouple stabilization time was high, so each measurement was made 5 to 10 min after the thermocouple was positioned at the desired position. The measured temperature along the tube length for a furnace temperature setpoint of 800 °C and for an Ar gas flow of 50 and 80 sccm, is plotted in Figure 3.3 a). The heating rate was 40 °C/ min. The origin of our position axis is at the end of the exit flange, as illustrated in Figure 3.3 b).

The utilization of a quartz tube with a length higher than the double of the furnace length had the purpose of preventing the overheating of the O-rings and of the plastic gas tubes that are attached to the flanges. This was confirmed by the temperature measurements, where the temperature near the flanges does not exceed 50 °C. The temperature profile is quite symmetric outside the furnace edges, indicating a gradual decrease in temperature as we are moving away from the furnace, as was expected. However, inside the furnace, the temperature profile is not uniform, not having an interval of positions with constant temperature. As we are moving away from the downstream furnace edge, the temperature increases rapidly till it reaches 800 °C. This temperature does not prevail for over 1 cm, and the centre of the furnace is at 827 °C. The temperature continues to increase till it reaches 840 °C at a position of 50cm. When approaching the upstream furnace edge, the temperature begins to decrease, having a sharp variation at the furnace edge.

From the plot in Figure 3.3 a), it can be seen that for both values of gas flow rate, the behaviour of the temperature profile is the same throughout the tube length. The difference in temperature between the two curves in the hot zone of the furnace is, in average, 8 °C, which can be negligible at the range of working temperatures because this difference is only 1% of the setpoint temperature. However, this difference in temperature between the curves measured with 50sccm and 80sccm was not observed for setpoint temperatures of 700 and 900 °C, where the difference in temperature between the two curves is, in average, 1 °C, which is equal to the measurement error. The temperature profiles for the different setpoint temperatures are plotted in Figure 3.4 a). The measurements with the two gas flow rates for

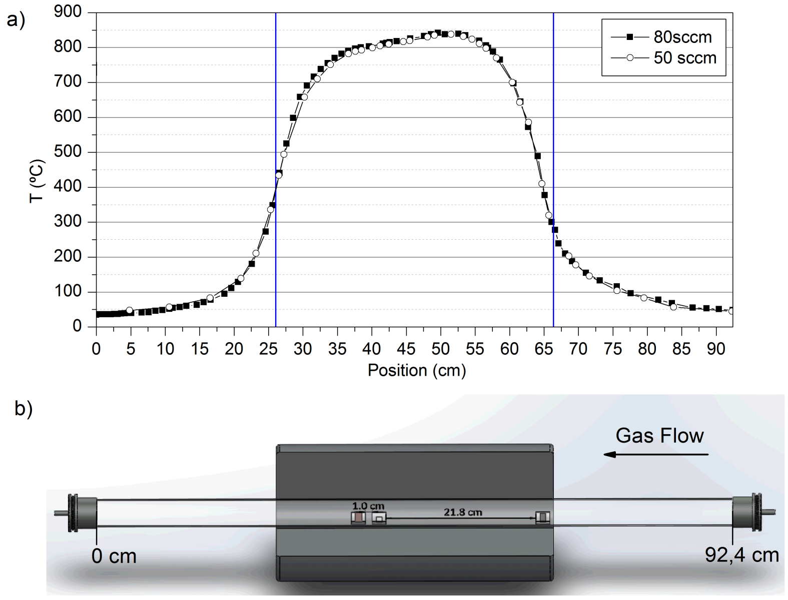

Figure 3.3: **Temperature Profile.** a) Temperature profile of the CVD reactor for a $T(setpoint) = 800$ °C for two different total gas flow rates. The blue lines represent the furnace edges. b) Scheme of the interior of the tube, with the substrate and precursors boats at the typically used positions. The edges of the furnace are aligned with the blue lines so that the scale presented in the graph is the one used for the positioning of the substrate and precursor boats.

setpoint temperatures of 700 and 900 °C were recorded on the same day, so that external conditions, such as room temperature and humidity were the same. In the case of the setpoint temperature of 800 °C, the measurements for the two values of gas flow rate were preformed on different days, which may explain the observed difference in temperature between the two curves. This shows that the gas flow rate does not alter the temperature profile of the furnace, for the three setpoint temperatures studied and in the gas flow rate range of 50 - 80sccm.

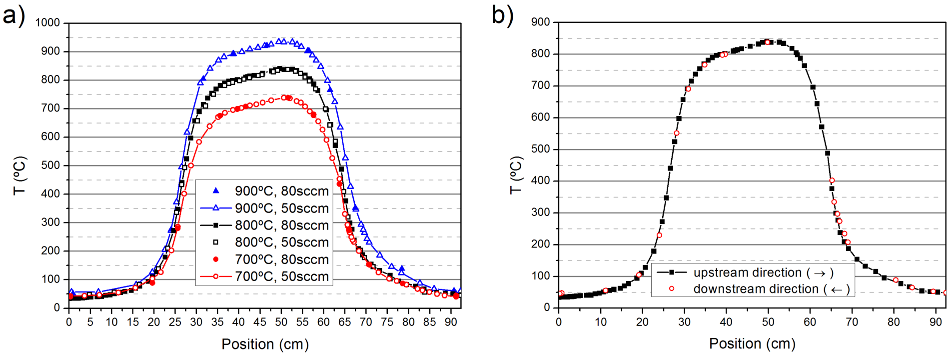

Figure 3.4: **Temperature profiles for different setpoint temperatures, gas flow rates and direction of measurements.** a)Temperature profiles for setpoint temperatures of 700 °C, 800 °C 900 °C, with gas flow rates of 50 and 80sccm. b) Temperature profiles for an Ar flow of 80sccm, measured in the upstream and downstream direction.

The temperature profile was measured in both directions, downstream and upstream, and both of them show the same temperature behaviour in the interior of the furnace, as shown in Figure 3.4 b), for an Ar flow of 80sccm. This means that the direction of measurement does not influence the temperature behaviour of the furnace and that the higher temperature zone at the upstream side of the furnace interior is not a consequence of the measurement direction. This effect might be due to a displacement of the heating element tube from the centre of the furnace. The profile measured in the upstream direction has 80 experimental points, and the downstream direction profile has 21 experimental points, which means that the former took over 6hours to be recorded, and the last one took only 1h45min. The fact that both profiles coincide (±2 °C) also indicates that the temperature profile is constant over long periods of time.

The study of the furnace temperature profile allows the choice of the precursors and substrate positions. In order for the MoO_3 powder be at 800 °C, the boat was placed between 40 - 42cm, where the temperature varies from 800 - 808 °C. The substrate boat was usually placed 1cm far away from the MoO_3 boat on the downstream side, between the positions 37-39cm. The positioning of the Se powder is more complex, since the temperature variation in the 400-200 °C zone, in the upstream side, is about 85 °C/cm. The Se boat was placed between 63.8-65.8cm which corresponds to 490-300 °C. Both powders and substrate were placed in the centre of the boats, in order to try to minimize the temperature variation. These positions are represented in Figure 3.3 b).

In order to understand if these positions gave the correct temperature in the case of a deposition experiment, the temperature behaviour over time was measured during an experiment. The thermocouple was placed outside the quartz tube, touching its surface at the desired positions. The setpoint temperature was 800 °C, and the heating rate was 40 °C/min so that the heating took 20min. The setpoint was fixed for 15min, and then the furnace was turned off and let cool naturally to room temperature. The obtained values are plotted in Figure 3.5 b). From this plot, it can be seen that the MoO_3 temperature increases linearly with the increase of the furnace temperature [1]. After the heating period, the MoO_3 temperature

---

[1] The furnace temperature is the temperature measured by the thermocouple incorporated in the furnace, which is read in the furnace setpoint controller.

is 814 °C, but it decreases to 808 °C within the first 2 min of deposition time, remaining constant at this value till the heating is turned off. In the case of the *Se* position, it reaches a temperature of 271 °C at the beginning of the deposition time, and it continues to increase till it reaches 308 °C after 15min.

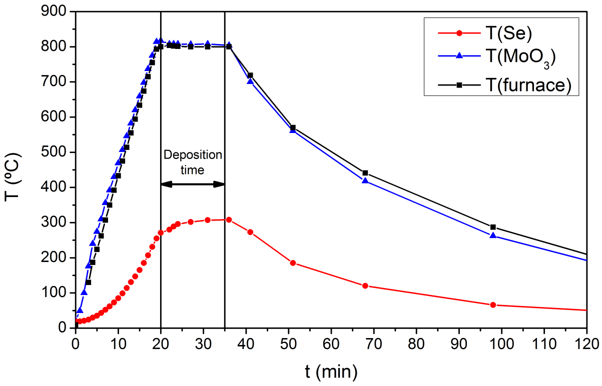

Figure 3.5: **Temperature variation over time.** Plot of temperature over time at the MoO_3 and *Se* precursors positions, measured outside the quartz tube. The vertical lines indicate the 15min of deposition time.

There are several possible explanations for the large difference in measured temperature values at the *Se* powder position between the temperature profile and the temperature variation over time. First of all, as it has been mentioned, the temperature variation over time measurements were made outside the quartz tube, so these values are subjected to convection phenomena that occur in the air near the tube surface, which is different from the air flow phenomena that occurs inside the tube, where a constant flow is passing. Moreover, as the air outside the quartz tube is not confined to a reservoir, heat dissipation through the surrounding air has to be taken into account, which might explain the lower temperature values. However, there exists time phenomena that we did not have into account while doing the temperature profile measurements that were performed over periods of time longer than 1hour, which is much longer than the 15min deposition time. The tube furnace is lined with ceramic material, whose purpose is to isolate the exterior of the furnace from the high temperature values. While the centre of the furnace is heating, the edges of the furnace heat due to heat propagation, so the heat takes some time to reach the edges. When the furnace setpoint temperature reaches 800 °C, the *Se* position reaches 271 °C and continues to rise over the passage of time. After 15min it reaches 308 °C, and we can extrapolate that after 1hour, its temperature may reach the value observed in the temperature profile studies.

This contradicts what was said before about the profile being constant over time, which indicates that the temperature profile takes some time to become constant. Although faster measurements were made, they were not fast enough to see this difference. Since each temperature profile reading took 5 to 10min to do, when the *Se* position was reached, over 15min had passed, implying that the temperature profile was already stabilized. This justifies the time dependent temperature profile, that only becomes constant over time after long periods of time.

This observed difference in the *Se* position temperature is not so drastic in the MoO_3 position because it is near the centre of the furnace, where the heat is well isolated from the exterior, and the convection phenomena due to the exterior air are not so important. Furthermore, the MoO_3 position is heated at the same rate as the centre of the furnace, since it is nearer the heating source, so the time phenomena described for the *Se* position does not occur in the same proportion. What happens in the MoO_3 position is that it heats to 814 °C setpoint, but after 2min it stabilizes at 808 °C, and it remains so.

In order to confirm these assumptions and determine exactly the temperature profile of the furnace right after the end of the heating process, it is necessary to do a precise study of the temperature variation over time at different positions. The determination of the temperature profile presented by the reactor at the beginning of the deposition phase is important to guarantee that the Se and MoO_3 powders are in the vapour phase throughout the whole deposition time. A plot of the temperature over the position in the reactor at the beginning, during and at the end of the deposition phase, would be necessary for the understanding of the temperature variations that the precursors (in the solid and gas phase) and the substrate are subjected to during the deposition.

Deposition parameters

In a CVD experiment, there are several parameters that influence the characteristics of the sample produced. For the deposition of $MoSe_2$ nanolayers these parameters are:

- Temperature of the MoO_3 and Se precursors.

  It influences the concentration of each precursor that will be present in the vapour phase. It is important that the Se concentration is uniform on the substrate surface, so the Se must evaporate before the MoO_3 powder. In this work, the MoO_3 temperature was 808 °C, and the Se temperature was 300 °C.

- Substrate temperature.

  The crystallisation of material on a substrate occurs spontaneously when the growth temperature (i. e. the substrate temperature, T) is lower than the thermodynamic equilibrium temperature (T_e) [42]. A degree of supercooling can be defined as $\Delta T = T_e - T$, and both the growth and nucleation rate will be influenced by this factor. For high ΔT, the nucleation rate is high, and so, many triangular domains will be formed. Moreover, as T is low, the molecules have low thermal energy to diffuse to already existing nucleation sites, preventing the lateral growth of the crystal domains. By increasing T (decreasing ΔT), the nucleation rate decreases, but an increase in growth rate occurs, as the molecules have sufficiently energy to diffuse through the substrate surface to join other nucleation sites. In this sense, for the growth of large-area $MoSe_2$ monolayers, the substrate temperature has to be high enough to promote the growth rate of the triangular domains, expanding their lateral sizes, and to enable a low nucleation density, to guarantee the deposition of single-crystal domains.

  Here, three different substrate positions were studied: over the MoO_3 boat where the temperature was 808 °C(sample 5), in the MoO_3 boat at the downstream side of the MoO_3 powder with a temperature of 800 °C(sample 6) and over a quartz boat 1cm away from the MoO_3boat at the downstream side at a temperature of 790 °C(samples 7 to 20).

- Distance between the precursors.

  A high distance between the two precursor sources will allow a more uniform concentration of Se in the vapour phase so that the Se concentration gradient can be neglected at the substrate surface [40]. The distance between the precursors boats was kept constant at 21.8cm.

- Distance between the substrate and the MoO_3 powder.

  It influences the concentration gradient of MoO_3 at the substrate surface. A lower distance between the substrate and the MoO_3 source increases the concentration of MoO_3 at its surface, which may promote the crystallization of Molybdenum oxide crystals, if the concentration of Se is not enough. In our experiments, this distance depended on the substrate position used (see substrate temperature).

- Quantity of MoO_3 and Se powders used.

  Selenium has an evaporation rate higher than the MoO_3 powder, which means that it is necessary to have a larger amount of Se mass to guarantee that there exists sufficient Se for the reaction to occur. The influence of the mass of the precursors on the properties of the films produced was studied in this work. The interval of MoO_3 mass used was 0.20 - 0.04g and of Se mass was 0.21 - 0.61g.

- Flush flow rate and flush time.

  To guarantee that there is no residual oxygen present in the reactor chamber and that the only gases present are the carrier gas, the reducing agent and the presursor vapours. In every experiment, the flush flow was 200sccm of Ar and the flush time was 1h30min.

- Heating rate and heating flow rate.

  To ensure that the reaction chamber has a uniform concentration of Se when the MoO_3 powder starts to evaporate, to prevent the deposition of molybdenum oxide at the substrate surface before the selenium arrives to react with the MoO_x molecules. In this work, the heating rate was 40 °C/ min and the heating flow rate was 5sccm of Ar.

- Deposition flow rate.

  It influences the time of residency of the reactants at the substrate surface and the thickness of the boundary layer, which affects the diffusion rate of the reactants through the boundary layer to the substrate surface. This parameter can change the deposition regime from thermodynamic (low flow rate) to kinetic (high flow rate). Here, the influence of the total flow rate was studied by comparing the properties presented by samples produced with 20sccm and 60 sccm of total flow rate (samples 20 and 18, respectively).

- Percentage of H_2 in the total deposition flow rate.

  It promotes the reaction of the MoO_x molecules with Se because it assists the reduction of the MoO_3 molecules. If it is too low, the reduction of the MoO_3 vapour is not successful and the reaction between MoO_3 and Se may not occur. If it is too high, it may reduce the MoO_3 to form Mo in the vapour phase, which is stable and a solid at the deposition temperature. In this work, the percentage of H_2 was studied in the interval 3.33 - 16.67 %.

- Cooling flow rate.

  A high cooling flow can increase the cooling rate in such a way that the film cracks due to the difference between the thermal coefficients of the film and the substrate. Moreover, if it is high, but not high enough, may promote the deposition of 3D crystals above the film, due to a decrease in the boundary layer.

3.1.2 Experimental procedure

The experimental procedure was adapted from the procedures reported in the literature [2,19–21,26]. A flowchart of the experimental procedure can be found in Figure 3.6. It is as follows:

- The quartz tube is cleaned with acetone and 2-propanol, with the help of a pipe cleaner, and blown dry with N_2. It is placed centered inside the furnace.
- The quartz boats and the substrate are cleaned by bath sonication in acetone for 15min, followed by bath sonication in 2-propanol for another 15min, and then blown dry with compressed N_2.
- The precursors mass are measured in a digital scale and transported inside aluminium paper.
- The Se powder is placed at the centre of the boat, and positioned inside the tube at 63.8 - 65.8cm.
- The MoO_3 powder is placed at the centre of the boat, and positioned inside the tube at 40 - 42 cm.
- The substrate is centered with the SiO_2 face down over a quartz boat, and is positioned inside the tube at 37 - 39cm.
- The tube is isolated from the exterior by the two flanges.
- The tube is flushed with 200sccm of Ar for 1h30min.
- The flow is lowered to 5sccm of Ar, and the furnace temperature is set to 800 °C, at a heating rate of 40 °C/min. The heating takes 20min.
- When the furnace reaches 800 °C, the flow is changed to 50sccm of Ar and 10sccm of H_2, and is kept for 15min.
- After 15min, the H_2 flow is closed and the Ar flow is decreased to 30sccm. The furnace is turned off.
- When the furnace temperature reaches 200 °C the flow is increased to 200sccm to fasten the cooling process and to guarantee that all toxic by-products leave the tube.
- When the reactor reaches the room temperature, the sample is removed from the tube.
- The tube and the boats are cleaned as described in the first two items.

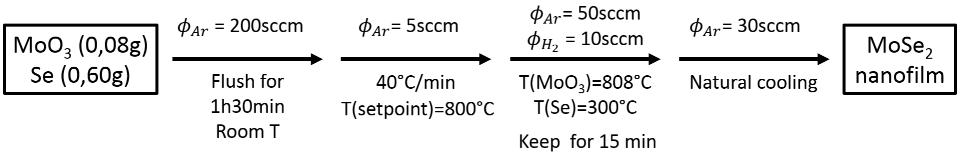

Figure 3.6: **Procedure Flowchart.** Flowchart describing the main steps of the experimental procedure.

3.2 Oxidation of (111) Si substrates

3.2.1 Visibility of TMD on SiO_2/Si substrates

A simple and non-destructive way of detecting two-dimensional layers is by using optical microscopy. It has been reported that monolayers of graphene and TMD deposited on SiO_2/Si substrates produce sufficient optical contrast with respect to the interference color of the underlying SiO_2 so that they can be easily detected [43, 44]. This optical contrast appears due to an increase in the optical path, which produces a phase shift of the interference colour, and due to the opacity of the monolayers. Using Fresnel theory on a stacking composed of a monolayer and a SiO_2 thin film on top of a semi-infinite

Si film, one obtains an expression for the intensity of reflected light as a function of the Fresnel coefficients. This intensity depends on the complex (or real) refractive indexes of each stack component (n_{2D}, n_{SiO_2} and n_{Si}) and on the phase shifts induced by changes in the optical path due to the two thin films, $\phi_i = 2\pi d_i n_i/\lambda$ where $i = 2D$, SiO_2. The contrast can then be defined as the relative intensity of reflected light in the presence ($I(n_{2D})$) and absence ($I(n_{2D} = 1)$) of the monolayer, which gives the expression

$$Contrast = \frac{I(n_{2D} = 1) - I(n_{2D})}{I(n_{2D} = 1)}. \tag{3.1}$$

The refractive indexes of the monolayer and of the Si are complex, where the real part is the real refractive index and the imaginary part is the extinction coefficient. It is the existence of a non-zero extinction coefficient in the monolayer TMD (a consequence of the presence of an energy gap in the visible range) and graphene that is responsible for the opacity since it indicates that some light was absorbed while passing through the monolayer. In the case of the SiO_2 layer, its refractive index is real, as a result of it being transparent to visible light. All of the refractive indexes vary with the wavelength of the incident light and the phase shifts depend on the thickness of the monolayer and on the SiO_2 thickness. Therefore, the optical contrast of the monolayer on top of SiO_2/Si will depend on the SiO_2 thickness, and there are thicknesses for which the contrast is maximised and others for which it is minimised. It also means that for the same SiO_2 thickness, a different number of layers of TMD will have different contrast, being possible to distinguish between mono- and few-layer.

For TMD, the optical contrast was studied for SiO_2 thickness lower than 300nm, under white light illumination, by Benameur *et al.* [44]. The authors reported that for SiO_2 thickness in the 50-100nm and 200-300nm range the TMD monolayers should present sufficient contrast to be detected. On the other hand, in the 0-50nm, 100-130nm and 160-200nm range, the contrast is low ($< 5-10\%$), and the monolayers are not visible. Based on their calculations and experimental results, they concluded that for a SiO_2 thickness of 90nm and 270nm, the TMD monolayers have sufficient contrast for them to be easily detected. This study was done for monolayers of MoS_2, WSe_2 and $NdSe_2$. Although a similar study for $MoSe_2$ has not been reported, the results for the previous TMDs are very similar amongst them and to the results obtained for graphene [43]. Thus, it can be assumed that a $MoSe_2$ monolayer will have sufficient optical contrast for the SiO_2 thickness reported.

Beyond the visibility of monolayer TMD by optical microscopy, the use of SiO_2/Si substrates has other advantages: it is useful for the fabrication of electronic and optoelectronic devices right onto the as-deposited layers due to the presence of the insulating SiO_2 layer; and the oxide layer can be easily decomposed by chemical means [45, 46] without degrading the deposited layer, enabling its easy suspension and transfer to other substrates (e.g. flexible substrates) as well as for the integration in low dimensional devices as a 2D building block [47]. Moreover, in the present work, it was observed that a thick oxide layer is needed to cloak the PL contribution from the SiO_x/Si interface in order to allow the correct identification and interpretation of the PL of $MoSe_2$ nanolayers, as will be discussed in Subsection 4.1.2.

Here, the oxidation of silicon substrates with $\sim 90nm$ of SiO_2 was performed (Subsection 4.1.1), to maximise the contrast between the $MoSe_2$ nanoflakes and the substrate, under white light illumination. The oxidation of Si with 230nm of SiO_2 was also performed to compare photoluminescence results (see Subsection 4.1.2).

3.2.2 Deal-Grove model

The Deal-Grove model [48] was used to estimate the oxidation time needed to obtain a SiO_2 layer of thickness x_{ox} over a Si substrate.

Consider the thermal oxidation of silicon. Assuming a SiO_2 layer of thickness x_{ox} that covers a silicon sample, it is known from experiment that the oxidation process occurs by the inward movement of oxidant species through the oxide layer to the $Si-SiO_2$ interface, where the reaction occurs and silicon is consumed. This process implies that the transported oxidant species must go through three stages: 1) it is transported from the bulk gas phase to the gas-SiO_2 interface; 2) It diffuses across the oxide layer towards the SiO_2-Si interface; 3) it forms a new layer of SiO_2 by reacting at the silicon surface. Each of this stages has associated a flux of oxidant species, which is the number of oxidant molecules crossing a unit surface area in a unit time. Considering that the three fluxes are in steady state, that is, that they are identical at all times, Deal and Grove [48] obtained the following expression for the oxide growth rate

$$\frac{dx_{ox}}{dt} = \frac{kC}{N(1+\frac{k}{h}+\frac{kx_{ox}}{D_{eff}})}, \tag{3.2}$$

where k is the chemical reaction rate constant, h is a gas-phase transport coefficient, C is the equilibrium concentration of the oxidant in the bulk gas phase and N is the number of oxidant molecules per unit volume that are needed to grow a unit volume of oxide.

They assumed that the silicon might have had an initial oxide layer of thickness x_i prior to the oxidation step under consideration, imposing that

$$x_{ox} = x_i \quad \text{at} \quad t = 0. \tag{3.3}$$

This assumption is important because x_i can be interpreted as the thickness of the oxide layer grown before the approximations of this model become valid. Moreover, x_i can also be regarded as the naturally grown oxide layer (native oxide, that grows in air at room temperature) and enables the consideration of multiple oxidations. Solving the above differential equation taking into account the initial condition gives

$$x_{ox}^2 + Ax_{ox} = Bt + x_i^2 + Ax_i \tag{3.4}$$

which can be written as

$$\frac{x_{ox}^2}{B} + \frac{A}{B}x_{ox} = (t+\tau), \tag{3.5}$$

where

$$B = \frac{2D_{eff}C}{N}, \tag{3.6}$$

$$B/A = \frac{C}{N\left(\frac{1}{k}+\frac{1}{h}\right)}, \tag{3.7}$$

and the parameter τ is the correction parameter for the presence of the native oxide layer of thickness x_i:

$$\tau = \frac{x_i^2 + Ax_i}{B}. \tag{3.8}$$

Solving equation 3.5 gives an expression of the oxide thickness as a function of time

$$\frac{x_{ox}}{A/2} = \left[1 + \frac{t+\tau}{A^2/4B}\right]^{1/2} - 1, \tag{3.9}$$

which can be studied for two limiting cases:

$$\text{For} \quad t \gg A^2/4B, \qquad x_{ox}^2 \cong Bt, \tag{3.10}$$

$$\text{For} \quad t \ll A^2/4B, \qquad x_{ox} \cong \frac{B}{A}(t+\tau). \tag{3.11}$$

Thus, for sufficient long oxidation times, the oxidation equation reduces to a power law of coefficient B, called the parabolic constant. This constant, as can be seen from expression 3.6, reflects the diffusive nature of the oxidation process, which is predominant at longer times. On the other hand, the oxidation equation has a linear behaviour at relatively small times, where the coefficient B/A is called the linear constant. From expression 3.7, this constant gives the contribution of the chemical reaction rate to the oxide growth rate. Actually, the growth rate is higher at the beginning of the oxidation process, where the growth is linear and the chemical reaction at the SiO_2/Si interface prevails. With the growth of the oxide layer as time passes, the oxidizing molecules have to diffuse across an increasing SiO_2 thickness, and the contribution of the diffusion of the oxidant species becomes predominant over the chemical reaction at the interface, decreasing the growth rate and turning it into a power law. Both B and B/A constants are time- and thickness-independent parameters, which corresponds to constant values of the diffusion coefficient, gas-phase transport coefficient and chemical reaction rate constant throughout the oxidation process [49]. However, they assume different values for different oxidation temperatures, since both the diffusion coefficient and the chemical reaction rate are temperature dependent.

The oxide growth rate is not the same for different oxidising agents, e.g., H_2O and O_2, which correspond to wet and dry oxidation, respectively. This is due to the fact that the diffusion coefficient is different for each molecule. Water molecules diffuse more easily across a SiO_2 layer than O_2 molecules, which implies that the oxidation time for wet oxidation is considerably lower than for dry oxidation [39]. However, this decrease in oxidation time results in a less homogeneous SiO_2 thickness along the Si surface, which is not desirable.

Different crystallographic orientations of the Si surface result in different oxide growth rates because they influence the kinetic mechanism for the thermal oxidation [48–50]. It has been reported that, at atmospheric pressure, the growth rates for three different crystallographic planes have the order $(111) > (110) > (100)$ at temperatures between 750 and 1000 °C, and for SiO_2 thicknesses higher than 25nm [50]. This implies that the linear and parabolic constants have different values for different Si surface orientations, which will influence the oxidation time. The higher the growth rate, the less oxidation time is needed to grow the same thickness of SiO_2. Several factors can be responsible for this dependency, like the density of Si atoms on different crystallographic planes and the stress in the oxide film which can be different for different crystallographic orientations.

In this work, the dry oxidation of $(111)Si$ wafers was performed, since the oxidation time is lower for this crystallographic orientation compared to the oxidation time necessary to grow an oxide layer of the same thickness in $(100)Si$. For oxidation times of 2h50min and 10h30min, thicknesses of $87 \pm 5nm$ and $230 \pm 11nm$ were obtained (see Section 4.1.1).

3.2.3 Experimental setup and procedure

The CVD experimental setup for the deposition of the $MoSe_2$ nanofilms was adapted for the dry oxidation of p-doped (111) Si wafer pieces. The $Ar+H_2$ flow was replaced by an O_2 flow, which was bubbled in Fomblin® oil before going into the air exhaustion (so that the excess of oxygen became dissolved in the oil). In order to prevent contamination from the products of the CVD reaction, a pristine quartz tube was used. The temperature setpoint of the furnace was 900 °C, and the temperature profile of the furnace at that temperature has the same behaviour as previosly mentioned (see Figure 3.4 a)). The temperature profile of the hotter zone inside the furnace can be seen in Figure 3.7. In this way, two to four Si pieces over quartz boats (polished face up) were put in the hotter zone at 934 °C, where an interval of 4cm has uniform temperature, to try to guarantee a uniform SiO_2 thickness along the Si width.

The experiment procedure is as follows:

- The quartz tube is cleaned with acetone and 2-propanol and blown with N_2. It is placed centered inside the furnace.
- The quartz boats and the Si pieces are cleaned by bath sonication in acetone for 15min, followed by in 2-propanol for another 15min, and then blown with N_2.
- The Si pieces over the quartz boats are placed inside the tube between 48.6 - 52.6cm.
- The tube is closed at both ends by two flanges.
- The tube is flushed with 100sccm of O_2 for 1hour.
- The flow is lowered to 5sccm of O_2, and the furnace temperature is set to 900 °C, at a heating rate of 40 °C/min. The heating takes 24min.
- When the furnace reaches 900 °C, the flow is changed to 100sccm of O_2 and is kept for 2h50min to 10h30, depending on the desired SiO_2 thickness.
- After the oxidation time has passed, the furnace is turned off and the flow is lowered to 50sccm of O_2.
- When the reactor reaches the room temperature, the substrates are removed from the tube.

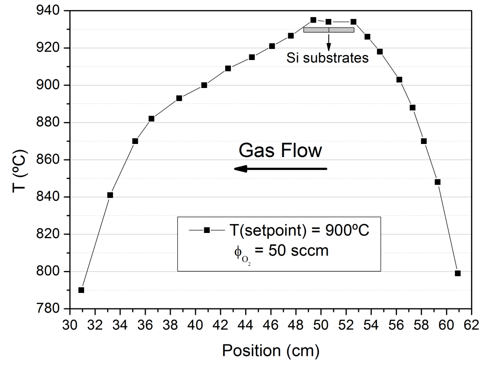

Figure 3.7: **Temperature profile for $T(setpoint) = 900$ °C.** Temperature profile of the hot zone of the furnace for a temperature setpoint of 900 °C, where the grey rectangles indicate the positions of the Si substrates. A flow of $\phi_{O_2} = 50sccm$ was used during the temperature measurements.

3.3 Characterization Techniques

3.3.1 Optical Microscopy (OM)

In optical microscopy (OM), the surface of the sample is illuminated with visible light and the image is formed by focusing the reflected light onto the eyepiece of the optical microscope. This reflected light is composed of light whose optical path was not changed by the sample and light that interacted with the sample suffering a phase change (due to a change in optical path). The interference between this two types of light forms what is called an optical image. This image can be captured by optical cameras equipped with CMOS (Complementary Metal-oxide Semiconductor) or CCD (Charge-coupled Device) sensors. The use of an optical microscope allows a simple, rapid and non-destructive characterization of the surface of large-area samples, with a resolution of a few micrometers.

As was noted in Section 3.2.1, optical microscopy has been widely used for the identification of monolayer $MoSe_2$ on SiO_2/Si substrates. In this work, the optical images of the samples were obtained by a DINO-EYE EYEPIECE camera (AM7023B) on a Nikon OPTIPHOT type 104 microscope, equipped with lenses of 5×, 20× and 40× magnifications.

3.3.2 Field Emission Gun - Scanning Electron Microscopy (FEG-SEM)

In scanning electron microscopy (SEM), a high energy electron beam is focused on a sample to produce a high-resolution image of its surface. When the accelerated electrons from the electron beam interact with the sample, they are decelerated and their kinetic energy is dissipated as secondary electrons (SE), backscattered electrons (BSE), characteristic X-rays, visible light (cathodoluminescence), and heat [51]. A SEM has usually two modes of operation, one that uses SE and another that uses BSE. The SE are low energy electrons that escape the atoms near the sample surface (few nanometers in depth) by inelastic scattering with the electrons from the electron beam. In this way, they are adequate to image the surface morphology and topography of the sample. The BSE are high energy electrons that are elastically scattered by the sample atoms. Since the rate of scattering electrons is different for atoms with different atomic weight, BSE allows the formation of an image where the contrast indicates areas with distinct chemical composition. The SEM images produced by this two modes of operation have a three-dimensional appearance, which results from the large depth of field presented by this microscope.

One of the consequences of the inelastic scattering of the incident electrons with the electrons from atoms in the sample, is the excitation of the sample electrons to high energy levels. Once they return to their lower energy states, X-rays with a characteristic energy are emitted. Their energy is related to the difference in energy levels of each element, thus the chemical composition of a selected area can be obtained by detecting the emitted X-rays. This is called energy-dispersive X-ray spectroscopy (EDS).

In the present work, SEM images of the samples were used to identify the presence of few-layer $MoSe_2$ triangles with small lateral size ($< 5\mu m$), that cannot be seen in optical microscope images. The thickness of the SiO_x layer in the SiO_x/Si substrates was measured from the SEM images of their cross-section. The SEM images were obtained by SE imaging on an FEG-SEM JEOL 7001F, coupled with EDS.

3.3.3 Atomic Force Microscopy (AFM)

An image of the topography of a sample surface with nanometer resolution can be obtained by Atomic Force Microscopy (AFM). The sample surface is swept by an ultrathin tip coupled to a cantilever, which is parallel to the plane of the sample surface. When the tip interacts with the sample, it experiences a local force that deflects the cantilever. By monitoring the angle of deflection of the cantilever throughout the swept, an image of the topography of the sample surface can be obtained. To detect these deflection angles, a laser beam is focused on the cantilever, in the place where the tip is. The reflected laser beam is detected by a photodetector, which is divided into four quadrants. The deflection of the cantilever causes a variation of the position of the laser spot in the photodetector, so by aligning the laser spot with the centre of the detector, any small variation of the laser spot position can be detected by comparing the different signals coming from the different quadrants. This allows the detection of the small deflection angle variations of the cantilever, thus detecting topography steps in the sample surface. By forcing the cantilever to return to its initial deflection angle, with the help of a piezoelectric material (that can be associated with the sample holder or to the cantilever), the topographic image can be obtained by mapping the quantity that the piezoelectric material had to move in the perpendicular direction to the sample plane with the position of the tip in the sample surface [52]. Depending on the application, the AFM can operate in three distinct modes: tapping, contact and non-contact.

The AFM results reported in the literature for low dimensional $MoSe_2$ show that a monolayer right above the substrate has a height of 0.7-1nm [2, 6, 19–21], and that the difference in height between a monolayer and a bilayer is about 0.6-0.7nm [19], so that the bilayer height from the substrate surface is $\sim 1.5nm$ [20].

The analysis of the samples was performed in the tapping mode, using a Digital Instruments™ microscope. The images were than treated using the NanoScope analysis and Gwyddion software. The height profiles presented in this work are the average curves of five different measurements performed along equivalent trajectories in the AFM images.

3.3.4 X-Ray Diffraction (XRD)

X-ray diffraction (XRD) is the most used technique to characterise the crystalline structure of a material. The wavelength of X-rays is comparable to the spacing between atoms in a crystal ($\sim$ 1Å), so the crystal lattice can be seen as a diffraction grating for this type of radiation. This enables the ”visualization” of the crystalline properties of a material. Considering that a crystal is composed of parallel planes of atoms separated by a distance d, X-rays scattered from different crystal planes will travel different path lengths, leading to interference. For constructive interference to occur, this difference in the path length has to be equal to an integral number of wavelengths, that is, has to satisfy the Bragg law

$$n\lambda = 2d_{hkl}sin\theta, \tag{3.12}$$

where n is the order of reflection, λ is the incident X-ray wavelength, d_{hkl} is the spacing between planes of the same hkl family and θ is the angle of incidence. In this sense, planes with the same Miller indices (hkl) are responsible for constructive interference, and different (hkl) will interfere constructively for different angles of incidence [53]. As different crystal structures have different d_{hkl} spacings, the angle of incidence for which constructive interference occurs, for each set of (hkl), is characteristic of the crystal lattice.

In an XRD experiment, the sample is rotated in relation to the incident monochromatic X-ray beam. In the case of Bragg-Brentano geometry, the detector moves on a goniometer circle which is in synchronization with the sample over a range of 2θ values. This allows the simultaneous record of both the angle and intensity of the diffracted beam. Thus, an X-ray diffraction pattern is a plot of the intensity of the diffracted beam in relation to the diffraction 2θ angle [51]. Each crystal structure presents a characteristic X-ray diffraction pattern. By comparing the X-ray diffraction pattern of an unknown material with well documented XRD patterns, one can determine its chemical composition and crystalline structure.

The diffraction peaks have a finite width, since even the most crystalline sample does not have a perfect three dimensional order. Peak broadening can be caused by finite size crystallite size and lattice strain (that changes the spacing between atomic planes). Another source of broadening comes from the instrument, due to non ideal X-ray optics, wavelength dispersion and detector resolution [51]. The determination of the width of the most intense peak (characteristic of a certain crystalline phase) can give information about the average crystallite size present in a sample. By using the Scherrer equation, an average of the crystallite size, $< \tau >$, can be obtained

$$< \tau >= \frac{K\lambda}{\beta cos\theta_{hkl}}, \tag{3.13}$$

where K is a constant whose value depends on the shape of the crystallites (usually 0.9 for spherical crystallites) and β is the peak width (in radians $2\theta_{hkl}$) that corresponds to the (hkl) reflection.

The XRD peaks of a sample can be shifted from the documented ones due to a displacement of the sample in relation to the centre of the goniometer. In order to correct this error, the following equation can be used [54]

$$\Delta(2\theta) = \frac{2x\cos\theta}{R}, \tag{3.14}$$

where θ is the measured peak position, x is the sample displacement and R is the goniometer radius. In this work, the XRD patterns of the samples presented the characteristic peak of the (111) plane of silicon displaced by a certain $\Delta(2\theta)$. Since the displacement of the sample in relation to the centre of the goniometer was unknown, the documented silicon peak corresponding to the (111) planes ($2\theta = 28.443$ (JCPDS 27-1402)) was used to estimate the value of x. Then, the displacement $\Delta(2\theta)$ for each value of θ was calculated using the previously obtained x value.

The structural characterization of the $MoSe_2$ few-layer samples was carried out by X-ray diffraction (XRD) on Philips X'Pert PRO apparatus set with a vertical PW 3050/60 goniometer ($\theta - 2\theta$ mode) equipped with X'Celerator detector and with automatic data acquisition (X'Pert Data Collectir (v2.0b) software), using a monochromatized CuKα radiation ($\lambda = 1.540598nm$) as incident beam, 40 kV - 30 mA. Diffractograms were obtained using the Bragg-Brentano configuration, by continuous scanning in a 2θ-range of 10-60° with a step size of 0.017° and scan step times of 40s. The recorded data was compared with the standard files from the "Joint Committee of Powder Diffraction Standard" (JCPDS) [55].

3.3.5 Raman Spectroscopy

When monochromatic laser light with frequency ω_i excites molecules in a sample, it transforms them into oscillating dipoles. Such oscillating dipoles can emit light of three different frequencies. If the interaction of the photon with the molecule is elastic, that is, if the excited molecule goes back to the same basic vibrational state and emits light with the same frequency ω_i, this is called the Rayleigh scattering. In the case where the scattering of the photon by the molecule is inelastic, this is called the Raman effect and two cases can occur. If the molecule is in its ground vibrational state and absorbs a photon of frequency ω_i, part of the photon energy is transferred into a Raman vibrational mode with frequency ω_0 (creation of a phonon) and the resulting frequency of the scattered light is reduced to $\omega_i - \omega_0$. This is called Stokes scattering. On the other hand, if a molecule which is already in its excited vibrational state absorbs a photon with frequency ω_i, when it relaxes to its ground vibrational state releases a photon of frequency $\omega_i + \omega_0$, which carries with it the energy of the Raman vibrational mode (annihilation of a phonon). This Raman frequency is called Anti-Stokes.

In Raman spectroscopy, the frequency due to the transitions between vibrational levels is measured in relation to the frequency of the incident monochromatic beam. As the number of molecules already in excited vibrational states, at room temperature, is orders of magnitude lower than the number of molecules in the ground state, one has that the Stokes scattering intensity is much greater than the intensity of the Anti-stokes scattering. In this way, the Raman frequency which is usually measured is the one that corresponds to the Stokes scattering [56]. Raman scattering provides information about the vibrational, rotational and other low frequency transitions in molecules, and also about the lattice vibrations in crystals.

For the analysis of $MoSe_2$ nanolayer films, Raman spectroscopy has been proven to be a powerful tool to confirm the presence of $MoSe_2$ and determine the number of layers present in each sample [19,26]. Both energy, width and amplitude of the Raman peaks are strongly influenced by the number of layers present [57]. One of the characteristics of the Raman spectra of few-layer TMD is the appearance of low energy interlayer vibrational modes that are usually not optically active in bulk crystals and have a strong dependence on the number of layers, being again absent in the monolayer [20].

The most intense peak corresponds to the A_{1g} mode, which is the out-of-plane vibration of Se atoms [2] as represented in Figure 3.8. It appears at a Raman shift of $\sim 241cm^{-1}$ for monolayer $MoSe_2$ [6, 19, 25, 58] and is blue-shifted to $\sim 242cm^{-1}$ for bi- and trilayer [2, 19, 26, 58] and to $\sim 244cm^{-1}$ for bulk $MoSe_2$ [2, 19]. The stiffening of the A_{1g} as the number of layers increases may be due to an increasing inter-planar restoring force [19, 25]. The in-plane vibration of Mo and Se atoms is associated to the E^1_{2g} mode, which appears at a Raman shift of $\sim 287cm^{-1}$ for the $MoSe_2$ monolayer [2, 19, 25, 58]. As the number of layers increases, this mode is red-shifted to lower Raman shifts, having the values of $\sim 286cm^{-1}$ for bilayer [2, 58] and $\sim 285cm^{-1}$ for bulk $MoSe_2$ [19]. A possible cause for the softening of the E^1_{2g} mode can be the presence of long-range coulomb interactions between layers. Since this two characteristic peaks are shifted with the increase of layer number, the difference between the positions of the A_{1g} and E^1_{2g} modes can be an indication of the number of layers present. For monolayer $MoSe_2$, the difference between these peaks has been reported to be in the range $45.5 - 46.9cm^{-1}$ [2, 6, 19, 25], whereas for few-layer and bulk $MoSe_2$ is $\sim 43.0cm^{-1}$ [4, 19] and $\sim 41.6cm^{-1}$ [19], respectively.

Other less intense peaks that appear in the Raman spectra of low dimensional $MoSe_2$ are the peaks corresponding to the E_{1g} mode at $\sim 168cm^{-1}$ [59], and to the B^1_{2g} at $\sim 353cm^{-1}$ [19, 20, 57, 58, 60]. The B^1_{2g} mode is inactive in bulk $MoSe_2$, but becomes weakly Raman active in bilayer and few-layer flakes due to the breakdown of translation symmetry [60]. Since this mode is due to the interaction between layers, it is absent for monolayer $MoSe_2$ and serves as confirmation for the presence of single-layer $MoSe_2$.

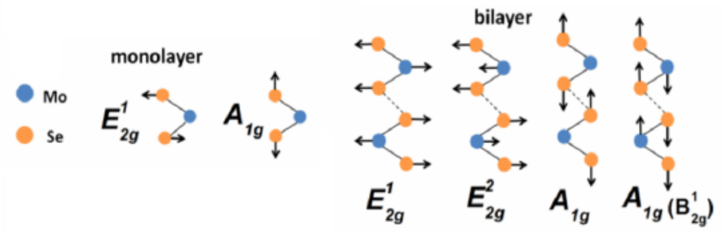

Figure 3.8: **Raman modes of mono- and bilayer $MoSe_2$.** Vibrational normal modes of mono- and bilayer $MoSe_2$. Adapted from Lu *et al* [20].

Here, the Raman spectra of the deposited $MoSe_2$ nanofilms were obtained on a LabRam HR 800

Evolution, from Horiba - Jobin Yvon, with 532 nm excitation source and a 1800 grove/mm grating. The light was focused with a 100x objective, where the laser spot was of $\sim 1\mu m^2$. The laser power on the sample was approximately 10 mW, with a penetration depth of $\sim 1\mu m$. Spectra were acquired using 10s of signal collection time and 16 accumulations. Data acquisition was performed with the LabSpec software from Jobin Yvon.

3.3.6 Photoluminescence Spectroscopy (PL)

Photoluminescence (PL) is a type of luminescence (spontaneous emission of light) that certain materials produce under light excitation. In particular, semiconductors present this kind of luminescence, since its carriers can be excited by light. When a light beam of sufficient energy is focused on a semiconductor, an electron from the valence band can be excited to the conduction band by absorbing a photon. Through recombination processes, a photon can then be emitted as the electron returns to the valence band. This spontaneous emission of photons when the electron returns to its ground state is called luminescence. In this way, the emitted photons have energy equal to the difference between excited states and ground states, and by collecting them, one can access the electronic structure of the semiconductor and determine its energy band gap. Moreover, when the semiconductor has intermediate levels in the band gap, due to impurities and/or defects, if the electron is excited to this states and then returns to the non-excited state by emitting a photon, this states can also be detected by PL. Thus, by studying the PL of a material one can access to all radiative processes that occur due to the light excitation, allowing the determination of its energy band-gap, impurity and defects levels, recombination mechanisms and quality of the material [61].

A PL spectrum is the plot of the number of photons emitted per energy. The higher the rate of a radiative transition at a certain energy, the higher the PL intensity is at that energy. In this way, the PL peaks are an indication of the existing excited states that allow a radiative recombination process. In the case of direct semiconductors, the spontaneous emission of a photon occurs quite easily since its valence band maximum has the same momentum of its conduction band minimum, and the excited electron decays into the valence band by emitting a photon of energy equal to its band gap. As this electron-hole radiative recombination occurs at a high rate, a direct semiconductor presents a well defined PL peak, with high intensity, at its band gap energy. On the contrary, in indirect semiconductors, in addition to the supply of a photon, a phonon with the right momentum and energy is also needed to excite the electron from the valence to the conduction band. This three-body recombination process (electron, hole and phonon) is significantly less likely to occur than a direct electron-hole recombination since the phonon availability is governed in part by the phonon dispersion relation. Thus, an indirect semiconductor presents a broad, much less intense, PL peak at its band gap energy [62].

The optical excitation is done by focusing a monochromatic light beam at the sample surface. The PL response depends greatly on the energy of the optical excitation, since it selects the initial photo-excited state, and on its intensity because the higher the number of carriers excited, the higher the number of photons emitted by the sample which increases the PL signal. The optical excitation can be done by focusing a laser, that has a small spot ($\sim 1\mu m^2$) and allows a detailed choice of the site of the sample surface to be analysed, or by a lamp which has a spot of a few millimeters square and allows to have an average of the PL response of the sample.

In the case of monolayer $MoSe_2$, it has been reported the PL study with laser excitation wavelengths of 514nm and 532nm. For both excitation wavelengths, a strong PL intensity at 800nm (1.55 eV) [19, 25, 60] or 794nm (1.56eV) [2, 6, 20] has been reported and corresponds to the direct band gap observed for monolayer $MoSe_2$. With increasing layer number, the PL peak is redshifted and its intensity is reduced significantly, as the band gap turns to indirect [2, 19, 60]. Finally, bulk $MoSe_2$ (layer number > 10) presents an indirect band gap of $1.1eV$ [19, 25].

In this work, the PL measurements of the $MoSe_2$ nanolayers were performed on a Spex Fluorolog spectrometer in front-face geometry in the spectral range from 650 to 850 nm under a 514.5 nm excitation from a Xenon lamp, at room temperature. The spot size is $2 \times 5mm^2$, which means that the PL peaks obtained are a consequence of the average PL of all the mono- to few-layer $MoSe_2$ present in each sample, resulting in a not so strong and broad PL peak. The PL peaks were fitted using a Gaussian function.

Chapter 4

Results and Discussion

In this chapter, the results of the oxidation of the silicon substrates and the properties of the mono- to few-layer $MoSe_2$ nanofilms deposited onto SiO_x/Si substrates by CVD will be presented and discussed.

The PL of the SiO_x/Si substrates for different excitation energies was studied to determine which excitation energy was more adequate for the PL study of the $MoSe_2$ samples. In the case of the $MoSe_2$ nanolayers, the results will be presented as a comparison of the different observed properties for each deposition parameter, in order to determine a set of deposition parameters that is adequate for the deposition of monolayer $MoSe_2$.

4.1 Oxidation of (111) Si substrates

In this section the results of the oxidation of (111)Si will be presented, as well as the photoluminescence spectra of the oxidized substrates, for four different excitation energies.

4.1.1 SiO_2 thickness

To estimate the oxidation time, equation 3.5 was rewritten to have the oxidation time t as a function of the oxide thickness x_{ox}

$$t(x_{ox}) = \frac{x_{ox}^2}{B} + \frac{A}{B}x_{ox} - \tau. \tag{4.1}$$

In all of the calculations it was assumed an initial SiO_2 thickness of $x_i = 3.0nm$ which was considered to be the naturally grown SiO_2 layer. At first, the values of B and B/A were obtained by fitting the values reported in [48] for (111)Si, to get an approximation of these constants values at a temperature of 934 °C. The obtained values were $B = 6.09 \times 10^3 nm^2/hour$ and $B/A = 27.48nm/hour$. None of the limiting cases, equations 3.10 and 3.11, were used here because $A^2/4B \approx 2hours$, which gives $x_{ox} = 48nm$, i.e. with the same order of magnitude as 90nm, implying that the time required to grow a 90nm SiO_2 layer will not be much higher than 2hours. As so, equation 4.1 gives an oxidation time of $t(90) \approx 4h30min$ to grow a SiO_2 layer of $90nm$ thickness. However, after proceeding to the oxidation of (111)Si in our setup for 4h30min, the SiO_2 layer obtained had a thickness of $160 \pm 10nm$, measured from the SEM image of its cross-section (Figure 4.1 b)). This thickness belongs to the 160-200nm range, where the contrast is low and the $MoSe_2$ monolayers will not be visible under white light illumination [44]. Unfortunately, this mistake was detected after the deposition of a few samples, samples numbered 7 to 15.

Using equation 4.1 to estime the time needed to grow 160nm of SiO_2, one obtains $t(160) = 9h55min$, which is much higher than the observed time of 4h30min in our oxidation setup. This shows that the constants B and B/A used were not appropriate. In order to estimate a more accurate oxidation time, the fitting expressions of B and B/A reported in [49] were used because they are valid for oxide thicknesses lower than 100nm and for temperatures lower than 1000 °C. These expressions are

$$B = 8.04 \times 10^{10} e^{-\frac{1.71}{k_B T}} nm^2/hour, \qquad \text{and} \qquad B/A = 7.98 \times 10^{8} e^{-\frac{1.74}{k_B T}} nm/hour, \tag{4.2}$$

where $k_B = 8.62 \times 10^{-5} eV K^{-1}$ is the Boltzmann constant. These constants give an oxidation time of $t(90) \approx 3h23min$. Before proceeding to the oxidation, it was realized that in the literature the carrier gas used was Ar [49] or N_2 [50], during the flush of the tube and the heating of the furnace. In contrast, here the gas flow used was always oxygen throughout the whole oxidation process, so there might have been SiO_2 growth during the furnace heating (that took 24min) and during cooling, while its temperature was still above 500 °C. To try to compensate these extra oxide growths, an oxidation time of 2h50min was used, and the oxide layer thickness obtained was $87 \pm 5nm$, which is close enough to the goal of 90nm. In Figure 4.1 a) the cross-sectional SEM image of the substrate can be seen. Samples 17 to 20 and samples A to D were deposited on these substrates.

The oxidation of a silicon piece with a thicker oxide layer was performed by using an oxidation time of 10h30min. The thickness obtained was of $230 \pm 11nm$, measured from the cross-sectional SEM image in Figure 4.1 c). Considering that the oxidation procedure applied in this work was not rigorous, in the way that the cleaning process of the Si pieces and the flush of the tube were not too controlled, the oxide layer may not have a perfect $1:2$ stoichiometry. Thus, from now on, the oxide layer will be considered as SiO_x, with unknown x, since the correct stoichiometry is not known.

XRD was used to confirm that the SiO_x layer was amorphous [48]. The XRD patterns for the three different SiO_x thickness are presented in Figure 4.1 d). The most intense peak at $2\theta = 28.4°$ is indexed to the (111) crystallographic direction of silicon (JCPDS 27-1402), as expected. The other peaks are much less intense ($\sim 400\times$ less intense) and may be due to strains between the crystalline Si surface and the amorphous SiO_x. At $2\theta \approx 44.6°$ there exists a broad peak with low intensity, which may be an indication of the amorphous nature of the SiO_x.

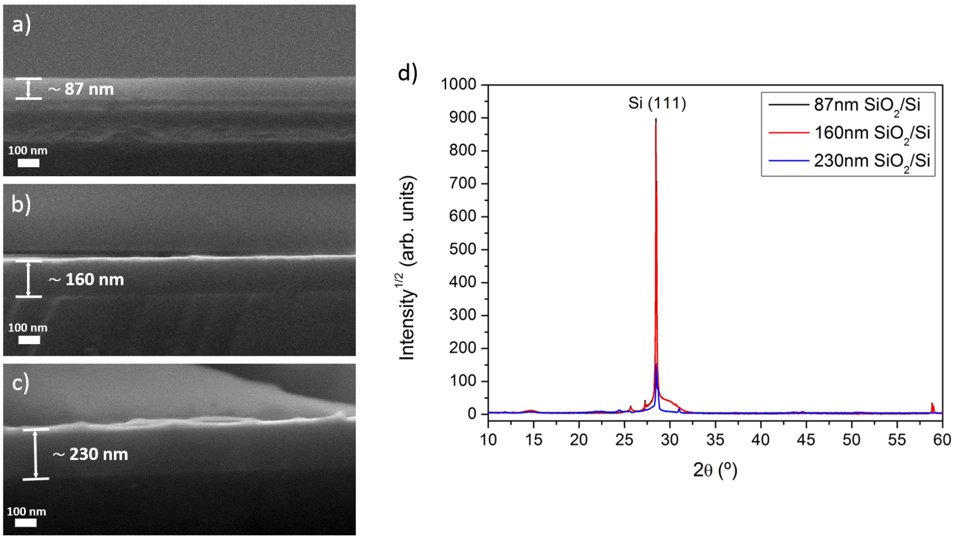

Figure 4.1: **Cross-sectional SEM images of SiO_x/Si substrates and their XRD patterns.** SEM images of the cross-section of a) 87nm, b) 160nm and c) 230nm SiO_x/Si substrates. d) XRD patterns of each substrate.

4.1.2 PL properties

While studying the PL of the $MoSe_2$ nanofilms, it was discovered that the SiO_x/Si substrates also presented efficient PL response, with PL peaks at wavelength positions similar to the ones reported for mono- to few-layer $MoSe_2$, for an excitation wavelength of 532nm. Since a blue shift of the PL peaks of the substrates was observed with an increase in excitation energy, the study of the PL for different excitation energies was performed, in order to determine which excitation energy was more appropriate to detect the PL emitted by the deposited $MoSe_2$ nanolayers.

The PL measurements were performed at room temperature in front-face geometry and for excitation wavelengths of 532, 523, 514.5 and 488nm from a Xenon lamp of spot size $2 \times 5mm^2$, as indicated in subsection 3.3.6. It is worth noting that this large spot size will provide the study of the PL coming from a macroscopic area of the samples, instead of a local PL.

The PL spectra of the SiO_x/Si samples and of a (111) Si piece, for four different excitation energies, are plotted in Figure 4.2. For $\lambda_{ex} = 532nm$, all samples present a PL peak at $\sim 800nm$ (1.55 eV) with high PL intensity and full width at half maximum (FWHM) of 8nm. Two more peaks, broader and with lower PL intensity, can be observed at $\sim 725nm$ (1.71 eV) and at $\sim 682nm$ (1.82 eV), except for the 230nm SiO_x/Si sample, where this last peak appears for wavelengths lower than 650nm. Increasing the excitation energy causes the PL peaks to shift to lower wavelengths, decreasing their PL intensities but maintaining their FWHM constant.

For $\lambda_{ex} = 523nm$, the peak previously at $\sim 800nm$ is shifted to $\sim 785nm$ (1.58 eV), and its intensity decreases about 5×, except for the 160nm SiO_x/Si sample where its intensity decreases about 10×. The higher energy peaks blueshift to $\sim 675nm$ (1.84 eV) and $\sim 711nm$ (1.74 eV), and their intensities also decrease. The samples with higher SiO_x thickness, 160nm and 230 nm, do not display the highest energy peak in the range 650-750nm. Decreasing the excitation wavelength to $\lambda_{ex} = 514.5nm$, the peaks are again blueshifted for the peak positions $\sim 773nm$ (1.60 eV) (PL intensity 2× lower), $\sim 700nm$ (1.77 eV) and $\sim 669nm$ (1.85 eV). Again, the samples with higher SiO_x thickness do not have this last peak.

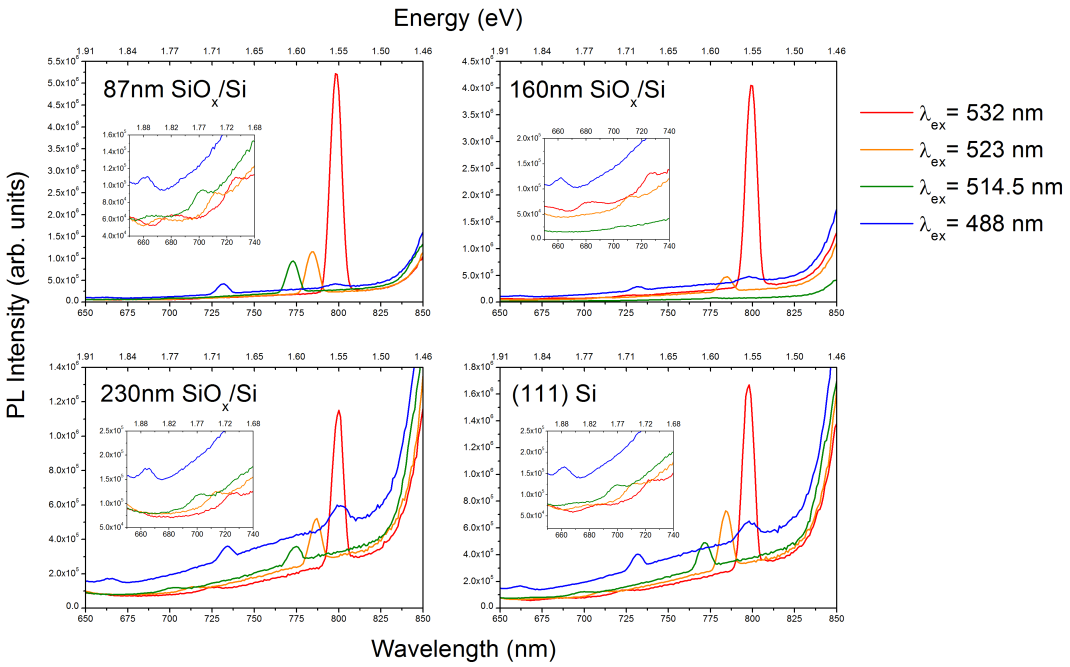

Figure 4.2: **PL spectra of SiO_x/Si samples.** PL spectra of SiO_x/Si samples for four different excitation wavelengths, in the range 650-850nm, where the insets show a zoom of the range 650-740nm. The color legend is the same for all plots.

Finally, for $\lambda_{ex} = 488nm$ a peak at $\sim 800nm$ (1.55 eV) is again observed, additionally to the presence of two peaks at $\sim 732nm$ (1.69 eV) and $\sim 662nm$ (1.87 eV). These two last peaks are thought to be the blueshifted ones, since the PL intensity of the $\sim 732nm$ peak is $2\times$ lower than the PL intensity of the peak observed at $\sim 773nm$, for $\lambda_{ex} = 514.5nm$, and the FWHM of both peaks is equal to 8nm. The peak observed at $\sim 800nm$ is broader and has lower PL intensity than the one observed at the same peak position for $\lambda_{ex} = 532nm$.

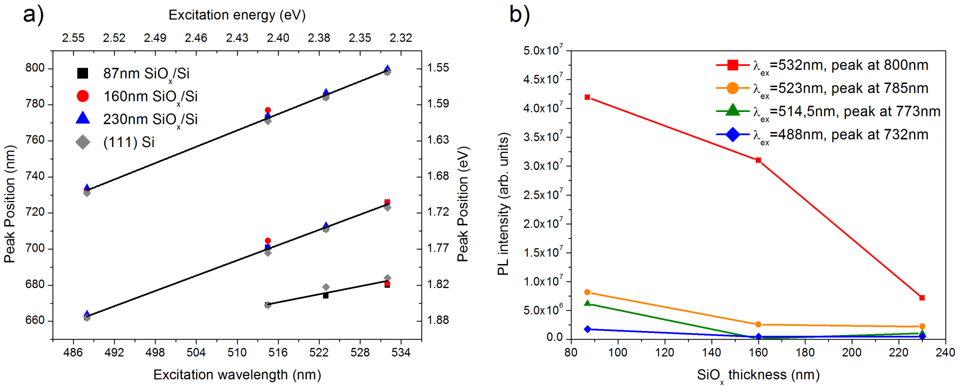

Figure 4.3: **PL results for SiO_x/Si samples as a function of excitation energy and SiO_x thickness.** a) Plot of PL peak positions as a function of excitation energy for the three SiO_x/Si substrates and a (111) Si piece, where the black lines are the linear fits to the experimental data. b) Plot of the variation of the PL intensity of the highest intensity peak with SiO_x thickness, for the four excitation energies used.

Plotting the peak position as a function of excitation energy for the four analysed samples, Figure 4.3 a), one can see that the peak position wavelength increases linearly with the increase in excitation wavelength, for the three observed PL peaks. Fitting linear functions to the data shows that the peaks at $\sim 800nm$ and at $\sim 725nm$ (for $\lambda_{ex} = 532nm$) are blueshifted with the increase in excitation energy following straight lines with similar slopes of 1.51 and 1.41, respectively. This might be an indication that these peaks are blueshifted due to the same phenomenon. The slope of the linear function fitted to the data of the highest energy peak observed is 0.74, which is much different than the fitted linear functions to the data of the other two peaks. This can be due to lack of data, since this last peak was out of the 650-850nm wavelength range for the samples 160nm SiO_x/Si (for $\lambda_{ex} = 514.5nm$) and 230nm SiO_x/Si (for $\lambda_{ex} = 523$ and 514.5nm), and for all samples for the excitation energy of 488nm.

The different samples have the PL peaks at the same peak positions (with fluctuations of $\pm 2nm$) for all of the E_{ex} used, however the PL intensities are different. The plot of the PL intensity of the highest intensity peak for all E_{ex} as a function of SiO_x thickness is shown in Figure 4.3 b). It shows that the PL intensity decreases with the increase of the SiO_x thickness, for the four excitation energies studied, which might be an indication that the PL comes from the $SiO_x - Si$ interface. Moreover, it also shows that the peaks have higher PL intensity for lower excitation energies.

These results are surprising because bulk silicon is regarded as a poor light emitter, with low photoluminescence in the visible range (particularly in the red and infra-red region), as a consequence of it being an indirect semiconductor [63]. The fact that phonons are needed in optical band to band transitions decreases greatly the rate of radiative recombination processes. Thus, the best expectation was to observe a peak at 1088nm (1.14 eV) with very low PL intensity corresponding to its indirect energy band gap, and no PL response in the visible range.

In the literature, the existence of efficient PL in the red and near-infrared range for silicon based materials has only been reported for porous silicon (silicon quantum dots) [64, 65], Si nanocrystals embedded in an SiO_2 matrix [66–69], and thin films of silicon-rich silica (SiO_x, $x < 2$) [70, 71]. The visible

PL observed in these silicon structures is usually attributed to quantum confinement, surface states, defects in the oxide, radiative states in the SiO_x-Si interface [72] and light emitters located in the involving silicon oxide layer [73] or in the Si nano clusters [72]. However, a correct interpretation of the red and near-infrared PL has yet to be established.

Although the mentioned reports may provide a first interpretation of what is observed in the SiO_x/Si samples produced, their studies are performed with higher excitation energies (E_{ex} in the range 325-488nm) from a laser source and the peak shifts are studied as a function of the size of the Si nanocrystals (or quantum dots). A blue shift of the PL peaks is observed with decreasing Si nanocrystal sizes, which is interpreted as an effect of quantum confinement. Even the thin films of silicon-rich silica, which may be close to our SiO_x layer, are considered as Si nano clusters embedded in a SiO_x matrix, and the PL peaks are studied as a function of annealing time, which is interpreted as influencing the size of the Si clusters. Therefore, finding relations between the results obtained in this work and those reported is not easy.

As previously discussed, the oxidation procedure implemented here was not strictly controlled, producing oxide layers of unknown stoichiometry, and probably promoting the appearance of structural defects at the SiO_x-Si interface. These defects might be due to a non-uniform oxide growth that promotes the growth of an inhomogeneous oxide layer, with regions richer in silicon and others richer in oxygen. One could interpret the silicon rich regions as Si clusters, in analogy with the thin films of silicon-rich silica. Actually, it has been reported the presence of Si nanocrystals of average size 2nm, randomly distributed throughout an amorphous silicon oxide layer, thermally grown by wet oxidation, which exhibits visible PL in the violet and yellow regions, at room temperature, when excited by a laser of wavelength 364nm, after it is subjected to rapid thermal annealing treatments [74]. In order to understand if the PL emitted by the SiO_x/Si substrates comes from quantum confinement of silicon nano clusters at the SiO_x-Si interface, the annealing of the samples in Ar atmosphere could be performed, and the effect of different annealing times on the emitted PL could be studied. This study could also be performed for higher excitation energies and for a broader range of wavelengths. Furthermore, the confirmation of the fact that the oxide layer of SiO_x/Si substrates is or isn't composed of Si nano clusters embedded in a silicon matrix, could be done by performing cross-sectional high-resolution transmission electron microscopy (HRTEM), which also allows to determine the size of such Si nano clusters. However, this interpretation does not explain the fact that the PL peaks measured have lower FWHM than the ones reported for the Si nanocrystals. The explanation given for the presence of broad PL peaks is the existence of Si clusters of several sizes, which emit PL at different wavelengths. In the present case, the low FWHM could indicate the presence of Si clusters of similar size, which is highly unlikely. Therefore, there must be another explanation for the photoluminescence measured in the SiO_x/Si substrates.

The answer for a correct interpretation of the PL results must be in the decrease in PL intensity with the increase of the SiO_x layer thickness and in the blue shift observed with the increase in excitation energy. The influence of the oxide layer thickness in the PL intensity and not in the peak position or FWHM indicates that the emission of the PL comes from the SiO_x-Si interface and that the "extra" SiO_x layer camouflages the PL emission. In order to understand if the PL emission is due to the interface between silicon and silicon dioxide, the PL measurements in the same conditions were performed in amorphous silicon (a-Si) thin films deposited by pulsed laser deposition (PLD) on fused silica and MgO substrates. These films were produced by C. Almeida Marques and Isabel A. Lopes in the project *Production and Characterization of silicon nanofilms by PLD, for thermoelectric applications*, LSPL, 2013. The silicon thin films deposited in fused silica exhibit PL peaks at the same positions as the SiO_x/Si substrates, with the same FWHM of 8nm, but with lower PL intensities. Figure 4.4 a) shows the PL spectra of a 150nm

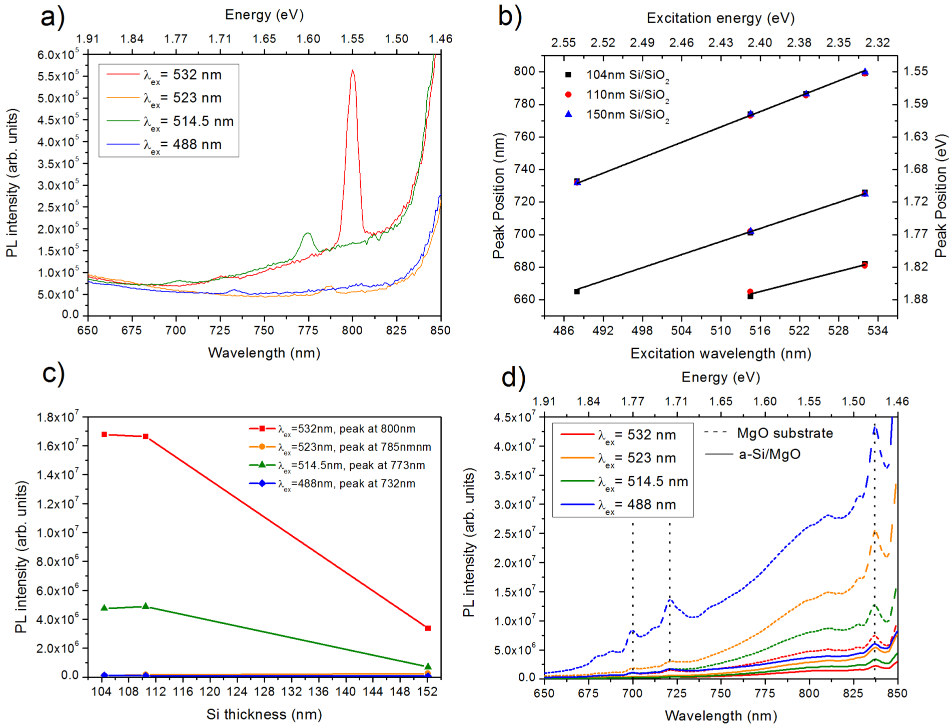

Figure 4.4: **PL measurements for a-Si thin films** a) PL results for an a-Si thin film with 150nm thickness, deposited on fused silica, for four different excitation energies. b)Plot of the peak positions as a function of excitation wavelength. c) Plot of the PL intensity of the most intense peak as a function of the thickness of the a-*Si* thin films. d)PL spectra for a MgO substrate (dash line) and for an a-Si thin film deposited on MgO substrate (line), for four different excitation energies. The vertical dot lines indicate the position of the three most intense PL peaks.

thickness a-Si thin film on fused silica, for the four different excitation energies. The same blue shift with excitation energy is observed, and in Figure 4.4 b) one can see that for three samples with different silicon thickness the variation of the PL peaks position with the excitation energies follows a straight line, as observed previously. Also, a decrease in PL intensity was observed for an increase in Si thin film thickness (Figure 4.4 c)), which is an indication that the emitted PL comes from the interface silicon oxide-silicon. As the PL response of a fused silica substrate is almost none in the studied region[1], these experiments clearly indicate that the PL emission comes from the interface between silicon and silicon oxide. To further support the previous hypothesis, the study of the PL of an a-Si thin film on MgO substrate was performed. The PL spectra of this sample is shown in Figure 4.4 d), and one can see that this sample (continuous line) has a completely different PL spectrum than the previous SiO_x/Si samples, with peaks at different positions, identical to the PL response observed for a pristine MgO substrate (dash line). This film does not exhibit the blue shift with excitation energy, and a higher excitation energy is only responsible for altering the PL intensity. Actually, the only influence of the a-Si thin film in the PL spectra of the sample is the decrease in PL intensity shown by the sample in comparison to the PL spectra of the MgO substrate alone. This supports the hypothesis that the light emitters have to be in the interface between silicon (crystalline or amorphous) and silicon oxide, and that the PL is not due to the presence of light emitters in the bulk silicon oxide nor in the bulk silicon thin films.

The blue shift exhibited by the two types of samples with increasing excitation energy can be due to changes in occupancy of low-energy states caused by the increasing excitation energy, which increases

---

[1] The PL spectra of a pristine fused silica substrate was also studied, but no emission was detected for $\lambda_{ex} = 523$, 514.5 and 488nm. For $\lambda_{ex} = 532$nm, a PL peak at 800nm is observed, with intensity 20× lower than the PL peak observed for the a-Si/SiO_2 thin films.

the average energy of carriers that are involved in the radiative recombination processes [75]. For a low excitation energy, the observed PL originates predominantly from the lowest excited states. Upon increasing the excitation energy, high energy excited states can be filled, and the radiative recombination processes occur emitting photons with higher energy [69]. The recombination times for the higher excitation states are much longer than for the lowest excitation states [69], causing a low recombination rate for high excitation states, which explains the lower PL intensity observed for higher excitation energies. However, although this might explain the observed shift, the energy states responsible for the PL are not known. There are some reports that suggest that the red and near-infrared PL from silica-based nanoscale materials and Si-rich SiO_2 films [72] is due to non-bridging oxygen combined with structural defects, like oxygen vacancies. This could be the case of the studied samples, because the existence of structural defects like oxygen vacancies is highly probable for both types of samples. To determine the correct mechanisms responsible for the observed PL, a careful study of the energy states present at the $SiO_x - Si$ interface is necessary, as well as the study of the PL decay times, which would help to understand the types of radiative recombination processes involved. In order to obtain more accurate results, the PL measurements in the same conditions should be performed for several samples with the same SiO_x thickness, so that a statistical treatment could be performed.

The presence of a PL peak at 800nm for an $\lambda_{ex} = 488nm$ in all samples can be due to heating effects [75]. The heating of the sample due to a high excitation energy (488nm) may enable the occupation of lower energy states, by providing extra phonons, provoking luminescent effect due to heat. In our case, this heating effects makes the electrons occupy the previous occupied low energy excited states (that were occupied at $\lambda_{ex} = 532nm$) enabling radiative recombination. To confirm this, one should investigate what happens for higher excitation energies, to see if the broad peak at 800nm continues to appear and if its intensity increases.

Additionally to what has been discussed, all of the research reports mentioned use laser beams as the excitation source. In our case, a Xenon lamp is used as the excitation source, which has a larger spot size. It has been reported that higher PL efficiencies are measured if the incident light illuminates a larger area ($10 \times 4mm^2$) rather than being focused [63], which can be explained by the fact that with focused illumination, a larger fraction of carriers diffuse away from the illuminated area into non-excited regions, where non-radiative recombination can occur [63].

The study of the PL of the SiO_x/Si substrates was important because the observed PL peak at 800nm for an $\lambda_{ex} = 532nm$ is in the same position as the PL peak reported for monolayer $MoSe_2$. This means that the excitation energy of 532nm is not suitable for the study of the PL response of the $MoSe_2$ samples. As the reported PL peak for $MoSe_2$ nanofilms corresponds to its energy band gap, its position will not shift for different excitation energies. In this way, an excitation energy of 514.5nm was chosen to study the PL of the $MoSe_2$ samples, because its most intense peak is at 773nm, which is shifted enough to enable the detection of the $MoSe_2$ peak at 800nm.

4.2 Deposition of $MoSe_2$ nanofilms

The first deposition experiments used sapphire substrates, that showed the presence of triangles, pyramids and macroscopic crystals visible by optical microscopy. However, EDS studies never detected the presence of selenium in neither of these structures, and Raman spectroscopy revealed that the crystals were MoO_2 and that the triangles and pyramids were defects of the sapphire substrate created by thermal strain due to the high heating rate and fast cooling process. This indicated that the chemical reaction between the MoO_3 and Se vapours was not efficient at the sapphire substrate surface, in our experimental setup. Therefore, oxidised silicon substrates were used, and the presence of $MoSe_2$ was usually detected.

In this section, the properties of the $MoSe_2$ nanolayers deposited onto SiO_x/Si substrates by CVD will be presented and discussed. All experiments were preformed with the same setpoint temperature, heating rate, flush, heating and cooling gas flow rate, as discussed in the previous chapter. The Raman and PL results of samples 5 to 20 are resumed in table 5.1 in Appendix A.

4.2.1 Substrate position

In the literature, the deposition of low dimensional $MoSe_2$ is reported for different substrate positions. Some authors report the synthesis of monolayer $MoSe_2$ by putting the substrate with the SiO_x face down over the MoO_3 boat [19,21], while others report that the deposition of $MoSe_2$ triangles happens when the substrate is a few centimetres away from the MoO_3 powder on the downstream side, either at the bottom of the quartz tube with the SiO_x face up [2,20] or over a quartz boat [7].

Here, three different substrate positions were studied to determine which position worked best for our setup. In sample 5, the substrate [2] was placed over the MoO_3 boat, with the SiO_x face down; in sample 6 it was put at the bottom of the MoO_3 boat on the downstream side of the powder, with the SiO_x face up; and in sample 7 it was placed over an empty quartz boat with the SiO_x face down, 1cm away from the MoO_3 boat (in the same way as represented in Figure 3.2). For all three samples, 0.20g of MoO_3 and of Se powders were used, the setpoint temperature was 800 °C, the heating rate was 40 °C/min, the deposition flow was a mixture of $\phi_{Ar} = 50sccm$ and $\phi_{H_2} = 10sccm$ (16.7% of H_2) and the deposition time was 15min. The temperature of the precursors and of the substrates was the same as discussed in subsection 3.1.1 for all depositions.

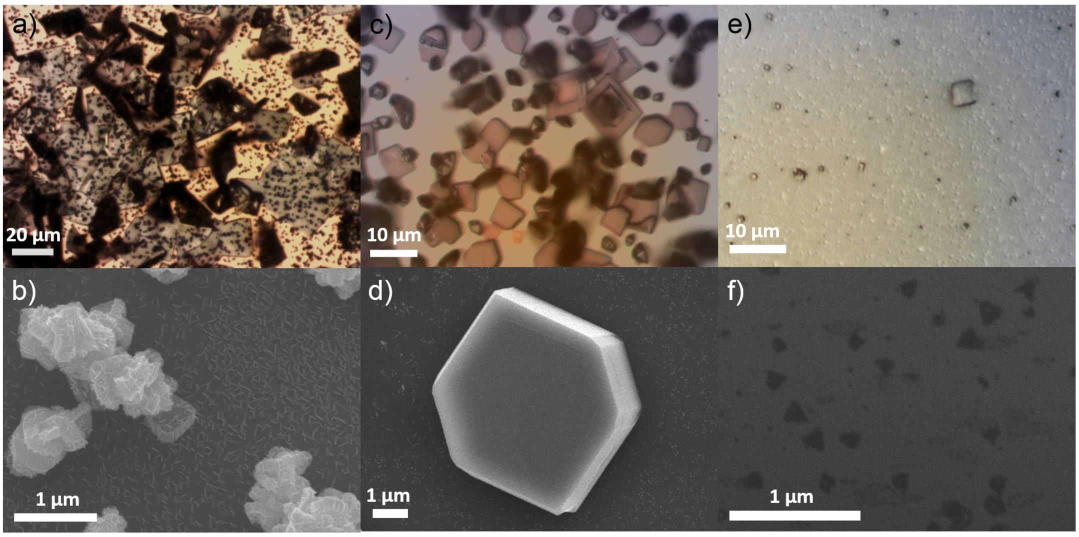

Figure 4.5: **Optical and SEM images of samples 5 - 7.** a) and b) are the optical and SEM images of sample 5, c) and d) of sample 6 and e) and f) of sample 7, respectively.

Figure 4.5 shows the optical and SEM images of samples 5 - 7. After the deposition, sample 5 presented a circular pattern, made of concentric rings with different colors, centred where the MoO_3 powder was positioned. An optical image of the centre of the circular pattern is shown in Figure 4.5 a) where different structures can be found: large plates with lateral sizes as large as 50 μm, dark crystals with high aspect ratio and small black dots with sizes $\sim 1\mu m$. The SEM image shown in Figure 4.5 b) is a close up image of one of the plates, which reveals that its surface has small oriented nanosheets, and also

---

[2] The substrates used in samples 5 and 6 were oxidised (100) Si wafers.

that the black dots are crystalline clusters. EDS study revealed that both the plates and the black dots had molybdenum and selenium (in addition to silicon and oxygen, due to the depth where the characteristic X-rays form). The optical image of sample 6 (Figure 4.5 c)) shows the presence of hexagonal crystals (edge $\sim 2\mu m$), rectangle plates and plates with a thick frame. In Figure 4.5 d), a close up SEM image of one of the hexagon crystals shows that its surface is smooth (as opposed to the plates found in sample 5), and EDS studies only showed the presence of Mo, Si and O atoms. In the case of sample 7, the optical image, Figure 4.5 e), only shows tiny plates with sizes between $1-2\mu m$ and a somewhat rough background. Surprisingly, the SEM image revealed the presence of triangles with different lateral sizes (between $100-200nm$), which were responsible for the roughness of the background seen in the optical image. EDS only showed the presence of Si and O atoms, which is possibly due to the small quantity of Mo and Se atoms present in such thin structures.

To give an insight of which crystal structures were present in each sample, XRD was performed. The XRD patterns of the three samples are shown in Figure 4.6, where the diffraction peaks at about $2\theta \approx 13.7°$, $27.6°$ and $41.9°$ are indexed to the planes (002), (004), and (006) of 2H-$MoSe_2$ (JCPDS 29-0914), respectively, and the peaks at about $2\theta \approx 18.4°$, $26.0°$, $37.4°$, $53.1°$, $53.5°$, $53.6°$, $53.9°$ and $57.4°$ are indexed to monoclinic MoO_2 (JCPDS 32-0671). Sample 5 has a mixture of crystalline 2H-$MoSe_2$ and monoclinic MoO_2, with larger MoO_2 quantity than $MoSe_2$ due to the difference in peak intensity and higher MoO_2 crystallite sizes due to a smaller FWHM of the most intense MoO_2 diffraction peak at $2\theta \approx 37.3°$. In the case of sample 6 only MoO_2 diffraction peaks are observed, indicating that if $MoSe_2$ is present, it must be in extremely small quantities. The XRD pattern of sample 7 shows small intensity peaks that correspond to the (-101) and (-202) planes of monoclinic MoO_2, suggesting that the tiny plates observed in the optical images of sample 7 are MoO_2 crystals.

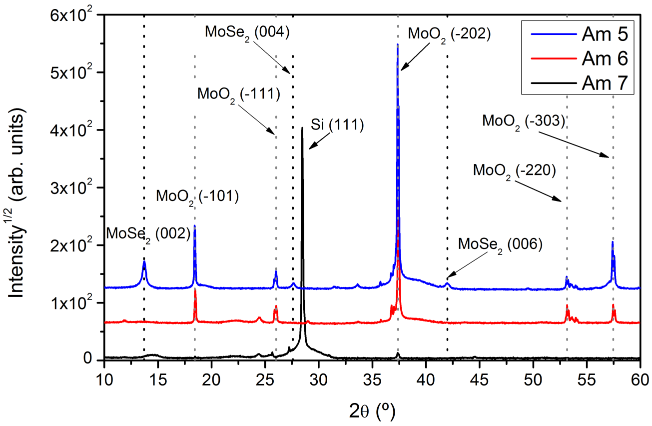

Figure 4.6: **XRD patterns of samples 5-7.** X-ray diffraction patterns of samples 5, 6 and 7, where the dashed vertical lines indicate the positions of the indexed peaks of 2H-$MoSe_2$ and monoclinic MoO_2.

XRD detects contributions from a large area of the sample surface so that it is impossible to determine which structures observed in the optical and SEM images corresponds to the observed diffraction peaks. To confirm the presence of $MoSe_2$ in the samples, Raman spectroscopy was used, because it detects the vibrational modes characteristic of different molecules, allowing the detection of small quantities of material. Furthermore, as it uses a laser beam as excitation source, a local study can be performed. In Figure 4.7 the Raman spectra of the three samples are shown.

For each sample, the Raman spectrum of a crystal and of the background was studied, in order to determine the composition of the crystal plates, complementing the information obtained by XRD, and to understand if a thin continuous film (at least as seen by optical microscopy) had been deposited in the cases of samples 5 and 6. As sample 7 has a background composed of tiny triangles, the Raman spectrum of the background was performed to see if it had the characteristic Raman peaks of monolayer $MoSe_2$. Since the laser spot is $\sim 1\mu m^2$, contributions from different triangles will appear.

Figure 4.7 a) shows the Raman spectra of sample 5 obtained for a large plate (C) and for the surrounding bright area (B, background). The large plate has Raman peaks at 168.1, 241.6 and 285.0 cm^{-1} that can be attributed to the E_{1g}, A_{1g} and E^1_{2g} modes of $MoSe_2$, respectively. The difference between the positions of the E^1_{2g} and A_{1g} modes is equal to 43.4 cm^{-1}. The peak positions plus the difference between the E^1_{2g} and A_{1g} modes are similar to the values reported for few-layer $MoSe_2$. However, the absence of the characteristic peak from the silicon substrate at 520.6cm^{-1} together with the the absence of the B^1_{2g} mode at 353cm^{-1}, which is inactive in bulk $MoSe_2$, indicates that the observed plates at the centre of sample 5 are bulk $MoSe_2$. The Raman spectrum of the background has peaks at 168.7, 241.8, 283.2 and 349.1 cm^{-1} which are attributed to $MoSe_2$, and a peak from silicon at 520.6 cm^{-1}, which has a high intensity, indicating that the $MoSe_2$ present is really thin. The difference between the E^1_{2g} and A_{1g} modes is 41.4cm^{-1}, which is close to the value reported for bulk $MoSe_2$. The SEM images taken to the surrounding area of the plates (not shown) don't show the presence of triangles but of star-like/hexagonal thin plates that are deposited at random orientations in the sample. From this results, one sees that the crystal plates at the centre of sample 5 are responsible for the $MoSe_2$ peaks that appear in the XRD pattern, and that the MoO_2 XRD peaks must come from other types of crystalline structures that appear in the other concentric rings present in the sample surface.

The Raman spectra of sample 6 for two distinct regions is shown in Figure 4.7 b). The background of sample 6 has Raman peaks at 167.8, 240.6 and 286.6cm^{-1}, which correspond to the E_{1g}, A_{1g} and E^1_{2g} modes of $MoSe_2$. The difference in Raman shift between the E_{1g} and A_{1g} modes is equal to 46cm^{-1}, which is similar to the value reported for monolayer $MoSe_2$. Moreover, the B^1_{2g} mode is absent, which sustains the idea of a monolayer film deposited directly on the substrate surface. The presence of low-intensity peaks at 125.8, 201.5 and 226.2cm^{-1}, corresponding to MoO_2, might be due to the black dots that are randomly distributed through the substrate surface. The Raman spectrum of the hexagonal crystal (H) reveals a mixture of $MoSe_2$ and MoO_2 peaks. The Raman peaks at 168.8, 241.7, 285.0, 350.0cm^{-1} are consistent with the values reported for few-layer $MoSe_2$. The peaks at 126.3, 202.6, 208.2, 229.3, 344.4, 363.5, 467.9, 496.5, 569.9 and 586.3 cm^{-1} can be attributed to monoclinic MoO_2 [76]. This suggests that the hexagonal crystal is a MoO_2 monoclinic crystal, deposited above the $MoSe_2$ film. A similar Raman spectrum is obtained for the plates observed in the optical image. This confirms the results obtained by XRD in the way that the MoO_2 peaks present in the XRD pattern of sample 6 must be due to the hexagonal crystals and crystal plates.

In the case of sample 7, the Raman spectrum of one of the crystals found on its surface, Figure 4.7 c)

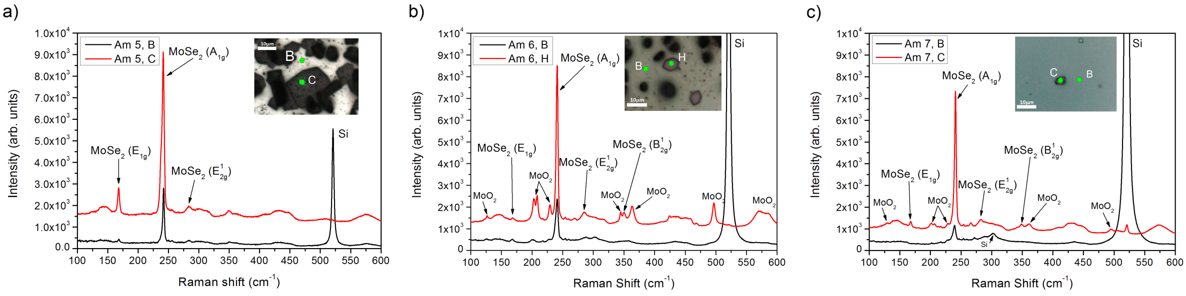

Figure 4.7: **Raman spectra of samples 5-7.** Raman spectra of the background (B) and of a plate (C) in a) sample 5, b) sample 6 and c) sample 7.

(C), also has peaks from $MoSe_2$ and from MoO_2, again suggesting the growth of MoO_2 crystals above a film of $MoSe_2$. This confirms what was said previously about the XRD pattern of this sample, in which the peaks corresponding to monoclinic MoO_2 were due to the crystal plates. The Raman spectrum of the background only has the contributions from the substrate, at 302.4 and 520.6cm^{-1}, and from $MoSe_2$ at 240.6 and 287.6cm^{-1}, close to the values reported for monolayer $MoSe_2$. This indicates that the triangles observed in the SEM image in Figure 4.5 f) are monolayer $MoSe_2$. This was confirmed by AFM, as will be discussed in subsection 4.2.2.

These results show that the most suitable substrate position for the growth of mono- to few-layer $MoSe_2$ in our experimental setup is the position used in sample 7, where triangles with small lateral sizes were found in the SEM images and Raman spectroscopy allowed to assign them to $MoSe_2$. Furthermore, this was the sample with a lower density of microscopic $MoO_2/MoSe_2$ crystals along its surface, showing that the growth of large crystals or plates is less probable at this substrate position. This might be due to a smaller concentration of MoO_{3-x} vapours along the substrate width, which decreases with the distance from the MoO_3 boat. The closer the substrate is from the MoO_3 powder, the higher is the concentration of MoO_{3-x} vapours, implying that if the selenium concentration is not high enough, the growth of MoO_2 crystals will be promoted. Another reason for the growth of triangles at the substrate position in sample 7 instead of sample 6 might be due to a smaller boundary layer in the former case, because the cross-sectional area crossed by the vapours is lower for sample 7, as discussed in subsection 2.2.2. This implies that the rate-limiting step is the surface reaction process, as desired, instead of the mass transport process [18] which is what might have happened for sample 6. In the case of sample 5, the cross-sectional area was similar to sample 7, but as the substrate was right above the MoO_3 powder, when it started to evaporate, the MoO_{3-x} molecules were quickly adsorbed on the substrate surface promoting the growth of 3D crystals.

4.2.2 H_2 percentage

In the previous experiments, it was observed the deposition of a significant amount of black powder at the bottom of the quartz tube that was identified as molybdenum (Mo) by XRD. This could be an indication of an overly reduced MoO_3 vapour due to a high H_2 percentage in the total gas flow, causing the formation of Mo which forms a solid at the working temperature. Once the Mo is in the solid state, it will not react with Se, hindering the formation of $MoSe_2$ at the substrate surface. To determine which percentage of H_2 was more adequate for the deposition of low dimensional $MoSe_2$, a study with the

Table 4.1: **Deposition parameters used in samples 7 - 9.** Resume of the deposition parameters used in samples 7, 8 and 9. All of the other deposition parameters are the ones discussed in Subsection 3.1.1.

Sample	m(MoO_3) (g)	m(Se) (g)	Substrate	T(substrate) (°C)	Flow	%H_2
7	0.20	0.20	160nm SiO_x/Si	790	Ar (50sccm) + H_2 (10sccm)	16.67
8	0.20	0.20	160nm SiO_x/Si	790	Ar (55sccm) + H_2 (5sccm)	8.33
9	0.20	0.20	160nm SiO_x/Si	790	Ar (58sccm) + H_2 (2sccm)	3.33

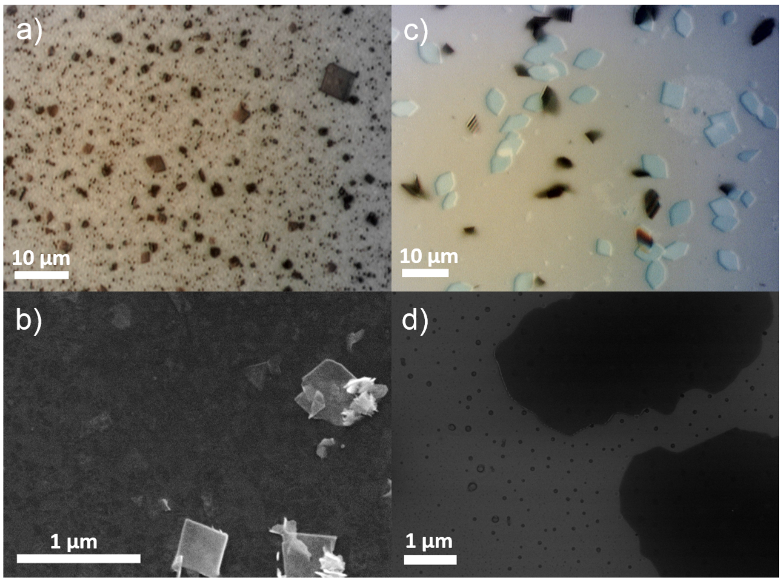

Figure 4.8: **Optical and SEM images of samples 8 and 9.** a) and b) are the optical and SEM images of sample 8 and c) and d) of sample 9, respectively.

decrease in H_2 percentage in the total flow was performed. Samples 8 and 9 were deposited using the same parameters as sample 7, while reducing the H_2 percentage from 16.67 % to 8.33 % and 3.33%, respectively. A resume of the deposition parameters can be found in Table 4.1.

The optical and SEM images of samples 8 and 9 are shown in Figure 4.8. The optical images show that sample 8 (Figure 4.8 a)) has a higher density of deposited plates and dark crystals than sample 7 (Figure 4.5 e)). In sample 9 (Figure 4.8 c)), the crystal structures deposited are blue hexagons of different sizes and dark crystals different from the ones observed on the other samples. The SEM images revealed the presence of an almost continuous thin film made of tiny triangles in sample 8 (Figure 4.8 b)), different from the ones observed for sample 7 (Figure 4.5 f)). The SEM image of sample 9 (Figure 4.8 d)) only shows the presence of small dots which might be defects on the surface of the SiO_x/Si substrate.

The XRD patterns of each sample are shown in Figure 4.9. No XRD peaks indexed to $MoSe_2$ were found in either of the samples, which indicates that the $MoSe_2$ structures present in samples 7 and 8 (and possibly in sample 9) have small sizes and heights, and cannot be detected by XRD. Samples 8 and 9 have peaks at $2\theta \approx 18.4°$, $37.4°$ and $57.4°$ indexed to the planes (-101), (-202) and (-303) of monoclinic MoO_2 (JCPDS 32-0671), respectively, and at $2\theta \approx 25.7°$, $27.3°$ and $58.9°$ indexed to the planes (040), (021) and (081) of orthorhombic MoO_3 (JCPDS 5-0508), respectively. Sample 7 has the peaks at $2\theta \approx 18.4°$, $27.3°$ and $37.4°$, but with less intensity than the ones present in the other two samples. The presence of XRD peaks indexed to MoO_3 suggest the presence of residual MoO_3 that did not react during the deposition process.

Figure 4.10 shows the Raman spectra of samples 8 and 9, of a crystal plate and of the background of each sample. The Raman spectra of sample 7 (Figure 4.7 c)) has already been discussed in subsection 4.2.1, where the crystal plates present peaks characteristic of monoclinic MoO_2 and of $MoSe_2$, and the background has only peaks corresponding to monolayer $MoSe_2$ and to the SiO_x/Si substrate. In sample 8 (Figure 4.10 a)), the crystal plate has Raman peaks at the positions 127.1, 202.0, 207.4, 227.358, 343.5, 362.223, 458.1, 495.1, 568.6 and 584.3 cm^{-1} corresponding to monoclinic MoO_2. It also presents a peak at 240.0 cm^{-1}, corresponding to $MoSe_2$, but with lower intensity than the MoO_2 peaks. On the contrary, the background of sample 8 only has peaks corresponding to $MoSe_2$, except for the peak of

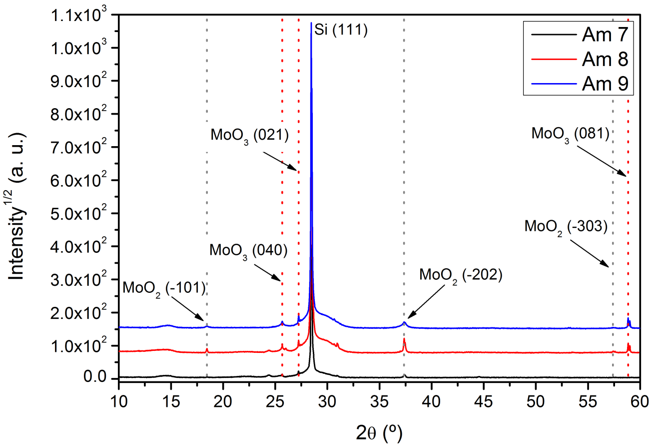

Figure 4.9: **XRD patterns of samples 7 - 9.** X-ray diffraction patterns of samples 7, 8 and 9, where the dashed vertical lines indicate the positions of the indexed peaks of monoclinic MoO_2 and orthorhombic MoO_3.

silicon at $520.0 cm^{-1}$. The peaks at 169.9, 240.0, 285.2 and 351.5 cm^{-1} correspond to the E_{1g}, A_{1g}, E^1_{2g} and B^1_{2g} modes of $MoSe_2$, respectively. The difference between the E^1_{2g} and A_{1g} modes is 45.1 cm^{-1}, which is near the interval of values reported for monolayer $MoSe_2$ [6]. However, this result together with the value of the E^1_{2g} mode (which is near the value for bulk $MoSe_2$) and the presence of the B^1_{2g} mode indicates the probable presence of few-layer structures. Again, Raman spectroscopy confirms that the XRD peaks indexed to monoclinic MoO_2 are due to the crystal plates observed at the surface of both samples.

Interestingly, the Raman spectrum of sample 9 (Figure 4.10 b)) shows that neither the blue hexagon crystals nor the background have $MoSe_2$. The Raman spectrum of the background matches the Raman spectrum of the SiO_x/Si substrate, indicated by the dash green line in Figure 4.10 b). The blue hexagon crystals, which are not regular hexagons, have Raman peaks at 123.5, 202.0, 229.2, 346.1, 362.2, 459.8, 496.8, 574.3 and 589.4 cm^{-1} attributed to bulk monoclinic MoO_2. These results show that a percentage of 3.33 % of H_2 in the total deposition flow is not sufficient to promote the reaction between the selenium and molybdenum oxide vapours, occurring only sufficient reduction of MoO_3 to MoO_2 to deposit crystalline structures of monoclinic MoO_2.

AFM was used to determine the height of the triangular structures seen in the SEM images of samples 7 and 8 (Figures 4.8 b) and d)). Figure 4.11 shows the AFM images of samples 7 and 8 together with height profiles taken along the white lines represented in the images. The AFM image of sample 7 (Figure 4.11 a)), reveals the presence of triangles with rounded vertices (lateral sizes ~ $100 nm$), where

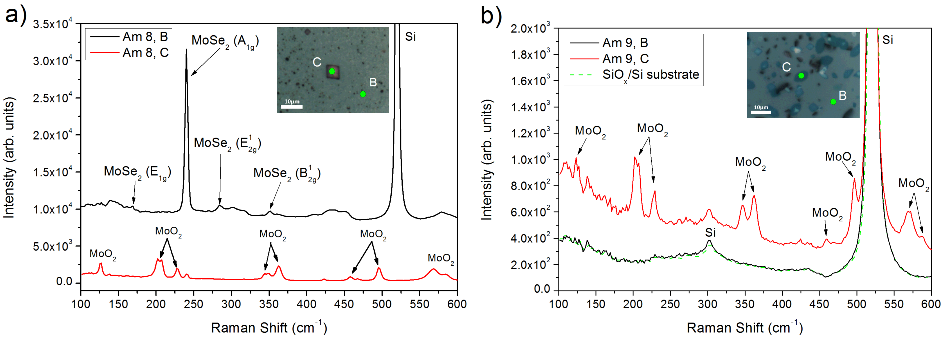

Figure 4.10: **Raman spectra of two different regions in samples 8 and 9.** a) Raman spectra of a crystal plate (C) and of the background (B) of sample 8. b) Raman spectra of sample 9 taken on a blue hexagon crystal and on the sample background. The dash green line is the Raman spectrum of a pristine SiO_x/Si substrate.

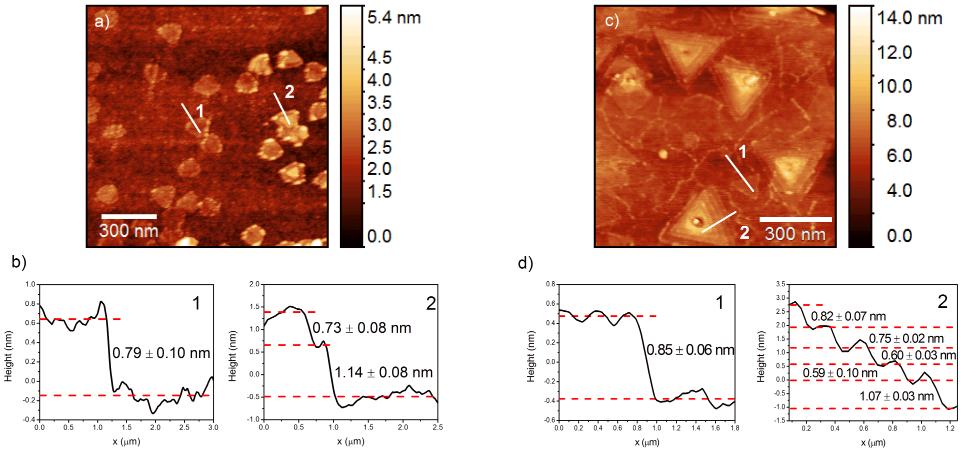

Figure 4.11: **AFM images of samples 7 and 8.** a) AFM image of sample 7. b) Height profiles taken along the white lines 1 and 2 indicated in the AFM image. c) AFM image of sample 8. d) Height profiles taken along the white lines 1 and 2 indicated in the AFM image. The black line is the average height profile and the red dash lines are the average height at each step.

some of them are clearly composed of few-layers. The height profiles seen in Figure 4.11 b) show that the triangle where profile 1 was measured have a height of $0.79 \pm 0.10nm$, corresponding to the reported values of monolayer $MoSe_2$, and that the multilayer triangle of profile 2 is a bilayer, whose top layer has a smaller lateral size. Although there are multilayer $MoSe_2$, Figure 4.11 a) shows a higher density of monolayers, confirming the results obtained by Raman spectroscopy, which showed the A_{1g} and E^1_{2g} modes characteristic of monolayer $MoSe_2$.

Figure 4.11 c) shows the presence of multilayer triangular pyramids on top of sample 8 with lateral sizes $\sim 280nm$, as well as some smaller triangles with $\sim 120nm$ edges. In this figure, it is possible to differentiate the different layers in each pyramid. The height profile measured along line 1, in Figure 4.11 d), shows that the smaller triangles are monolayers with $0.85 \pm 0.06nm$ of height and the height profile measured along line 2 shows that the pyramid is composed of 5 $MoSe_2$ layers, with different heights between 0.59 and 1.07nm. The presence of these multilayer triangular pyramids explain the results obtained by Raman spectroscopy, where the presence of the peak characteristic of B^1_{2g} mode of $MoSe_2$ indicated the presence of multilayer structures.

PL spectroscopy was performed to determine the energy gap of the deposited layers. Figure 4.12 shows the PL spectra for samples 7, 8 and 9, where the peaks at 774, 773 and 772 nm, with respect

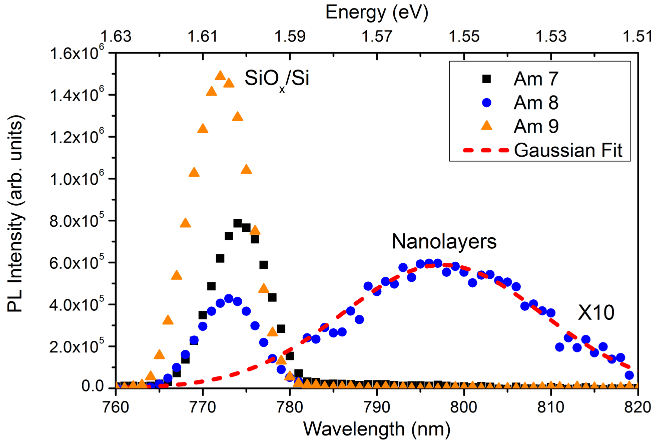

Figure 4.12: **PL spectra of samples 7 - 9.** PL spectra of samples 7, 8 and 9 under $\lambda_{ex} = 514.5nm$. The PL intensity of the peak at 797nm in sample 8 was multiplied by 10. The red dash line corresponds to the Gaussian fit made to that peak.

to each sample, are the contributions from the SiO_x/Si substrates as discussed in section 4.1.2. Notice that since the PL was performed using the spectral lines of a Xenon lamp, with a large spot size, the PL spectrum measured for each sample contains contributions from every crystalline structure present in the samples, resulting in a weak PL signal. Sample 7 does not show a PL peak at $\sim 800nm$, as is reported for monolayer $MoSe_2$. Although it has been shown that this sample has monolayers of $MoSe_2$, the monolayers do not have a regular triangular shape and have reduced lateral sizes indicating their low quality, which might reflect on a very weak non detectable PL signal. On the contrary, sample 8 has a detectable PL peak at 797nm (1.56 eV) with a FWHM of 27nm similar to the FWHM reported [19, 57], indicating that the decrease in H_2 percentage from 16.7% to 8.3% enhanced the PL response, and consequently, the quality of the deposited layers. In the case of sample 9 no PL response was found at $\sim 800nm$, as expected since it does not have $MoSe_2$ deposited on its surface.

This study suggests that a percentage of 8.33% of H_2 in the total gas flow allows the deposition of better quality mono- and multilayer $MoSe_2$, with larger lateral sizes. However, although they are of better quality, more multilayer structures are found in sample 8 than in sample 7. On the contrary, a percentage of 3.33% of H_2 is too low, allowing only the reduction of MoO_3 to MoO_2, therefore promoting the deposition of MoO_2 monoclinic crystals and preventing the deposition of $MoSe_2$. Actually, after the depositions, it was observed an increase in the amount of Mo powder deposited at the bottom of the tube with the increase in H_2 percentage, showing that the highest percentage of H_2 used (16.7%) is probably responsible for the occurrence of an overly reduced MoO_3 powder, preventing the deposition of good quality $MoSe_2$ monolayers.

4.2.3 Quantity of precursors

The supply of precursors is one of the most important deposition parameters since it determines the amount of material available for reaction at the substrate surface, and thus the $Mo : Se$ ratio, which influences the lateral size, shape and quality of the layers produced [17]. If the quantity of selenium present at the substrate surface during the deposition process is not enough, the reduction of MoO_3 into MoO_2 by H_2 will prevail, and so the formation of MoO_2 crystals will be promoted instead of the deposition of $MoSe_2$. This not only leads to the formation of MoO_2 crystal structures, but also to $MoSe_2$ layers with structural defects, like Se vacancies, which greatly decreases the quality of the films produced. Hence, the optimization of the quantity of mass of MoO_3 and Se powders used is crucial to determine which set of MoO_3 and Se powders masses allows the formation of $MoSe_2$ monolayers. Different studies with variations in the powders masses were made in this work. Firstly, the same conditions used for sample 7 and 8 were repeated, but this time with a higher Se powder mass (0.30g), to see if an increase

Table 4.2: **Deposition parameters used in samples 12 and 13.** Resume of the deposition parameters used in samples 12 and 13. Sample 12 and 13 were deposited with 16.67% and 8.33% of H_2 in the total flow, respectively. The other deposition parameters are the ones discussed in the experimental procedure, in section 3.1.1.

Sample	m(MoO_3) (g)	m(Se) (g)	Substrate	T(substrate) (°C)	Flow	%H_2
12	0.20	0.30	160nm SiO_x/Si	790	Ar (50sccm) + H_2 (10sccm)	16.67
13	0.20	0.30	160nm SiO_x/Si	790	Ar (55sccm) + H_2 (5 sccm)	8.33

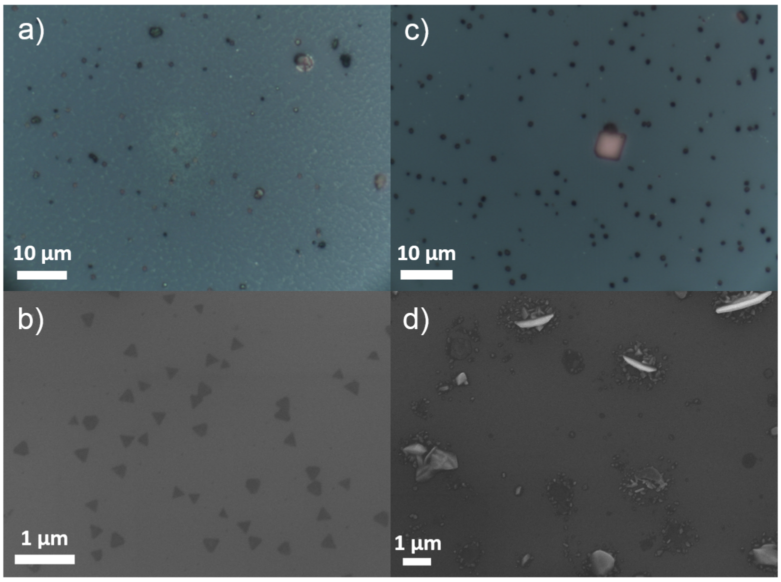

Figure 4.13: **Optical and SEM images of samples 12 and 13.** a) and b) are the optical and SEM images of sample 12, and c) and d) of sample 13, respectively.

in *Se* mass would improve the quality of the layers produced and increase their lateral sizes (samples 12 and 13). After that, using a flow of 55 sccm of *Ar* and 5sccm of H_2, and fixing the selenium mass at 0.31g, the influence of a small decrease in MoO_3 mass was studied (samples 14 and 15). Lastly, for a flow of 50sccm of *Ar* and 10sccm of H_2, a great decrease in MoO_3 mass was studied for 0.30g of *Se* (sample 17), and then fixing 0.60g of *Se*, the layers properties were studied for a decrease in half of the MoO_3 mass (samples 18 and 19).

For the first study, the deposition parameters used in samples 12 and 13 are resumed in Table 4.2. Figure 4.13 shows the optical and SEM images of samples 12 and 13. Sample 12 (Figure 4.13 a)) has a similar surface microstructure as sample 7 (Figure 4.5 e)) but with less and smaller rectangular plates. The SEM image (Figure 4.13 b)) reveals the presence of small triangles (lateral sizes between 150 and 250nm), randomly distributed throughout the sample surface. Some of the triangles are equilateral, and others are truncated triangles with flat vertices. The density of triangles is lower than in sample 7, but they have a more regular shape and larger lateral sizes. In the case of sample 13 (Figure 4.13 c)), its surface is covered with crystals similar to the ones found on sample 8. However, contrary to what was observed for sample 8, the SEM image of sample 13 (Figure 4.13 d)) does not show the presence of

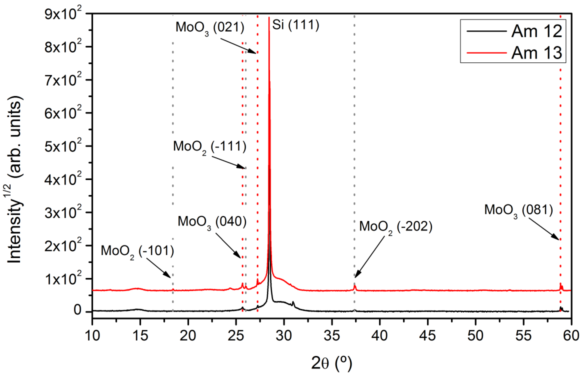

Figure 4.14: **XRD patterns of samples 12 and 13.** X-ray diffraction patterns of samples 12 and 13, where the dashed vertical lines indicate the positions of the indexed peaks of monoclinic MoO_2 and orthorhombic MoO_3.

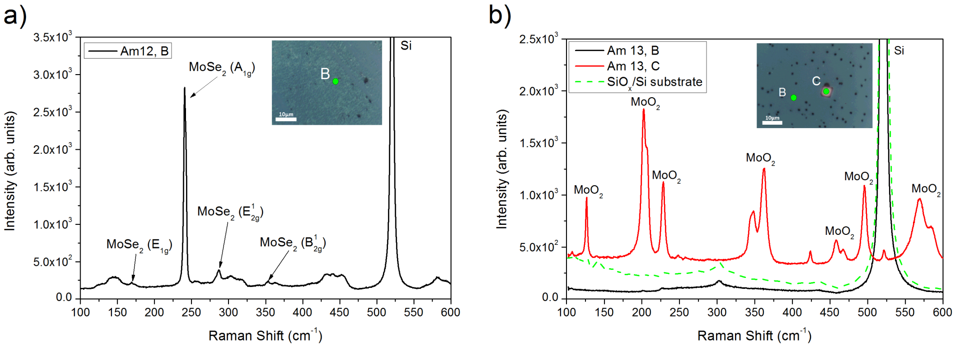

Figure 4.15: **Raman spectra of samples 12 and 13.** a) Raman spectrum of the surface of sample 12. b) Raman spectra of the surface (B) and of a plate crystal (C) of sample 13. Here, the dash green line indicates the Raman spectrum of the pristine SiO_x/Si substrate.

an almost continuous film nor the presence of triangular islands. The XRD patterns of both samples are shown in Figure 4.14 and they have peaks at $2\theta \approx 18.4°$, $26.0°$ and $37.3°$ which are indexed to the planes (-101), (-111) and (-202) of monoclinic MoO_2 (JCPDS 32-0671), respectively, and at $2\theta \approx 25.7°$, $27.3°$ and $58.9°$ indexed to the planes (040), (021) and (081) of orthorhombic MoO_3 (JCPDS 5-0508). The peaks of the XRD pattern of sample 13 have higher intensity then the ones found on the XRD pattern of sample 12, which is due to a higher amount of crystalline material found at the surface of sample 13.

The Raman spectra of samples 12 and 13 are represented in Figure 4.15. The rough background of sample 12 (Figure 4.15 a)) has Raman peaks at 169.0, 240.6, 286.4, and $353.5 cm^{-1}$, corresponding to the E_{1g}, A_{1g}, E^1_{2g} and B^1_{2g} modes of $MoSe_2$, respectively. Although the difference between the E^1_{2g} and A_{1g} modes position is 45.8, close to the one reported for monolayer $MoSe_2$, the presence of the Raman peak characteristic of the B^1_{2g} mode indicates that the triangles found in the SEM image might not be monolayer $MoSe_2$ as in the case of sample 7. In sample 13 (Figure 4.15 b)), the Raman spectrum corresponding to its background is almost identical to the Raman spectrum of the bare SiO_x/Si substrate (dash green line), where the difference in intensity between these two spectra is due to the use of a grating of 600gr/mm in the case of the substrate spectrum and of 1800gr/mm in the case of the sample spectra. This confirms that there is no $MoSe_2$ deposited on the sample surface. The Raman spectrum of one of the plates present on sample 13 only has the Raman peaks characteristic of monoclinic MoO_2. Again, the XRD peaks corresponding to monoclinic MoO_2 are due to these crystal plates, but the crystals corresponding to the MoO_3 XRD peaks were, again, not detected by Raman spectroscopy.

The AFM image of sample 12 can be seen in Figure 4.16 a). It shows triangles with similar lateral sizes as the ones seen in the SEM image. These triangles have higher lateral sizes and a more regular shape than the ones found on sample 7. However, the height profiles shown in Figures 4.16 b) and c),

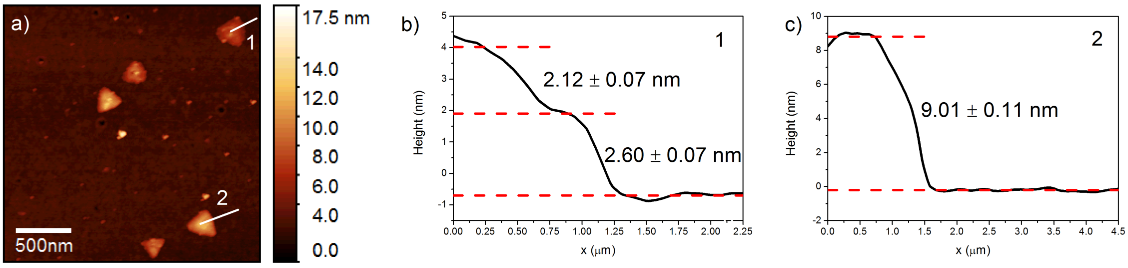

Figure 4.16: **AFM image of sample 12 and respective height profiles.** a) AFM image of the triangles of sample 12. b) and c) are the height profiles taken along the white lines 1 and 2, respectively. The black line is the average height profile and the red dash lines are the average height at each step.

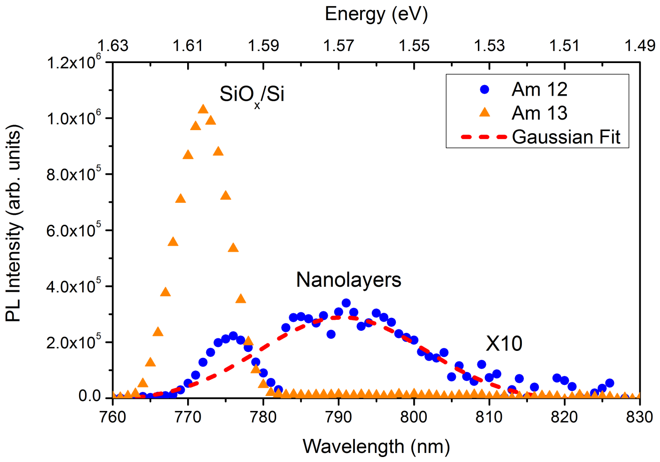

Figure 4.17: **PL spectra of samples 12 and 13.** PL spectra of samples 12 and 13. The PL of sample 12 was multiplied by 10 in the range 782-840nm, in order for the PL peak corresponding to the sample be visible. The red dash line corresponds to the Gaussian fit of that PL peak.

taken along the white lines on Figure 4.16 a), reveal that these triangles are formed by several layers of $MoSe_2$. Profile 1 (Figure 4.16 b)) indicates that the triangle is a pyramid constituted by 3 layers on top of 4 layers of $MoSe_2$, whereas profile 2 taken from a triangle with more color contrast has a height that corresponds to $\sim$ 14 layers of $MoSe_2$. In other images obtained by AFM, no monolayers were found. In the case of sample 13, as expected from the SEM and Raman spectroscopy results, AFM images of its surface (not shown) only showed the roughness of the substrate surface, not detecting any low dimensional structures similar to the ones reported for $MoSe_2$.

The PL spectra of samples 12 and 13 are shown in Figure 4.17. As expected from the previous results, sample 13 only has the PL peak corresponding to the substrate at 772nm. Sample 12, in addiction to the PL peak of the substrate at 776nm, has a low intensity peak at 791nm (1.56 eV) with FWHM of 26nm, which corresponds to the PL response of the $MoSe_2$ few-layer structures found on its surface. Since no $MoSe_2$ monolayer was found in sample 12, its PL intensity is an order of magnitude lower than the PL intensity of sample 8, which, although having pyramids with several layers, also shows monolayers at its surface, which are responsible for a stronger PL signal.

These results were surprising because an improvement of the deposited structures found on sample 7 and 8 were expected. Since selenium has a higher evaporation rate than MoO_3, it evaporates more quickly implying that if the Se mass is too low all of the Se powder used might evaporate before the 15min of deposition has passed. Also, it was observed that the Se powder starts to evaporate during the heating process, making it more likely for all of Se to evaporate before the deposition time is over. In this way, the quantity of Se was increased, in order to guarantee that the supply of selenium was enough. However, not only the triangles found on sample 12 are much thicker than the ones found on sample 7, sample 13 did not present any kind of $MoSe_2$ deposited on its surface.

In the case of samples 7 and 12, all of the other controllable deposition parameters were the same, which suggests that the thicker triangular structures are due to the increase in Se mass. Still, most of the authors that report the deposition of monolayer $MoSe_2$ use higher Se mass than MoO_3 mass [2, 19, 58], which indicates that other parameter is playing an important role on the structures observed. The case of samples 8 and 13 is strange because no $MoSe_2$ was detected in sample 13, although sample 8 seemed to have better quality layers than sample 7. In these two samples, all of the other controllable deposition parameters were the same, except the positioning of the substrate. In the case of sample 8 the substrate length was smaller than the length of the quartz boat so that it was not completely over the boat and

Table 4.3: **Deposition parameters of samples 14 and 15.** Resume of the deposition parameters used in samples 14 and 15. The other deposition parameters are the ones discussed in the experimental procedure, in section 3.1.1.

Sample	m(MoO_3) (g)	m(Se) (g)	Substrate	T(substrate) (°C)	Flow	%H_2
14	0.18	0.31	160nm SiO_x/Si	790	Ar (55sccm) + H_2 (5 sccm)	8.33
15	0.16	0.31	160nm SiO_x/Si	790	Ar (55sccm) + H_2 (5 sccm)	8.33

its height was slightly lower than 1cm. This might influence the thickness of the boundary layer at the substrate surface, which was thicker in the case of sample 13 (higher cross-sectional area, lower average gas flow velocity which implies a thicker boundary layer) implying that the transport of reactants through the boundary layer was more difficult for this sample. However, the difference in height of the substrates between the two samples (consequently in cross-sectional area) was not high enough to cause a great variation in boundary layer thickness that would explain the hindering of the deposition of $MoSe_2$. Since all of the other controllable deposition parameters were the same for these two samples, these results suggest that there are other external parameters that were not identified at the time of the growth experiments and, thus, were not controlled in our experimental setup that greatly influence the deposition of $MoSe_2$ nanofilms. These external parameters can be a difference in the substrate surface roughness that was not carefully studied in this work and is not known, and could have been different for the two substrates used, or fluctuations in temperature or gas flow rate during the deposition process.

In order to confirm that the difference in masses of MoO_3 and Se powders was not responsible for the results obtained for sample 13, two samples were deposited in which the mass of MoO_3 was slightly decreased. Sample 14 was deposited using 0.18g of MoO_3 powder while in sample 15, 0.16g of MoO_3 powder was used. The deposition parameters used in these two samples are resumed in Table 4.3, where all parameters except the $m(MoO_3)$ are equal to the ones used in sample 13.

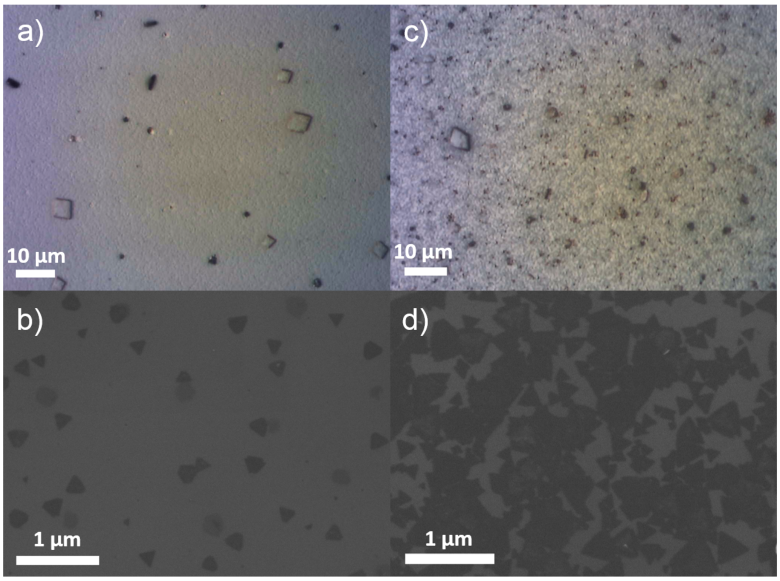

Figure 4.18: **Optical and SEM images of samples 14 and 15.** a) and b) are the optical and SEM images of sample 14, respectively. c) and d) are the optical and SEM images of sample 15, respectively.

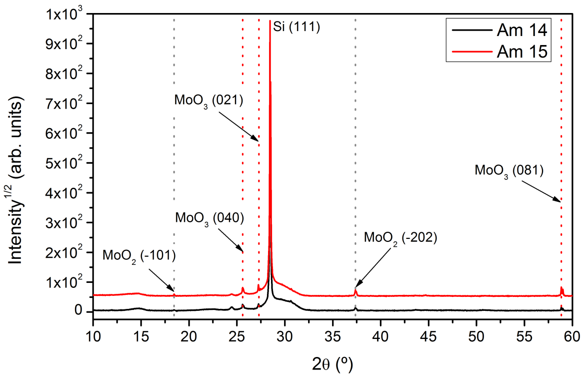

Figure 4.19: **XRD patterns of samples 14 and 15.** X-ray diffraction patterns of samples 14 and 15, where the dashed vertical lines indicate the positions of the indexed peaks of monoclinic MoO_2 and orthorhombic MoO_3.

The optical and SEM images of samples 14 and 15 are shown in Figure 4.18. The optical image of sample 14 (Figure 4.13 a)) is very similar to the optical image of sample 7, with rectangular plates of the same size and with a rough background. The SEM image (Figure 4.18 b)) shows the presence of triangles and truncated triangles of lateral sizes in the range 100-200nm. In the case of sample 15, the optical image (Figure 4.18 c)) shows a different microstructure of the background than the ones previously seen, and also the presence of rectangular plates and small irregular dark crystals. The SEM image of sample 15 (Figure 4.18 d)) reveals the presence of a huge amount of triangles with different lateral sizes, between 150 - 400nm, in which the larger triangles are merged with smaller ones, almost creating a continuous film. The XRD patterns of samples 14 and 15 are shown in Figure 4.19, and both patterns have peaks at the positions $2\theta \approx 18.4°$ and 37.3°, corresponding to the (-101) and (-202) planes of monoclinic MoO_2 (JCPDS 32-0671), respectively, and peaks corresponding to the planes (040), (021) and (081) of orthorhombic MoO_3 at 25.7°, 27.3° and 58.8° (JCPDS 5-0508), respectively.

Figure 4.20 shows the Raman spectra of samples 14 and 15. In the case of sample 14 (Figure 4.20 a)), the Raman spectrum of a crystal on its surface shows that it is a mixture of MoO_2 and $MoSe_2$, as was observed previously for other samples. The Raman peaks at 128.3, 199.9, 204.5, 226.1, 348.4, 358.3, 492.971 and 572.4cm^{-1}, can be attributed to monoclinic MoO_2 and the peaks at 167.3, 240.5 and 282.8 cm^{-1} are close to the values reported for $MoSe_2$. The Raman spectrum of the sample background only shows two peaks beyond the substrate contribution, at the peak positions 242.7 and 287.0cm^{-1}, with low intensity, corresponding to the A_{1g} and E_{2g}^1 modes of $MoSe_2$ indicating the probable presence of few-layer $MoSe_2$, which corresponds to the triangles seen in the SEM image. In sample 15, the Raman spectrum of a plate also has the peaks corresponding to monoclinic MoO_2 at 127.9, 203.6, 208.7, 364.5,

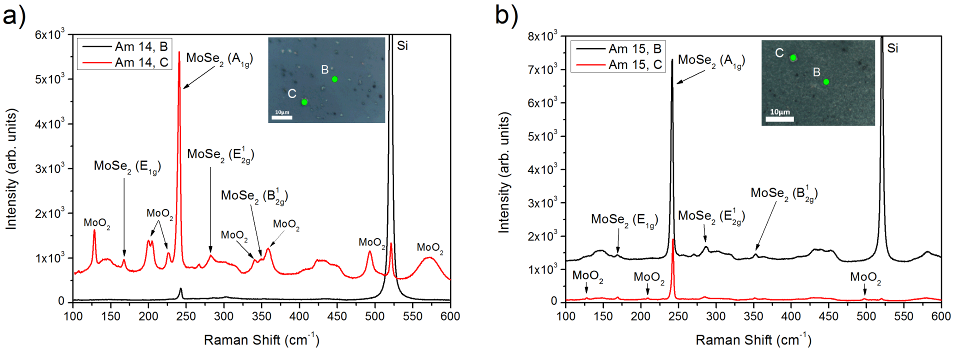

Figure 4.20: **Raman spectra of samples 14 and 15.** a) Raman spectra of the background (B) and of a crystal (C) of a) sample 14 and b) sample 15.

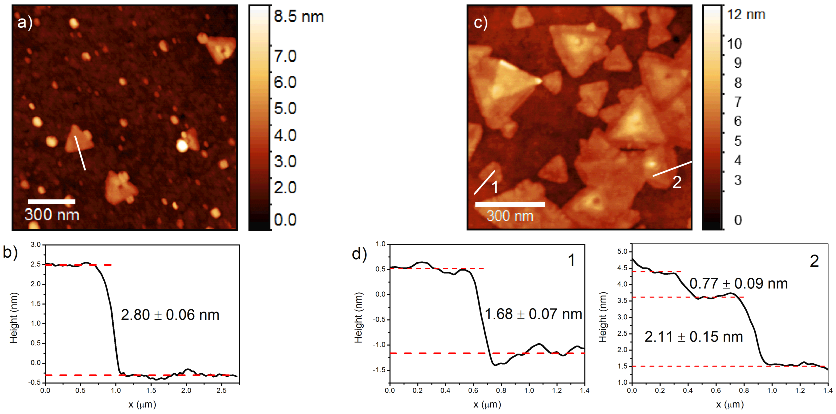

Figure 4.21: **AFM images of samples 14 and 15, and respective height profiles.** a) AFM image of sample 14 and b) the height profile taken along the white line. c) AFM image of sample 15 and d) the height profiles taken along the white lines 1 and 2. The black line is the average height profile and the red dash lines are the average height at each step.

497.5 and 579.3cm^{-1} and the peaks corresponding to $MoSe_2$ at 169.0, 242.2, 284.6 and 351.0 cm^{-1}, all with lower intensity than the peaks observed for the crystal in sample 14. Contrary to the Raman spectrum of the background of sample 14, the background of sample 15 has Raman peaks with high intensity corresponding to the E_{1g}, A_{1g}, E^1_{2g} and B^1_{2g} modes of $MoSe_2$, at the peak positions 168.7, 241.7, 286.0 and 352.3cm^{-1}, respectively. The presence of the B^1_{2g} mode indicates that the triangles seen in the SEM image are made of more than one layer of $MoSe_2$.

To determine the height of the triangles observed in the SEM images, AFM was performed, and the obtained images can be seen in Figure 4.21. In the case of sample 14, Figure 4.21 a) shows the presence of triangles that correspond to the triangles observed in the SEM image. The height profile (Figure 4.21 b)) taken along the white line in Figure 4.21 a), shows that the triangles have a height that corresponds to at least 4 layers, confirming what was said in the analysis of its Raman spectrum. The other triangles observed in Figure 4.21 a) are thicker than the one measured since they present a higher color contrast. Figure 4.21 c) shows the AFM image of sample 15, where distinct layers can be distinguished due to the color contrast. The height profile 1 ((Figure 4.21 d), 1) taken along the white line 1 drawn on the AFM image shows that a small triangle has a height of $1.68 \pm 0.07 nm$ corresponding to two layers of $MoSe_2$. In the case of white line 2 (Figure 4.21 d), 2), a multilayer structure of a monolayer on top of 3 other layers can be found. The triangles and pyramids found in sample 15 have larger lateral sizes and more uniform surfaces than the surfaces of the triangles found in sample 14, which might justify the difference in Raman intensity of the spectra taken from both samples. Another reason for this difference in intensity can be the fact that the merged triangle layers found in sample 15 span a larger area than the randomly distributed triangles of sample 14, resulting in better quality layers and thus higher Raman intensity.

The PL spectra of both samples are shown in Figure 4.22, where sample 14 only has the peak that corresponds to the substrate. On the contrary, sample 15 has a peak at $\sim 797 nm$ (1.56 eV) with a FWHM of 34nm and intensity comparable to the PL peak of sample 8. This confirms that the layers produced in sample 15 are of better quality than the triangles found on sample 14, as already mentioned.

These results indicate that a small decrease in the mass of MoO_3 powder (leaving the Se mass constant) is responsible for the production of better quality layers, that span a larger area over the substrate surface. The decrease in MoO_3 mass in relation to Se mass may promote the reaction between the Se and MoO_{3-x} vapours at the substrate surface because, since selenium has a low chemical reactivity, a great quantity of Se is needed to improve the efficiency of the chemical reaction. In this way, since more selenium is available for reaction at the substrate surface, larger $MoSe_2$ clusters are formed. This study

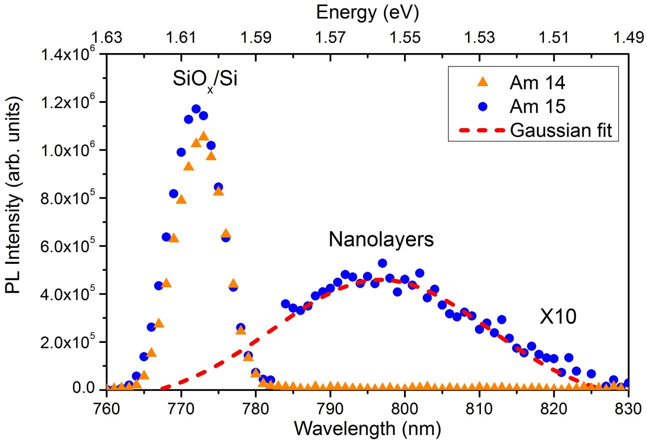

Figure 4.22: **PL spectra of samples 14 and 15.** PL spectra of sample 14 and sample 15. The red dash line indicates the Gaussian fit made to the peak at $\sim 797nm$ in sample 15.

confirms that the fact that in sample 13 no $MoSe_2$ was deposited on its surface was due to an external parameter that could not be controlled in our experimental setup, as discussed previously.

Once no monolayers were found in either of samples 14 and 15, the experimental conditions used in samples 7 and 12 were revisited, with a great change in the precursors masses. In this way, sample 17 was deposited using the same Se mass as sample 12, but with a much smaller MoO_3 mass of 0.08g. Then, in sample 18, the Se mass was doubled to 0.60g, and in sample 19 the MoO_3 mass was halved to 0.04g, fixing $m(Se) = 0.60g$. The deposition parameters of samples 17 to 19 are resumed in Table 4.4. These samples were deposited on SiO_x/Si substrates with an oxide layer 87nm thick.

Table 4.4: **Deposition parameters of samples 17 - 19.** Resume of the deposition parameters used in samples 17, 18 and 19. The other deposition parameters are the ones discussed in the experimental procedure, in subsection 3.1.1.

Sample	m(MoO_3) (g)	m(Se) (g)	Substrate	T(substrate) (°C)	Flow	$\%H_2$
17	0.08	0.30	87nm SiO_x/Si	790	Ar (50sccm) + H_2 (10sccm)	16.67
18	0.08	0.60	87nm SiO_x/Si	790	Ar (50sccm) + H_2 (10sccm)	16.67
19	0.04	0.60	87nm SiO_x/Si	790	Ar (50sccm) + H_2 (10sccm)	16.67

Figure 4.23 showns the optical and SEM images of samples 17 to 19. The optical image of sample 17 (Figure 4.23 a)) shows a smooth surface with black small crystals whose shape is indistinguishable. In the SEM image (Figure 4.23 b)), no triangle isolated islands nor a continuous film are present, only irregular shaped crystals are seen. On the contrary, the optical image of sample 18 (Figure 4.23 c)), shows the presence of large triangles of lateral sizes between 1.3 and 2.3 μm. Surrounding the large triangles, small black crystals, white crystals with an hexagonal shape and small orange spots can be seen. The SEM image taken at the surrounding area (Figure 4.23 d)) shows that the small orange spots seen in the optical image are indeed triangles of lateral sizes in the range $700-800nm$, and it also shows irregular shaped structures with edges $\sim 400nm$. In the case of sample 19, its optical image (Figure 4.23

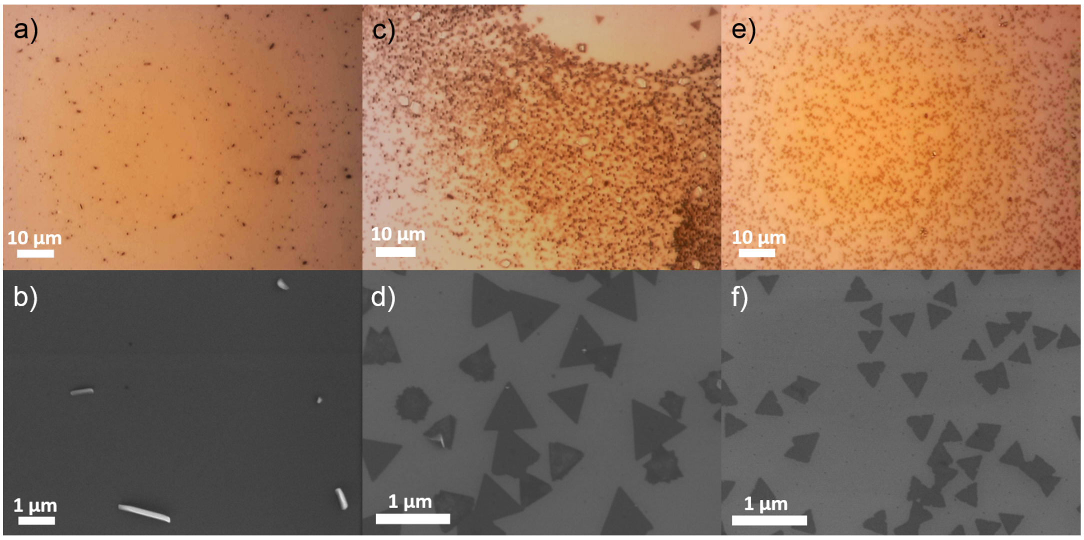

Figure 4.23: **Optical and SEM images of samples 17 to 19.** Optical and SEM images of a), b) sample 17, c), d) sample 18 and e), f) sample 19, respectively.

e)) shows small orange spots similar to the ones present in the optical image of sample 18. However, the SEM image (Figure 4.23 f)) reveals that these orange spots are triangles with lateral sizes $\sim 300nm$, smaller than the triangles present in sample 18. Additionally, the triangles found on sample 19 look like they have degraded edges, where small quantities seem to be missing.

The XRD patterns of the three samples are presented in Figure 4.24. They all have the peaks at $2\theta \approx 25.7^\circ$, 27.3° and 58.9° which are characteristic of orthorhombic MoO_3, as appeared in the previous samples. However, only one peak corresponding to monoclinic MoO_2 is found at 37.3°, with a really low intensity. Only sample 18 has a peak at $2\theta \approx 13.7^\circ$, characteristic of 2H-$MoSe_2$ (JCPDS 29-0914), with an almost undetectable intensity, which might be due to a great density of triangles present on its surface.

The Raman spectra of samples 17, 18 and 19 are shown in Figure 4.25. In the case of sample 17 (Figure 4.25 a)), the Raman spectrum of its background (B) has the same behaviour as the Raman spectrum of the bare SiO_x/Si substrate (dash green line) and the Raman spectrum of a crystal on its surface (C) has the peaks attributed to monoclinic MoO_2 at the peak positions 126.9, 202.1, 205.7, 228.3, 345.1, 360.7, 494.1 and 565.8 cm^{-1}. These results suggest that sample 17 does not have $MoSe_2$ deposited on its surface, just like in the case of sample 13. In sample 18, three different regions were

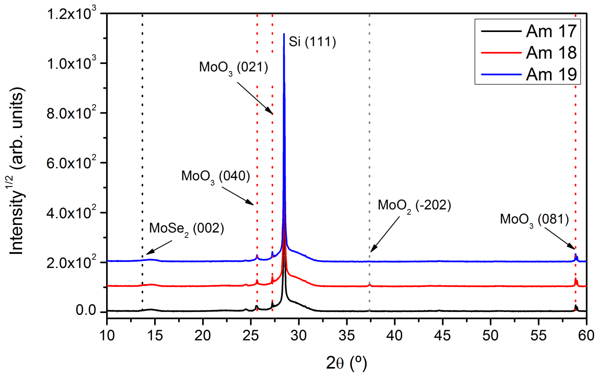

Figure 4.24: **XRD patterns of samples 17 - 19.** XRD patterns of samples 17, 18 and 19. The vertical dash lines indicate the peak positions indexed to $MoSe_2$ (black) MoO_2 and MoO_3.

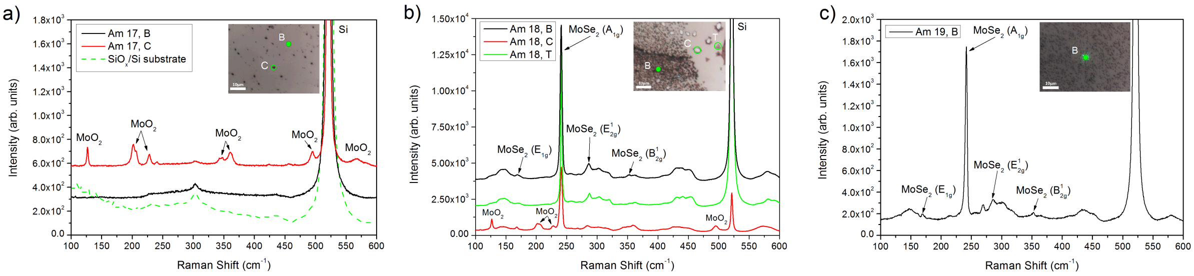

Figure 4.25: **Raman spectra of samples 17 - 19.** a) Raman spectra of a crystal (C) and of the background (B) of sample 17. b) Raman spectra of three different regions in sample 18: an hexagonal crystal (C), a triangle (T) and the background (B). c) Raman spectrum of the surface of sample 19.

analysed (Figure 4.25 b)). The Raman spectrum of an hexagonal shaped crystal (C) has peaks at 126.9, 201.1, 206.0, 228.5, 345.4, 360.3, 494.5, 574.0 and 588.6 cm^{-1}, corresponding to monoclinic MoO_2, and peaks at 168.0, 241.1, 283.9 and 350.1 cm^{-1} attributed to $MoSe_2$. One of the largest triangles has Raman peaks at 124.3, 171.5, 241.1 and 287.6cm^{-1} attributed to the modes of low dimensional $MoSe_2$. The difference between the E^1_{2g} and A_{1g} modes at 287.6 and 241.1cm^{-1} is 46.5, close to the value reported for monolayer $MoSe_2$. This result together with the absence of the B^1_{2g} mode at 353cm^{-1} suggest that these isolated large triangles are monolayers of $MoSe_2$. The Raman spectrum of the surrounding area (B) has peaks at 170.3, 241.1, 286.1 and 352.1 $cm^{-}1$, corresponding to the E_{1g}, A_{1g}, E^1_{2g} and B^1_{2g} modes of $MoSe_2$. The presence of the B^1_{2g} mode suggests the presence of few-layer $MoSe_2$ in this region. Here, the presence of $MoSe_2$ peaks in the Raman spectrum of the hexagonal shaped crystal might be due to the fact that these crystals are surrounded by triangular shapes, with the same optical contrast as the triangles, which suggests that they are also few layer $MoSe_2$. Since the crystals have lateral sizes slightly larger then 1μm, the laser spot might not be completely focused on the centre of the crystal, and so the contribution from the surrounding area is detected. The Raman spectrum of the background of sample 19 (Figure 4.25 c)) shows peaks at 169.0, 241.7, 286.3 and 352.5 cm^{-1}, which are attributed to the E_{1g}, A_{1g}, E^1_{2g} and B^1_{2g} modes of $MoSe_2$, respectively. The presence of the B^1_{2g} mode suggests that the triangles are few-layer $MoSe_2$.

The analysis of sample 17 by AFM confirmed, that besides the irregular shaped crystals seen in the

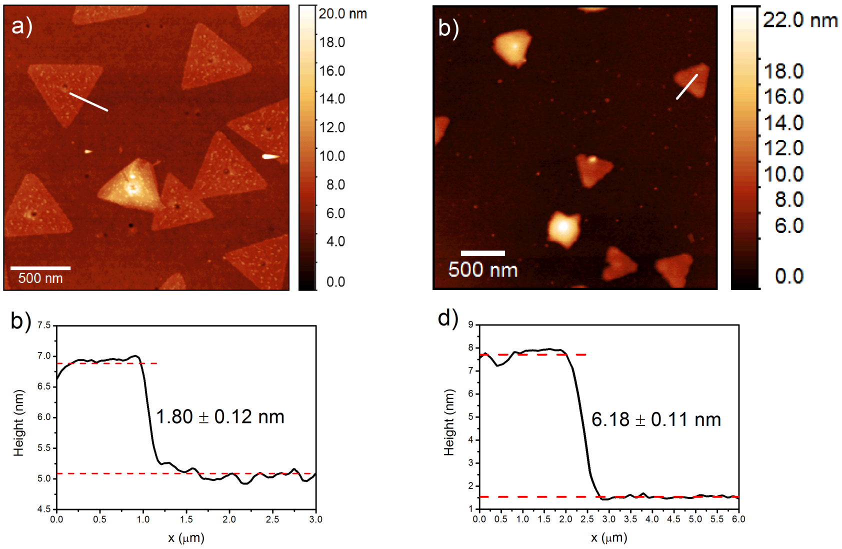

Figure 4.26: **AFM images of samples 18 and 19.** a) AFM image of sample 18 and b) a height profile taken along the white line. c) AFM image of sample 19 and d) a height profile taken along the white line.

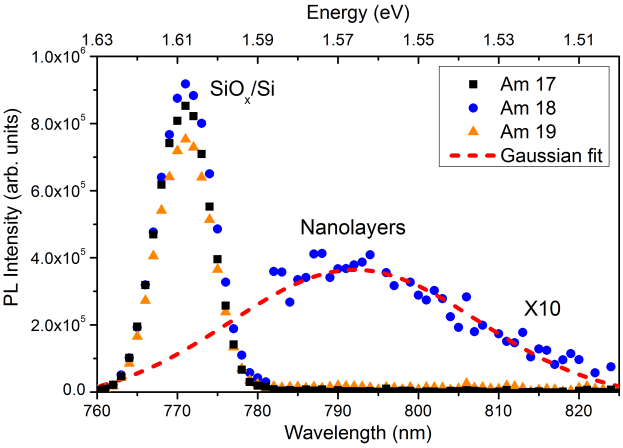

Figure 4.27: **PL spectra of samples 17 - 19.** PL spectra of samples 17, 18 and 19. The red dash line is the Gaussian fit made to the peak at $\sim 792nm$ in the PL spectrum of sample 18.

SEM image, no other shape is present at its surface. The AFM images of samples 18 and 19 are shown in Figure 4.26, with respective height profiles. The AFM image of sample 18 (Figure 4.26 a)) was performed in the same region as the SEM image, and it shows that the triangles have a *hole* in the middle and that their surfaces are not uniform, having small agglomerates deposited on them. The height profile (Figure 4.26 b)) taken along the white line seen in Figure 4.26 a) shows that the triangles have a height of $1.80 \pm 0.12nm$, corresponding to at least 2 layers, which explains the presence of the B^1_{2g} mode in the Raman spectrum taken in this region. The AFM image of sample 19 (Figure 4.26 b)) shows the triangles observed on the SEM image. These triangles are composed of 9 layers, having $6.18 \pm 0.11nm$ of height, as is shown on the height profile in Figure 4.26 d). In this image, it can also be seen that the edges of the triangles are not uniform and that it seems like a piece of the triangle edge is missing.

The PL spectra of samples 17, 18 and 19 are shown in Figure 4.27. Both samples 17 and 19 don't show a PL contribution near 800nm. However, sample 18 has a PL peak at 792nm (1.56 eV) with a FWHM of 31nm and an intensity that is comparable to the intensity of the PL peaks of samples 8 and 15, showing that the triangles of sample 18, although larger than the ones found on these samples, are of similar quality.

Since samples 12 and 18 both have layers of $MoSe_2$ deposited on their surfaces, there is no evidence on the deposition parameters of sample 17 that suggest the failure in depositing $MoSe_2$ on its surface. If the non deposition in this sample was due to a low ratio of $m(MoO_3)/m(Se)$, then sample 18 would have had no nanolayers of $MoSe_2$. This suggests that the reason why sample 17 does not have any $MoSe_2$ deposited is the same as in sample 13, which proves the existence of external factors to our experimental setup that highly influence the deposited film. To undoubtedly prove this, the deposited parameters used in samples 13 and 17 should be repeated.

Sample 18 was the first sample to have triangles with sufficient lateral sizes that made them visible by optical microscopy. The results of this sample show that the growth of larger triangles happens for a low $m(MoO_3)/m(Se)$ ratio, as suspected. An excess of Se molecules in relation to MoO_3 is necessary to promote the growth of $MoSe_2$ nanosheets, because of the low chemical reactivity of selenium. However, the small triangles present in sample 19 show that if this ratio is too low, it will hinder the growth of $MoSe_2$ nanolayers due to a lack of MoO_3 molecules available for reaction. Moreover, the degraded aspect of the edges of these triangles might be an indication of the existence of Mo defects. In this way, the results of sample 18 suggest that the precursor masses used are a good start point to study the

Table 4.5: **Deposition parameters of samples 18 and 20.** Resume of the deposition parameters used in samples 18 and 20. The other deposition parameters are the ones discussed in the experimental procedure, in subsection 3.1.1.

Sample	m(MoO_3) (g)	m(Se) (g)	Substrate	T(substrate) (°C)	Flow	Total Flow
18	0.08	0.60	87nm SiO_x/Si	790	Ar (50sccm) + H_2 (10sccm)	60sccm
20	0.08	0.61	87nm SiO_x/Si	790	Ar (16.7sccm) + H_2 (3.3sccm)	20sccm

influence on the deposited layers of other deposition parameters. Since no monolayers were found on sample 18, the growth of few-layer structures may be promoted due to other deposition parameter as, for example, the total flow rate used.

4.2.4 Total flow rate

In the previous samples, the total flow rate of 60 sccm might have been too high, hindering the lateral growth of the nanolayers produced. A high flow rate implies a low residency time of the reactant molecules at the substrate surface, so that they may not have enough time to move into the right lattice sites, forming layered structures of non-uniform thickness. To understand if a lower gas flow rate would promote the growth of larger layers, sample 20 was performed using a total flow rate of 20 sccm, with the same H_2 partial pressure as sample 18. The deposition conditions of sample 20 are resumed in Table 4.5, together with the deposition parameters of sample 18, to facilitate the comparison.

Figure 4.28 shows the optical and SEM images of sample 20. Its surface is covered by hexagonal crystals similar to the ones found on sample 18 (Figure 4.23 c)). Its background has an orange microstructure which is due to small triangles of lateral sizes between 80 - 220 nm, as revealed by the SEM image (Figure 4.28 b)). These triangles are merged together in a similar way as the triangles found on sample 15. The XRD pattern of sample 20 is shown in Figure 4.28 c), and it has the peaks indexed to the (-101) and (-202) planes of monoclinic MoO_2 at $2\theta \approx 18.4°$ and $37.4°$, respectively. It also presents the diffraction peaks indexed to the (040), (021) and (081) planes of orthorhombic MoO_3 at the peak positions $2\theta \approx 25.7°$, $27.3°$ and $58.9°$.

The Raman spectra of sample 20 are shown in Figure 4.29 b). The crystal (C) has Raman peaks at 125.8, 203.9, 209.0, 229.9, 345.4, 364.1, 495.5, 573.6 and 591.0 cm^{-1}, that can be attributed to mono-

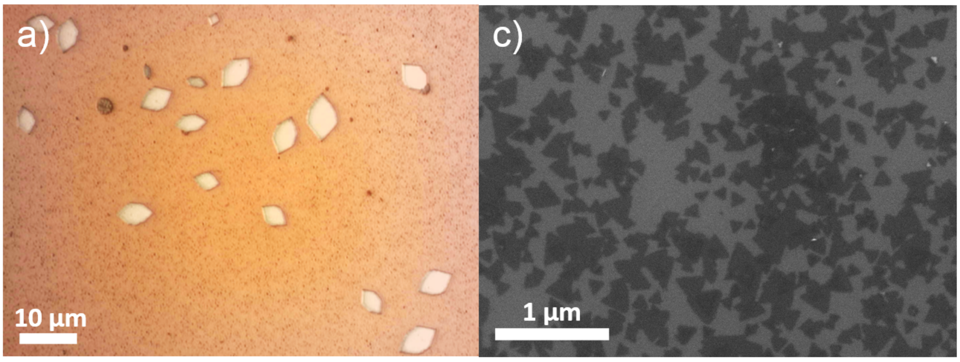

Figure 4.28: **Optical and SEM images of sample 20.** a) Optical and b) SEM images of sample 20.

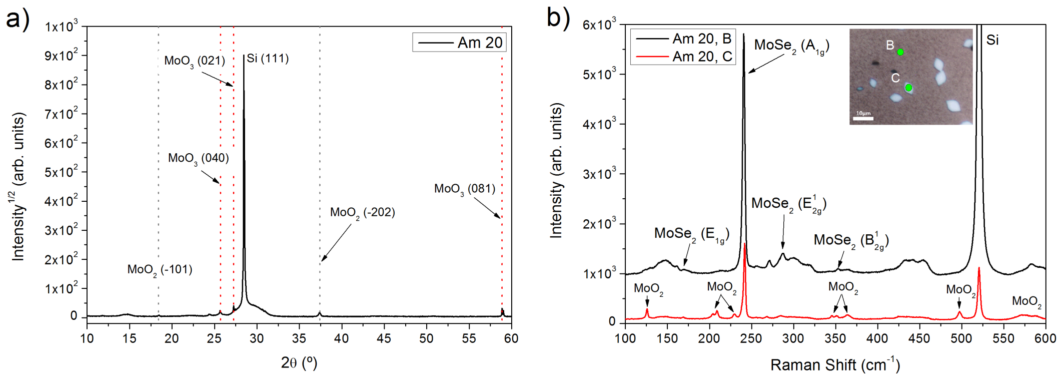

Figure 4.29: **XRD pattern and Raman spectra of sample 20.** a) XRD pattern of sample 20. b) Raman spectra of the background (B) and of a crystal (C) of sample 20.

clinic MoO_2 and peaks at 168.7, 241.7, 284.2 and 351.0cm^{-1}, that correspond to $MoSe_2$. These Raman peaks of $MoSe_2$ might be due to a not centred focused laser beam, which can detect the contribution from the surrounding area of the crystal. In the case of the Raman spectra of the background, the peaks are at the positions 169.5, 240.6, 286.7 and 352.9cm^{-1} corresponding to the E_{1g}, A_{1g}, E^1_{2g} and B^1_{2g} modes of $MoSe_2$, respectively. The presence of the B^1_{2g} mode on the Raman spectrum of the background indicates that the triangular shapes shown in the SEM image are composed of few-layer $MoSe_2$, although the difference between the E^1_{2g} and A_{1g} modes is 46.1cm^{-1}, close to the reported value for monolayer $MoSe_2$. This may suggest a mixture of mono- to few-layer structures.

The AFM image of sample 20, together with two height profiles taken along the white lines shown on the AFM image, are presented in Figure 4.30. The AFM image (Figure 4.30 a)) clearly shows triangles of different lateral sizes, some of them merged together, and the presence of few-layer structures. The height profile taken along white line 1 (Figure 4.30 b)) indicates that the triangles with a more uniform color contrast have a height of $1.53 \pm 0.09nm$, corresponding to bilayer $MoSe_2$. The height profile taken along white line 2 (Figure 4.30 c)), where two distinct triangles can be seen on top of each other, shows a monolayer on top of a bilayer with larger lateral size. This is similar to what was observed in sample 15.

The PL spectrum of sample 20 is shown in Figure 4.31. Additionally to the contribution of the substrate at 771nm, a peak at 792nm (1.56 eV) is present, with a FWHM of 30nm and an intensity an order of magnitude lower than the PL peak intensity of samples 15 and 18. Although sample 20 is very similar to sample 15, the triangular domains of sample 20 have lower lateral sizes, which are responsible for more grain boundaries, known to decrease the PL.

These results show that a total flow rate of 20sccm does not promote the lateral growth of the $MoSe_2$

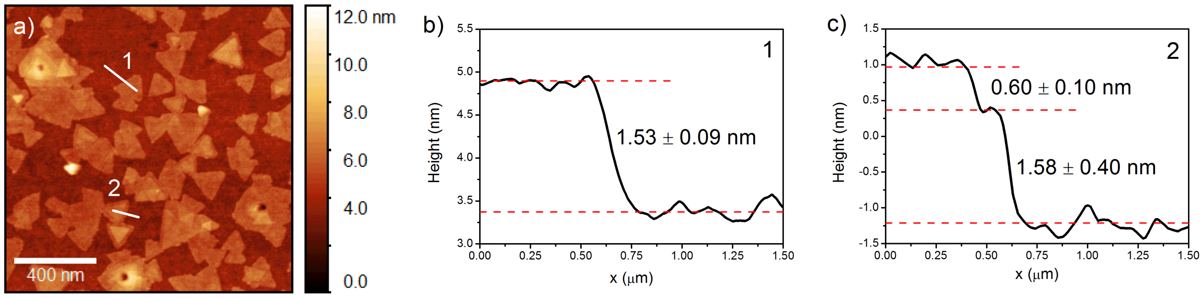

Figure 4.30: **AFM image of sample 20.** a) AFM image of sample 20. b) and c) are the height profiles taken along the white lines 1 and 2, respectively, shown in a).

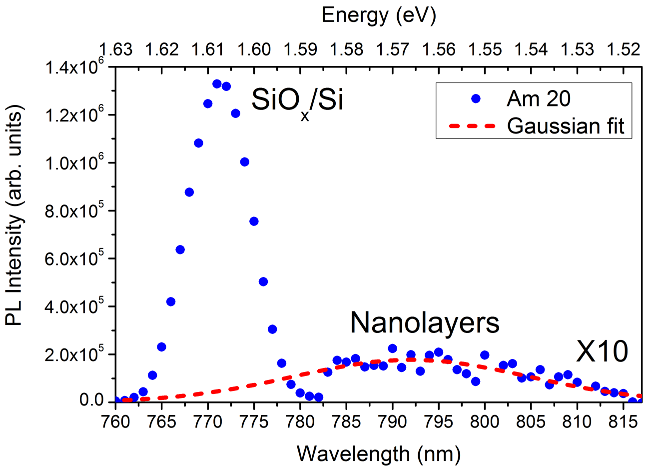

Figure 4.31: **PL spectrum of sample 20.** PL spectrum of sample 20, where the dash red line indicates the Gaussian fit of the PL peak of the sample, which was multiplied by 10.

nanolayers. Instead of large triangular clusters of uniform thickness, sample 20 has small bilayer clusters that are merged together laterally, and few layers deposited on top of each other, similar to what was observed in sample 15. A low flow rate drags lower quantities of Se atoms from its source to the substrate region, implying that at the substrate surface the ratio $MoO_{3-x}:Se$ will be higher for a flow of 20sccm than for 60sccm, for fixed precursor's masses. Since the morphology of the layers deposited on sample 20 is similar to the ones on sample 15, the ratio $MoO_{3-x}:Se$ in sample 20 may be close to the ratio that was present in sample 15 (that was caused by a lower Se powder mass). This suggests that a decrease in flow rate, from 60 to 20 sccm, may have a similar effect on the morphology of the deposited layers as the use of a smaller difference between the masses of the precursors. Moreover, a lower gas flow rate is responsible for a thicker boundary layer, which renders the diffusion of the reactant molecules through the boundary layer to the substrate surface less efficient. Consequently, the mass transport becomes the growth rate limiting factor, instead of the surface reaction that occurs at a faster rate. This is known to yield a columnar type of growth in conventional CVD of thin films. Here, because the deposition times are very short, the growth is limited in height and few-layer triangles are observed, representing primary nucleation sites, as well as small bilayers formed due to secondary nucleation. This might be the reason why sample 20 has smaller triangle domains than sample 15.

4.2.5 Distance from the MoO_3 powder

In the previous experiments, all analysis were made at the centre of the samples, where the distance between the substrate and the MoO_3 precursor was $\sim 3cm$. However, for every sample, it was observed that the substrate surface area covered by deposited material decreased with the distance from the MoO_3 powder, accompanied with a change in lateral size or morphology of the deposited nanolayers. This can be seen in Figure 5.1 of Appendix A, where a change in shape of the nanolayers deposited in sample 18 and a transition from a continuous film to isolated islands in sample 20 are observed along the gas flow direction. It has been reported that this variation in shape and lateral size is caused by a sharp precursor concentration gradient that forms along the gas flow direction at the substrate surface [17], as discussed in subsection 2.2.2.

To study the variation in morphology of the samples as a function of the distance from the MoO_3 powder, a deposition with four substrates over a quartz boat was performed. A 6cm quartz boat was used, where the MoO_3 powder was put 0.5cm away from the upstream edge of the boat and the first substrate was centred 2cm away from that edge. The other three substrates were tightly placed side by side at the downstream side. All substrates had a width of $\sim 1cm$ and together all of them covered a length of $\sim 4cm$. The substrates used were 87nm SiO_x/Si, and the deposition conditions were the same as in sample 12, but with 0.14g of MoO_3 powder. This experiment was performed between samples 15 and 17, and the substrates were placed in a way such that the third substrate was at the same position as the substrates in the previous experiments.

The substrates are designated A, B, C and D, being A the one nearer the MoO_3 powder and D the one farthest from it. After the deposition, each sample had a different pattern of deposition which showed the presence of a MoO_3 concentration gradient. The morphology of the deposited films in samples A to D, at different regions along the gas flow direction, is shown in the SEM images in Figure 4.32. In sample A, Figure 4.32 a1) shows the presence of sphere like aggregates of nanoplates, that almost completely cover the substrate surface near the MoO_3 source. The SEM image suggests a growth in height, which might be due to a great concentration of MoO_3 molecules at that region. EDS studies reveal the presence of Mo, Se and oxygen atoms, with a higher atomic weight of oxygen, suggesting the deposition of molybdenum oxides with incorporated Se. As one moves away from the MoO_3 source to the regions shown in Figures 4.32 a2) and a3), the morphology progressively changes to a shape that looks like aggregates of nanofibres, that cover less surface area as before. EDS results show the presence of silicon atoms additionally to Mo, Se and oxygen, suggesting that these aggregates are thinner than the previous ones. Moving further away from the MoO_3 powder, Figure 4.32 a4), the shape of the aggregates changes to nanosheets oriented in different directions, that join to form rectangular aggregates, and less surface area is covered. Finally, at the farthest edge, at a distance of about 1.5cm from the MoO_3 precursor (Figure 4.32 a5)), small clusters of nanosheets spread along the substrate surface. The EDS of the nanosheets in the previous two regions shows the presence of Mo, Se, Si and O atoms. The region between the aggregates, clusters and nanosheets in the five different regions is covered by a continuous thin film of unknown thickness, because the EDS shows the presence of Se atoms in those regions, additionally to the presence of silicon and oxygen atoms.

In sample B, the SEM image of the region closer to sample A (Figure 4.32 b1)) shows the presence of rectangular plates whose surfaces are covered with nanosheets. EDS results reveals the presence of Mo, Se, Si and O atoms, with a high atomic weight of silicon, suggesting that they are thin. Moving along the gas flow direction to Figure 4.32 b2), the rectangle plates turn to smaller ones that are farther apart from each other and the substrate surface becomes covered with randomly distributed oriented nanosheets. The rectangle plates and the nanosheets are surrounded by a continuous thin film, as in the case of sample A. Further from the MoO_3 powder, the amount of nanosheets decreases and the thin film can be seen as being composed of triangular domains, as in the inset of Figure 4.32 b3). At some point, the continuous thin film changes to isolated triangular islands randomly distributed at the substrate surface, as can be seen in Figure 4.32 b4), where triangles and truncated triangles of different lateral sizes can be observed (between 110 - 300nm). With the increase in the distance from the MoO_3 precursor, Figure 4.32 b5), the number of triangles decreases and their lateral sizes become smaller (between 50 - 130nm). The transition from a continuous film to isolated triangle islands, whose shape and size varies along the gas flow direction, indicates the presence of a precursor concentration gradient.

In the case of sample C, the region near sample B has rectangle plates of lateral sizes of $\sim 1.4\mu m$ (Figures 4.32 c1)), whose surfaces are smooth. EDS made at the centre of a plate shows the presence of Mo, silicon and oxygen atoms, indicating that these are molybdenum oxide plates. Moving further away from the MoO_3 powder to Figure 4.32 c2), one observes the appearance of triangles and truncated triangles of lateral sizes $\sim 120nm$, that stay with similar lateral sizes and shapes along the gas flow

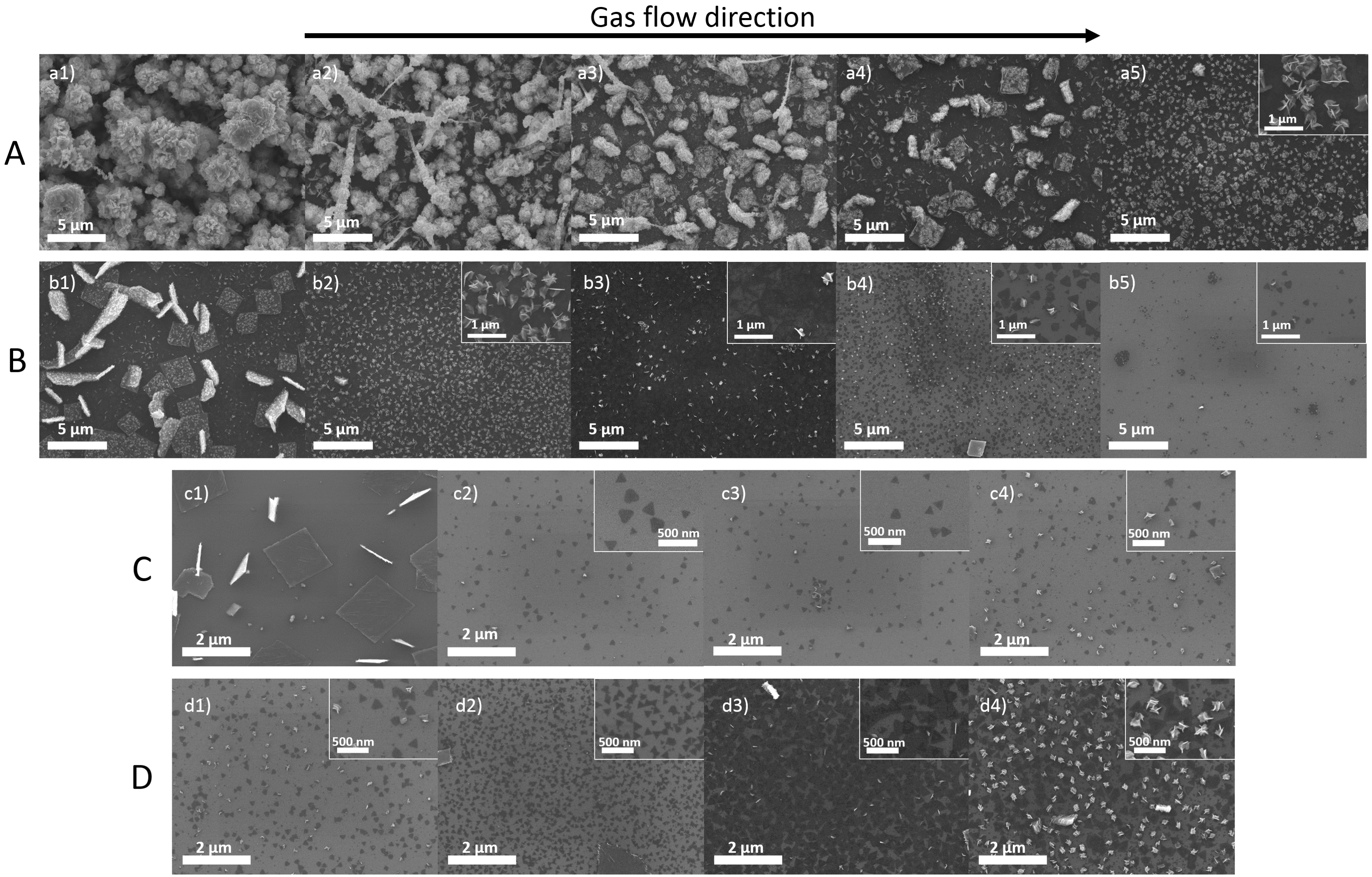

Figure 4.32: **SEM images of samples A to D.** SEM images of samples A, B, C and D, showing the change in morphology along the gas flow direction, represented by the black arrow.

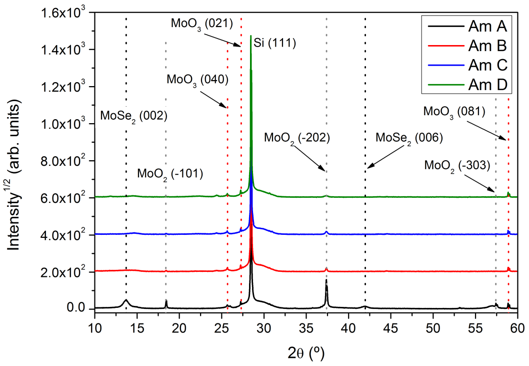

Figure 4.33: **XRD patterns of samples A - D.** The vertical dotted lines indicate the indexed peaks of 2H-$MoSe_2$, monoclinic MoO_2 and orthorhombic MoO_3.

direction (Figures 4.32 c3) and c4)). In sample D, the region near sample C has triangles of lateral sizes $\sim 130nm$ (Figure 4.32 d1)) that are randomly distributed along the substrate surface, very similar to the ones found earlier in Figure 4.32 c4). Moving along the gas flow direction to Figure 4.32 d2), the lateral sizes of the triangles decreases to $\sim 90nm$, but a lot more of them are observed. Increasing the distance to the MoO_3 powder, the lateral size of the triangles increases to $\sim 240nm$ (Figure 4.32 d3)) and they merge together almost transforming into a continuous film, contrary to what was observed in the previous samples. Finally, at the farthest point from the MoO_3 precursor, the number of triangles decreases, transforming into almost isolated islands, and nanosheets randomly oriented reappear.

The XRD patterns of samples A to D are shown in Figure 4.33. In the XRD pattern of sample A, the diffraction peaks at about $2\theta \approx 13.7°$ and $41.9°$ are indexed to the (002) and (006) planes of 2H-$MoSe_2$ (JCPDS 29-0914), the ones at $2\theta \approx 18.4°$, $37.4°$ and $57.4°$ are indexed to the (-101), (-202) and (-303) planes of monoclinic MoO_2 (JCPDS 32-0671) and the peaks at $2\theta \approx 25.7°$, $27.3°$ and $58.9°$ are indexed to the (040), (021) and (081) planes of orthorhombic MoO_3 (JCPDS 5-0508). This results suggest that there are residual MoO_3 on sample A, which might be due to non-reacted MoO_3 vapour that deposited on the sample surface during the heating or cooling of the furnace. The high intensity diffraction peak at $37.4°$ shows that a high quantity of crystalline monoclinic MoO_2 was deposited on the sample surface, and the broad $MoSe_2$ diffraction peaks show that the $MoSe_2$ deposited is nanocrystalline. Samples B to D have the peaks corresponding to monoclinic MoO_2 and orthorhombic MoO_3 at the same peak positions as sample A, but with lower peak intensities, indicating that the molybdenum oxides present are in lower quantity. However, the diffraction peaks indexed to $MoSe_2$ are absent, indicating that the $MoSe_2$ present is in the form of low dimensional materials, such as the nanosheets and the few-layer triangle islands.

The Raman spectra of samples A to D are represented in Figures 4.34 a) and b), for five different regions along the gas flow direction, where the first and last Raman spectrum of each sample corresponds

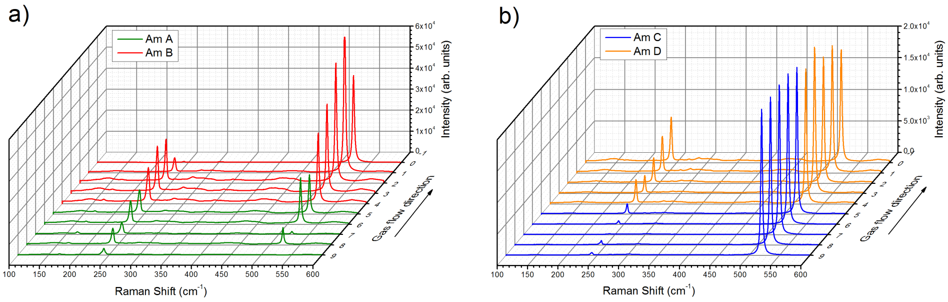

Figure 4.34: **Raman spectra of samples A - D.** Raman spectra of five positions in a) samples A, B and b) samples C, D.

to the upstream and downstream edges, respectively. In the case of sample A, because a great quantity of material is deposited on its surface, the characteristic Raman peak of silicon at 521.6 cm^{-1} has a low intensity or is absent. All of the five Raman spectra have the peaks characteristic of the modes E_{1g}, A_{1g} and E_{2g}^1 of $MoSe_2$, but no peak corresponding to the B_{2g}^1 mode at $\sim 353cm^{-1}$ is observed. Since this mode is absent in bulk $MoSe_2$, these results indicate the presence of bulk $MoSe_2$ and confirm the results by XRD. The A_{1g} mode shifts from $241.4cm^{-1}$ at the edge nearer the MoO_3 powder to 241.7 cm^{-1} in the centre of the sample and finally to $242.2cm^{-1}$ at the downstream edge near sample B. Although these values are similar to the ones reported for few-layer $MoSe_2$, the value of the E_{2g}^1 mode is $\sim$ 284.1, which is similar to the value reported for bulk $MoSe_2$ [59].

For sample B, the intensity of the silicon Raman peak at 521.6 cm^{-1} increases along the gas flow direction indicating a decrease in the film thickness. The Raman spectrum made at the downstream edge of the sample, where almost no film was observed by the SEM image in Figure 4.32 b4), has a lower silicon Raman peak intensity, but since the peaks characteristic of $Mose_2$ are almost undetectable, this decrease could be due to an external factor not taken into account. All of the Raman spectra of sample B have the Raman peaks of $MoSe_2$, characteristic of the E_{1g}, A_{1g}, E_{2g}^1 and B_{2g}^1 modes. The A_{1g} mode remains at $242.2cm^{-1}$ for the first three Raman spectra, and then decreases to $241.7cm^{-1}$ in the fourth spectrum, returning to $242.2cm^{-1}$ in the last Raman spectrum. The E_{2g}^1 mode shifts from $284.3cm^{-1}$ in the first spectrum, to $284.9cm^{-1}$ in the second spectrum, to $285.8cm^{-1}$ in the third and fourth spectra, and finally to $287.1cm^{-1}$ in the fifth spectrum. The B_{2g}^1 starts at $351.3cm^{-1}$ for the first two spectra, but then shifts to $352.0cm^{-1}$. These values of the $MoSe_2$ Raman modes show the transition between bulk $MoSe_2$, at the regions near the MoO_3 powder, to low dimensional $MoSe_2$ as one goes along the gas flow direction.

In sample C (Figure 4.34 c)) , the first four Raman spectra only have the Raman peaks characteristic of silicon at $520.6cm^{-1}$, and of the A_{1g} mode of $MoSe_2$ at 241.1, 242.2, 241.2 and $241.7cm^{-1}$, respectively. The non-detection of the other Raman modes of $MoSe_2$ can be due to the reduced lateral size of the triangular islands and to the spacing between adjacent islands. Because the laser spot is $\sim 1\mu m^2$ and the spacing between the triangular islands is in the range 0.5 - 1.0 μm, the laser will detect a small effective area covered in $MoSe_2$, resulting in a low signal. The reduced size of the triangles also shows their low

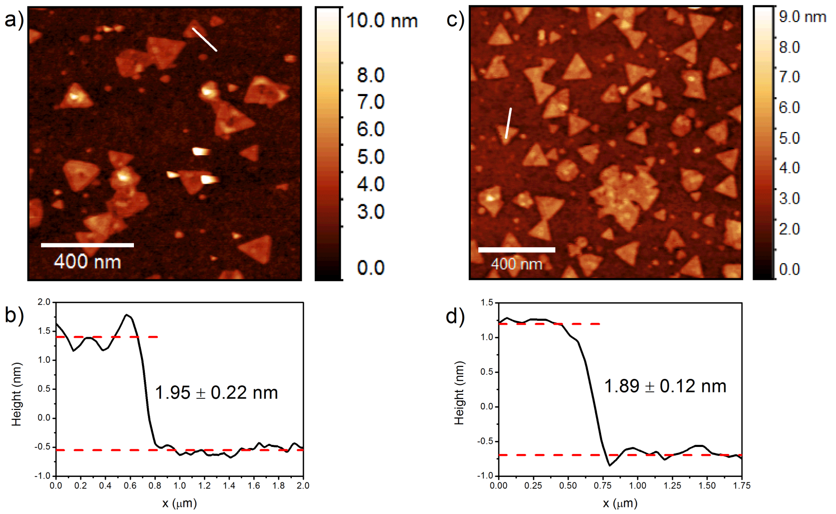

Figure 4.35: **AFM images of samples C and D.** a) AFM image of sample C and b) is the height profile taken along the white line shown in the AFM image. c) AFM image of sample D and d) is the height profile taken along the white line shown in the AFM image.

quality, which affects the Raman peak intensity. However, the Raman spectra made at the downstream edge of sample C shows Raman peaks at 241.1, 286.4 and 352.6cm^{-1}, corresponding to the A_{1g}, E^1_{2g} and B^1_{2g} modes of $MoSe_2$, suggesting the presence of few-layer $MoSe_2$.

Finally, sample D has Raman peaks more well defined, and for the five Raman spectra the Raman modes of low dimensional $MoSe_2$ are present. In the first four Raman spectra, the modes A_{1g}, E^1_{2g} and B^1_{2g} are at 241.1, 287.6 and 353.0cm^{-1}, suggesting the presence of mono- to few-layer $MoSe_2$. The last Raman spectrum, made at the farthest edge from the MoO_3 powder, has Raman peaks at 241.1, 286.0 and 353.0cm^{-1}. The shift of the E^1_{2g} mode to lower values might be due to the presence of the oriented nanosheets seen in the SEM image in Figure 4.32 d4).

Figure 4.35 shows the AFM images of samples C and D. The AFM image of sample C, Figure 4.35 a), shows the presence of triangles and truncated triangles with different heights. The height profile shown in Figure 4.35 b), taken along the white line drawn in the AFM image, reveals that the triangles with a more uniform color contrast have a height of $1.95 \pm 0.22nm$, corresponding to trilayer $MoSe_2$. In the case of sample D, the AFM image corresponds to the triangles seen in the SEM image in Figure 4.32 d2), and the height profile taken along the white line drawn on it shows that these triangles have a height of $1.89 \pm 0.12nm$, close to the value of trilayer $MoSe_2$.

The PL spectra of samples A to D are shown in Figure 4.36. Sample A shows a low intensity peak at 774nm which corresponds to the PL signal that comes from the substrate. Its low intensity is due to the great quantity of material that is deposited on its surface. No PL peak is found at about 800nm, because the $Mose_2$ found on this sample is in its bulk form. The PL spectra of sample B has a PL peak at 796nm, additionally to the one at 772nm. This PL peak has a FWHM of 34nm, and a PL intensity higher than the PL intensities found on samples 8, 15 and 18. This high PL is due to the great density of triangle domains, but it can also be due to the large amount of nanosheets on its surface, that have been reported to have a strong PL signal [77]. However, sample C does not present a PL peak near 800nm, possibly due to the same reason as discussed in their Raman spectrum. Here the spot of the excitation source is higher than in the case of the Raman analysis, and so the contribution from the substrate overlays the small PL signal that may come from the reduced size triangles. This also shows that the layers deposited in this sample are of reduced quality. Nevertheless, the PL spectrum of sample D shows a PL peak at 793nm, with a FWHM of 33nm, and PL intensity comparable with the PL intensities of samples 8, 15 and 18.

The reported results of the change in morphology in samples A, B and C confirms what was mentioned earlier and clearly show the presence of a concentration gradient of MoO_3 molecules along the

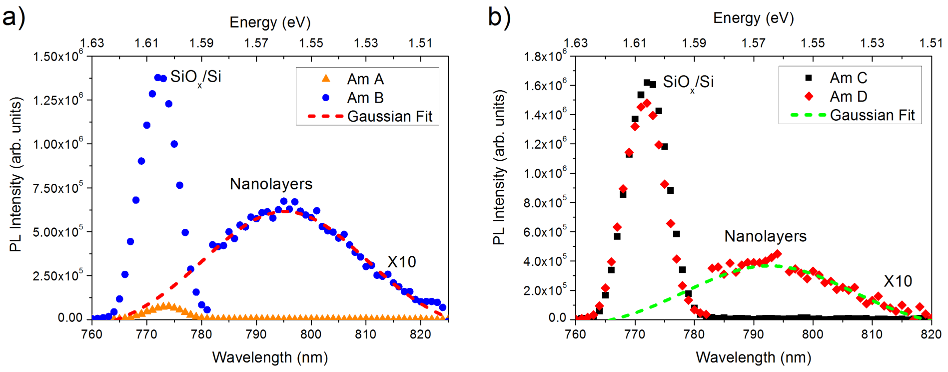

Figure 4.36: **PL spectra of samples A - D.** PL spectra of a) samples A, B and b) samples C, D. The dashed lines are the Gaussian fits of the PL peaks of samples B and D.

downstream direction. Because the MoO_3 powder is very close to sample A, as the MoO_3 molecules evaporate they are rapidly adsorbed by the substrate surface, due to a thin boundary layer at that region. Consequently, at the region nearer the precursor source, the amount of material deposited is very large, forming large aggregates of crystalline material. As the molecules are being deposited, the quantity available for reaction decreases along the gas flow direction, and the deposited material changes from large crystalline aggregates to randomly distributed nanosheets. This clearly shows that a sharp MoO_3 concentration gradient existed along the width of sample A. Moving to sample B, large rectangle plates appear at the region near sample A that, again, change to nanosheets as one moves away from the MoO_3 powder. These large plates indicate an increase in the concentration of MoO_3, which then decreases to a similar concentration as the one found on the downstream edge of sample A. This increase in concentration might be due to the fact that the positioning of the substrates is not perfect so that a small gap exists between them, and the gas that tries to escape through there is held back at the substrate surface near it, increasing the concentration of precursors at that region. Furthermore, the gap disturbs the boundary layer, which becomes thinner at that region, enabling the deposition of more material. As one moves away from the gap, the continuous film that surrounds the plates and the nanosheets turns to isolated triangular islands, whose number and lateral size decreases along the gas flow direction, probably caused by a decrease in the ratio $Mo:Se$. Once more, this is an evidence of the presence of a decrease in MoO_3 concentration along the substrate width. In sample C, the region near sample B has large rectangle plates, indicating an increase in MoO_3 concentration that was probably due to the same phenomena as explained before. Ongoing along the gas flow direction, isolated triangles appear, and they stay with very similar lateral sizes as one moves away from the MoO_3 powder, although some oriented nanosheets reappear at the region farthest from the precursor source. This suggests that at a certain distance from the MoO_3 source, the concentration of MoO_3 molecules becomes more uniform.

However, sample D has a behaviour which is contrary to what is observed in the other three samples and the increase in the nucleation rate with the distance from the MoO_3 powder cannot be explained only by the precursor concentration gradient. Due to the temperature profile of the furnace, the temperature of the four substrates decreases along the gas flow direction (from 799 °C at the centre of sample A to 785 °C at the centre of sample D), and this change has to be taken into account. A decrease in temperature from the equilibrium temperature ($\Delta T = T_e - T$, with T_e the equilibrium temperature and T the growth temperature) is known to increase the nucleation rate (thermodynamic contribution). On the other hand, the molecules have lower thermal energy to diffuse to already existing nucleation sites (transport contribution) which decreases the growth rate [39]. This might explain the increase in the number of triangle islands from Figure 4.32 d1) to d2), accompanied by a decrease in lateral size. Nonetheless, the increase in the triangles lateral size from Figure 4.32 d2) to d3) might be due to a change in the $Mo:Se$ ratio.

Although sample C was put at the same position as the substrates in samples 7 to 20, the deposited $MoSe_2$ layers did not show the same shape change as was observed for the previous samples. In the case of samples 7 - 20, since only one substrate was used, the precursor concentration gradient began to form at the upstream edge of the substrate and prevailed along the substrate width. However, in sample C, because two extra substrates were placed between it and the MoO_3 powder, the precursor concentration gradient began at the upstream edge of sample A, 2cm away from the upstream edge of sample C. When the reactant molecules arrive to sample C, the precursor concentration gradient is already well established and is considerably different than the concentration gradient present in samples 7 -20. Thus, the deposited few-layers will have different characteristics between sample C and samples 7 - 20.

To understand which substrate position, and therefore which substrate temperature and distance from the MoO_3 powder, is more adequate for the deposition of large-area monolayer $MoSe_2$, several studies with the position of the substrate have to be made. Also, to decrease the influence of the MoO_3 concentration gradient, the design of a substrate holder that could tilt the substrate in relation to the gas flow direction could be of great importance, to minimise the variation in the boundary layer thickness.

Chapter 5

Conclusion and future work

In the present work, mono- to few-layer $MoSe_2$ was successfully synthesised by CVD onto SiO_x/Si substrates, using MoO_3 and Se powders as solid precursors. The gas flow consisted of a mixture of Ar and H_2, which acted as the carrier gas and the reducing agent, respectively. Although the deposition of large-area monolayer crystals of $MoSe_2$ was not achieved, the experiments performed enable a clarification over the influence of several deposition parameters on the characteristics of the nanolayers produced. The results show that the morphology of the samples strongly depends on the H_2 partial pressure in the gas phase, concentration gradient of MoO_3 along the substrate surface, mass of the Se powder, and total gas flow rate.

The positioning of the substrate was demonstrated to be an important factor because it influences both the boundary layer thickness and the concentration gradient of MoO_3 molecules, along the substrate surface. It was proven that a lower A_t allowed the deposition of mono- to few-layer $MoSe_2$ in sample 7, contrary to what was observed for sample 6, probably due to a thinner boundary layer. Moreover, a certain distance between the substrate and the MoO_3 source decreased the concentration of MoO_3 molecules at the substrate surface, which enabled the deposition of low dimensional structures, instead of microscopic $MoSe_2$ crystals, as in sample 5. The fact that no triangles were observed on sample 5, contrary to what is reported in the literature for this substrate position, shows that the reproducibility of results in different CVD reactors is difficult, because it strongly depends on the type of reactor, its temperature profile and heating conditions.

The variation of the H_2 partial pressure in the gas phase showed that if it is too low, only the growth of MoO_2 crystals onto the substrate surface is promoted (sample 9). On the other hand, if it is too high, it may reduce the MoO_3 to Mo, which is stable at the growth temperature, preventing the formation of $MoSe_2$. However, while it was demonstrated that a percentage of H_2 lower than 3.33% was insufficient to produce $MoSe_2$ nanolayers, it was not possible to determine which percentage between 8.33% and 16.67% was adequate for the deposition of better quality layers. Although sample 8 has higher PL signal than samples 7 and 12 suggesting its better quality, samples 14 and 15 show poorer results than sample 18. One of the missing pieces is sample 13, where no $MoSe_2$ was deposited on its surface possibly due to external parameters.

The use of a greater mass of Se powder than MoO_3 powder was responsible for the deposition of larger triangular flakes in sample 18, visible by optical microscopy. As discussed, it is a consequence of the low chemical reactivity of selenium, which requires a great amount of Se for the reaction with the MoO_3 molecules to be successful. However, if the difference between the mass of the two precursors is too great, the deposited layers may have vacancies of molybdenum atoms, as is suspected to be the case of sample 19, lowering the quality of their properties.

For every sample, the substrate area covered by $MoSe_2$ was observed to decrease along the gas flow direction, accompanied by a change in the lateral size or in the morphology of the deposited nanolayers. The former case can be due to a decrease in deposited material along the gas flow direction, which is a consequence of the increase of the boundary layer thickness along the substrate surface. The change in the shape of the $MoSe_2$ flakes can be attributed to the MoO_3 concentration gradient that forms at the substrate surface, which results in a variation of the $Mo : Se$ ratio. Samples A to D were performed to prove that this concentration gradient existed, and the change in the morphology and amount of material deposited clearly shows the presence of these two effects.

The presence of a great number of small triangle domains that, in some samples, merge laterally to form an almost continuous film is an evidence of a high nucleation rate. Each triangle represents a nucleation site, showing that the mass transport rate is much slower than the surface reaction rate, resulting from a thick boundary layer. The growth process is similar to the columnar growth of thin films, where the thick pyramids indicate the sites of primary nucleation and the smaller thin triangles represent secondary nucleation sites. Hence, a lower nucleation rate should promote the growth of larger-area domains, with more uniform thickness. To lower the nucleation rate, the boundary layer thickness has to decrease in order for the mass transport rate be slightly higher than the surface chemical reaction. To reduce the boundary layer thickness, the gas flow rate has to be increased, which was demonstrated to result in a transition from an almost continuous film of small triangle domains, in sample 20, to isolated triangle islands of larger lateral sizes in sample 18.

Curiously, samples 15 and 20 have very similar morphologies, both of them with almost continuous films formed by small triangular domains. These domains were larger for sample 15, resulting in a higher PL response. The similarity between these two samples show that two completely different sets of deposition parameters can produce equivalent results. This indicates that the deposition parameters of a CVD experiment are not independent of each other, and that variations of different parameters can give rise to similar changes in the morphology of the samples. Furthermore, the results of samples 13 and 17, where no $MoSe_2$ was found on their surfaces, show that external parameters, which were not identified at the time of the deposition experiments, play an important role on the efficiency of the depositions, which lowers the reproducibility of results. The identification of these parameters is important to develop a reproducible experiment.

Sample 18 was the only one that had sufficiently large triangular domains capable of being visible by optical microscopy. Although they are bilayers, the deposition parameters used in this sample, together with the information obtained in the other samples, are a good starting point for the development of an experimental plan to attempt the deposition of $MoSe_2$ monolayers. This plan was defined, however, the breaking down of the heating element of the furnace after sample 20 forbid the execution of further experiments. It is expected to resume the experiments in a new furnace after its temperature profile is carefully studied.

First of all, the repetition of the experimental conditions of sample 18 with a higher gas flow rate is crucial to confirm the hypothesis previously stated, that a higher flow rate will allow the deposition of larger triangle domains. Two experiments, one with $\phi_{total} = 70sccm$ and another with $\phi_{total} = 80sccm$ are necessary to determine which flow rate promotes the growth of the larger layers. If both experiments give similar results, the use of a higher flow rate should allow the determination of the higher value of the total flow rate that enables the growth of low dimensional $MoSe_2$ under thermodynamic conditions. Using the gas flow rate that gave the best results, three studies with variations in the H_2 partial pressure are needed, since, in this work, it was not possible to determine which $H_2\%$ allowed the deposition of better quality layers. It is suggested the use of 5%, 10% and 15%, because they are between the values studied in this work, and so will provide more information about the influence of this parameter on the characteristics of the nanolayers produced.

Here, the influence of the substrate temperature on the morphology and quality of the samples produced was not studied. This study is important to determine if a substrate temperature of 790 °C is the factor responsible for the growth of bi- to few-layer structures, hindering the deposition of monolayers. Moreover, the variation in the temperature of MoO_3 powder requires further study, because it influences the rate of evaporation, thus, determining the amount of MoO_3 that exists in the vapour phase. This will change the concentration gradient of MoO_3 along the substrate surface during the deposition time. It is expected that its decrease will produce similar results to a decrease in MoO_3 powder mass. However, it would be interesting to perform an experiment where a lower MoO_3 temperature along with a higher growth time were used, to see if a slower evaporation of the MoO_3 molecules along with a high concentration of Se (due to the high powder mass) would promote the growth of larger-area triangles. Moreover, to confirm that the lateral growth of the layers deposited stop after 15 min of deposition time, as discussed in subsection 2.2.2, experiments with longer deposition times are needed, between 15min and 1hour.

To prevent the growth of the MoO_2 plates, that are thought to grow during the cooling process when the temperature is still high and no Se is present in the gas phase, a very high cooling flow rate could be used. If the flow rate is high enough (higher than $200sccm$), it could stop the reaction right away, hindering the deposition of further material, because the molecules in the gas phase would not have enough residency time to be adsorbed at the substrate surface.

Experiments performed with lower heating rates would also be important. Heating rates of $25\,°\mathrm{C}/min$ or $15\,°\mathrm{C}/min$ could allow the use of sapphire substrates which could be important for the PL study of the samples. A low heating rate could prevent the appearance of structural defects due to thermal strains on sapphire substrates. If this was the case, than the cooling process should be more controlled, by using temperature steps, to prevent the fast cooling of the sample.

The results obtained and the review of the literature presented in subsections 2.2.1 and 2.2.2, suggests that the presence of an uniform selenium atmosphere when the MoO_3 powder reaches the growth temperature is important to guarantee the formation of $MoSe_2$ right at the beginning of the growth process. In every experiment, the Se powder started to evaporate before the setpoint temperature of the furnace reached 800 °C, in order to guarantee the presence of selenium throughout the reactor tube before the growth temperature was reached. However, the heating flow rate used was very low, $\phi_{heating} = 5sccm$, and in every experiment it was observed that a large quantity of selenium moved upstream, being deposited on the walls of the quartz tube, as a consequence of the temperature gradient formed along the CVD reactor (Soret effect). Although it was observed the passage of selenium to the downstream side, its quantity was much lower than the observed at the upstream side. To avoid this, experiments with higher heating flow rates could be performed, such as $\phi_{heating} = 10sccm$ or $15sccm$.

As mentioned in subsection 3.1.1, the temperature at the selenium position increases over time, which changes the evaporation rate of the Se powder as the deposition time goes by, preventing the formation of a uniform supply of Se molecules to the gas phase. To guarantee that the temperature of the Se powder is constant over time and to control the exact moment when it starts to evaporate, an experimental setup where the selenium powder is heated independently of the heating of MoO_3 could be developed. An experimental setup of this kind would allow a more uniform concentration of selenium throughout the quartz tube, which would be responsible for a more uniform mixing of the precursor vapours at the substrate surface. Furthermore, if the amount of selenium powder used was enough, the cooling of the Se powder could be done after the temperature of MoO_3 decreased under a certain temperature to see if the presence of selenium during cooling would prevent the deposition of MoO_2 crystals, confirming that they grow during the cooling process.

In relation to the characterization of the samples, there are a few things that need further investigation. The observation of *holes* at the SiO_x surface and at the centre of the triangular domains in samples 8, 15, 18 and 20, which suggests that the layers grow around them, still needs an explanation. It was observed, by AFM, that these *holes* do not appear on the SiO_x surface in a pristine substrate, they are only observed at the surfaces of the samples. This could be due to hydrogen passivation during the growth process, due to dangling bonds on the oxide surface, but further investigation is needed. Moreover, the presence of small agglomerates at the edges of the nanolayers with a higher height than the thickness of the layers, seen in the AFM images, and the rough surface of the triangular layers on sample 18 still have an unknown origin. They could be due to the cleaning process after the cut of the samples to fit into the AFM holder, but further understanding of the chemical properties of the $MoSe_2$ nanolayers and the effects of 2-propanol on their properties needs to be made.

In this thesis, the oxidation of silicon substrates with three different SiO_x thickness was successfully achieved. The use of $\sim 90nm$ SiO_x/Si substrates was demonstrated to enable the visibility of the layers produced by optical microscopy. Unexpectedly, it was discovered that the SiO_x/Si substrates possessed a high intensity PL peak at $\sim 800nm$, for $\lambda_{ex} = 532nm$, at the same peak position as the values reported for the PL response of the $MoSe_2$ monolayers. Studies with different λ_{ex} showed that the PL peak of the SiO_x/Si substrates blueshifted linearly with the increase in excitation energy. It was determined that a $\lambda_{ex} = 514.5nm$ was more adequate for the study of the PL of the samples, because the high intensity PL peak appeared sufficiently shifted from $800nm$, to allow the access to the PL coming from the samples. Moreover, it was observed that increasing SiO_x thickness possessed lower PL intensity, for all the λ_{ex} used, suggesting that the deposition of $MoSe_2$ over $300nm$ SiO_x/Si substrates would enable a more accurate study of the PL signal of the low dimensional $MoSe_2$ samples. To undoubtedly determine the PL of the $MoSe_2$ samples, depositions onto sapphire or fused silica substrates could be performed.

To understand the origin of the PL from the SiO_x/Si substrates, the PL of amorphous silicon thin films deposited onto fused silica substrates by PLD was investigated. It was observed that these samples had PL peaks at the same peak positions as the SiO_x/Si substrates, but with lower intensity, for all of the λ_{ex} used. The same linear shift of the peak position with the increase in excitation energy was observed, and, for all excitation energies, the PL intensity decreased with the increase of the $a-Si$ thin film thickness. These results suggest that the PL comes from the silicon oxide-silicon interface. To confirm that this was not due to light emitters in the bulk silicon or in the bulk SiO_2, the PL of a pristine fused silica substrate and of a silicon thin film deposited onto MgO substrates were investigated. It was observed that the pristine fused silica substrate had a very low intensity peak at $\sim 800nm$, for $\lambda_{ex} = 532nm$, but no PL was detected for the other excitation energies. In the case of the $a-Si/MgO$ thin film, it was observed a completely different PL spectrum, very similar to the PL spectrum of the pristine MgO substrate. For this sample, no shift of the PL peaks was detected with the increase in excitation energy, and the only effect of the presence of the $a-Si$ thin film in the PL response of the sample is the decrease in PL intensity. These two results confirm that the PL is originated by states present in the interface SiO_x-Si. Although the discussion in subsection 4.1.2 attempts an explanation for the PL of these samples, further studies are needed to determine which states are responsible for the PL.

Bibliography

[1] K. S. Novoselov, A. K. Geim, S. V. Morozov, D. Jiang, Y. Zhang, S. V. Dubonos, I. V. Grigorieva, and A. A. Firsov. Electric field effect in atomically thin carbon films. *Science*, 306(5696):666–669, 2004.

[2] J. Xia, X. Huang, L. Liu, M. Wang, L. Wang, B. Huang, D. Zhu, J. Li, C. Gu, and X. Meng. Cvd synthesis of large-area, highly crystalline $MoSe_2$ atomic layers on diverse substrates and application to photodetectors. *Nanoscale*, 6:8949–8955, 2014.

[3] Q. H. Wang, K. Kalantar-Zadeh, A. Kis, J. N. Coleman, and M. S. Strano. Electronics and optoelectronics of two-dimensional transition metal dichalcogenides. *Nature nanotechnology*, 7(11):699–712, 2012.

[4] S. Larentis, B. Fallahazad, and E. Tutuc. Field-effect transistors and intrinsic mobility in ultra-thin $MoSe_2$ layers. *Applied Physics Letters*, 101(22), 2012.

[5] S. Das, H. Chen, A. V. Penumatcha, and J. Appenzeller. High performance multilayer MoS_2 transistors with scandium contacts. *Nano letters*, 13(1):100–105, 2012.

[6] Y. Chang, W. Zhang, Y. Zhu, Y. Han, J. Pu, J. Chang, W. Hsu, J. Huang, C. Hsu, M. Chiu, T. Takenobu, H. Li, C. Wu, W. Chang, A. T. S. Wee, and L. Li. Monolayer $MoSe_2$ grown by chemical vapor deposition for fast photodetection. *ACS Nano*, 8(8):8582–8590, 2014. PMID: 25094022.

[7] C. Jung, S. M. Kim, H. Moon, G. Han, J. Kwon, Y. K. Hong, I. Omkaram, Y. Yoon, S. Kim, and J. Park. Highly crystalline cvd-grown multilayer $MoSe_2$ thin film transistor for fast photodetector. *Scientific reports*, 5, 2015.

[8] M. Tsai, S. Su, J. Chang, D. Tsai, C. Chen, C. Wu, L. Li, L. Chen, and J. He. Monolayer MoS_2 heterojunction solar cells. *Acs Nano*, 8(8):8317–8322, 2014.

[9] M. Bernardi, M. Palummo, and J. C. Grossman. Extraordinary sunlight absorption and one nanometer thick photovoltaics using two-dimensional monolayer materials. *Nano Letters*, 13(8):3664–3670, 2013. PMID: 23750910.

[10] J. S. Ross, P. Klement, A. M. Jones, N. J. Ghimire, J. Yan, D. G. Mandrus, T. Taniguchi, K. Watanabe, K. Kitamura, W. Yao, D. H. Cobden, and X. Xu. Electrically tunable excitonic light-emitting diodes based on monolayer WSe_2 p-n junctions. *Nature nanotechnology*, 9(4):268–272, 2014.

[11] B. W. H. Baugher, H. O. H. Churchill, Y. Yang, and P. Jarillo-Herrero. Optoelectronic devices based on electrically tunable p-n diodes in a monolayer dichalcogenide. *Nature nanotechnology*, 9(4):262–267, 2014.

[12] H. Tang, K. Dou, C. Kaun, Q. Kuang, and S. Yang. $MoSe_2$ nanosheets and their graphene hybrids: synthesis, characterization and hydrogen evolution reaction studies. *J. Mater. Chem. A*, 2:360–364, 2014.

[13] Shun Mao, Zhenhai Wen, Suqin Ci, Xiaoru Guo, Kostya (Ken) Ostrikov, and Junhong Chen. Perpendicularly oriented $MoSe_2/Graphene$ nanosheets as advanced electrocatalysts for hydrogen evolution. *Small*, 11(4):414–419, 2015.

[14] X. Li, W. Cai, J. An, S. Kim, J. Nah, D. Yang, R. Piner, A. Velamakanni, I. Jung, E. Tutuc, S. K. Banerjee, L. Colombo, and R. S. Ruoff. Large-area synthesis of high-quality and uniform graphene films on copper foils. *Science*, 324(5932):1312–1314, 2009.

[15] J. Park, J. C. Park, S. J. Yun, H. Kim, D. H. Luong, S. M. Kim, S. H. Choi, W. Yang, J. Kong, K. K. Kim, and Y. H. Lee. Large-area monolayer hexagonal boron nitride on Pt foil. *ACS Nano*, 8(8):8520–8528, 2014. PMID: 25094030.

[16] Y. Lee, X. Zhang, W. Zhang, M. Chang, C. Lin, K. Chang, Y. Yu, J. T. Wang, C. Chang, L. Li, and T. Lin. Synthesis of large-area MoS_2 atomic layers with chemical vapor deposition. *Advanced Materials*, 24(17):2320–2325, 2012.

[17] S. Wang, Y. Rong, Y. Fan, M. Pacios, H. Bhaskaran, K. He, and J. H. Warner. Shape evolution of monolayer MoS_2 crystals grown by chemical vapor deposition. *Chemistry of Materials*, 26(22):6371–6379, 2014.

[18] S. Wang, M. Pacios, H. Bhaskaran, and J. H. Warner. Substrate control for large area continuous films of monolayer MoS_2 by atmospheric pressure chemical vapor deposition. *Nanotechnology*, 27(8):085604, 2016.

[19] J. C. Shaw, H. Zhou, Y. Chen, N. O. Weiss, Y. Liu, Y. Huang, and X. Duan. Chemical vapor deposition growth of monolayer $MoSe_2$ nanosheets. *Nano Research*, 7(4):511–517, 2014.

[20] X. Lu, M. I. B. Utama, J. L., X. Gong, J. Zhang, Y. Zhao, S. T. Pantelides, J. Wang, Z. Dong, Z. Liu, W. Zhou, and Q. Xiong. Large-area synthesis of monolayer and few-layer $MoSe_2$ films on SiO_2 substrates. *Nano Letters*, 14(5):2419–2425, 2014.

[21] X. Wang, Y. Gong, G. Shi, W. L. Chow, K. Keyshar, G. Ye, R. Vajtai, J. Lou, Z. Liu, E. Ringe, B. K. Tay, and P. M. Ajayan. Chemical vapor deposition growth of crystalline monolayer $MoSe_2$. *ACS Nano*, 8(5):5125–5131, 2014. PMID: 24680389.

[22] C. Cong, J. Shang, X. Wu, B. Cao, N. Peimyoo, C. Qiu, L. Sun, and T. Yu. Synthesis and optical properties of large-area single-crystalline 2d semiconductor WS_2 monolayer from chemical vapor deposition. *Advanced Optical Materials*, 2(2):131–136, 2014.

[23] J. Huang, J. Pu, C. Hsu, M. Chiu, Z. Juang, Y. Chang, W. Chang, Y. Iwasa, T. Takenobu, and L. Li. Large-area synthesis of highly crystalline WSe_2 monolayers and device applications. *ACS nano*, 8(1):923–930, 2013.

[24] B. Liu, M. Fathi, L. Chen, A. Abbas, Y. Ma, and C. Zhou. Chemical vapor deposition growth of monolayer WSe_2 with tunable device characteristics and growth mechanism study. *ACS nano*, 9(6):6119–6127, 2015.

[25] S. Tongay, J. Zhou, C. Ataca, K. Lo, T. S. Matthews, J. Li, J. C. Grossman, and J. Wu. Thermally driven crossover from indirect toward direct bandgap in 2d semiconductors: $MoSe_2$ versus MoS_2. *Nano Letters*, 12(11):5576–5580, 2012. PMID: 23098085.

[26] A. Bachmatiuk, R. F. Abelin, H. T. Quang, B. Trzebicka, J. Eckert, and M. H. Rummeli. Chemical vapor deposition of twisted bilayer and few-layer $MoSe_2$ over SiO_x substrates. *Nanotechnology*, 25(36):365603, 2014.

[27] S. Das, J. A. Robinson, M. Dubey, H. Terrones, and M. Terrones. Beyond graphene: Progress in novel two-dimensional materials and van der waals solids. *Annual Review of Materials Research*, 45:1–27, 2015.

[28] A. Kumar and P. K. Ahluwalia. Electronic structure of transition metal dichalcogenides monolayers 1h-MX_2 (m= mo, w; x= s, se, te) from ab-initio theory: new direct band gap semiconductors. *The European Physical Journal B*, 85(6):1–7, 2012.

[29] M. Chhowalla, H. S. Shin, G. Eda, L. Li, K. P. Loh, and H. Zhang. The chemistry of two-dimensional layered transition metal dichalcogenide nanosheets. *Nature chemistry*, 5(4):263–275, 2013.

[30] H. Zeng, J. Dai, W. Yao, D. Xiao, and X. Cui. Valley polarization in MoS_2 monolayers by optical pumping. *Nature nanotechnology*, 7(8):490–493, 2012.

[31] D. Xiao, G. Liu, W. Feng, X. Xu, and W. Yao. Coupled spin and valley physics in monolayers of MoS_2 and other group-vi dichalcogenides. *Physical Review Letters*, 108(19):196802, 2012.

[32] P. Johari and V. B. Shenoy. Tuning the electronic properties of semiconducting transition metal dichalcogenides by applying mechanical strains. *ACS nano*, 6(6):5449–5456, 2012.

[33] A. Kumar and P. K. Ahluwalia. Mechanical strain dependent electronic and dielectric properties of two-dimensional honeycomb structures of MoX_2 (x= s, se, te). *Physica B: Condensed Matter*, 419:66–75, 2013.

[34] K. He, C. Poole, K. F. Mak, and J. Shan. Experimental demonstration of continuous electronic structure tuning via strain in atomically thin MoS_2. *Nano letters*, 13(6):2931–2936, 2013.

[35] Y. Zhang, Y. Zhang, Q. Ji, J. Ju, H. Yuan, J. Shi, T. Gao, D. Ma, M. Liu, Y. Chen, X. Song, H. Y. Hwang, Y. Cui, and Z. Liu. Controlled growth of high-quality monolayer WS_2 layers on sapphire and imaging its grain boundary. *ACS Nano*, 7(10):8963–8971, 2013.

[36] Hugh O. Pierson. *Handbook of chemical vapor deposition: principles, technology and applications*. Noyes Publications, 1992.

[37] A. S. Pawbake, M. S. Pawar, S. R. Jadkar, and D. J. Late. Large area chemical vapor deposition of monolayer transition metal dichalcogenides and their temperature dependent raman spectroscopy studies. *Nanoscale*, 8:3008–3018, 2016.

[38] B. Li, Yo. Gong, Z. Hu, G. Brunetto, Y. Yang, G. Ye, Z. Zhang, S. Lei, Z. Jin, E. Bianco, X. Zhang, W. Wang, J. Lou, D. S. Galvão, M. Tang, B. I. Yakobson, R. Vajtai, and P. M. Ajayan. Solid–vapor reaction growth of transition-metal dichalcogenide monolayers. *Angewandte Chemie*, 128(36):10814–10819, 2016.

[39] M. Ohring. *The Materials Science of Thin Films*. Referex Engineering. Academic Press, 1992.

[40] A. G. Rajan, J. H. Warner, D. Blankschtein, and M. S. Strano. Generalized mechanistic model for the chemical vapor deposition of 2d transition metal dichalcogenide monolayers. *ACS Nano*, 10(4):4330–4344, 2016. PMID: 26937889.

[41] Baudouin Lecohier. *Etude et developpement de techniques de deposition selective du cuivre*. Ecole Polytechnique Federale de Lausanne, 1992.

[42] J.P. Mercier, G. Zambelli, and W. Kurz. *Introduction to Materials Science*. Series in applied chemistry and materials sciences. Elsevier Science, 2012.

[43] P. Blake, E. W. Hill, A. H. Castro Neto, K. S. Novoselov, D. Jiang, R. Yang, T. J. Booth, and A. K. Geim. Making graphene visible. *Applied Physics Letters*, 91(6), 2007.

[44] M. M. Benameur, B. Radisavljevic, J. S. Héron, S. Sahoo, H. Berger, and A. Kis. Visibility of dichalcogenide nanolayers. *Nanotechnology*, 22(12):125706, 2011.

[45] H. Li, J. Wu, X. Huang, Z. Yin, J. Liu, and H. Zhang. A universal, rapid method for clean transfer of nanostructures onto various substrates. *ACS nano*, 8(7):6563–6570, 2014.

[46] B. Li, Y. He, S. Lei, S. Najmaei, Y. Gong, X. Wang, J. Zhang, L. Ma, Y. Yang, S. Hong, J. Hao, G. Shi, A. George, K. Keyshar, X. Zhang, P. Dong, L. Ge, R. Vajtai, J. Lou, Y. J. Jung, and P. M. Ajayan. Scalable transfer of suspended two-dimensional single crystals. *Nano Letters*, 15(8):5089–5097, 2015.

[47] T. Roy, M. Tosun, J. S. Kang, A. B. Sachid, S. B. Desai, M. Hettick, C. C. Hu, and A. Javey. Field-effect transistors built from all two-dimensional material components. *Acs Nano*, 8(6):6259–6264, 2014.

[48] B. E. Deal and A. S. G. General relationship for the thermal oxidation of silicon. *Journal of Applied Physics*, 36(12):3770–3778, 1965.

[49] H. Z. Massoud, J. D. Plummer, and E. A. Irene. Thermal oxidation of silicon in dry oxygen accurate determination of the kinetic rate constants. *Journal of the Electrochemical Society*, 132(7):1745–1753, 1985.

[50] E. A. Lewis and E. A. Irene. The effect of surface orientation on silicon oxidation kinetics. *Journal of the Electrochemical Society*, 134(9):2332–2339, 1987.

[51] Nicoleta Popovici. *Oxide thin films for spintronics application growth and characterization*. PhD thesis, Faculdade de Ciências, Universidade de Lisboa, 2009.

[52] W. Melitz, J. Shen, A. C. Kummel, and S. Lee. Kelvin probe force microscopy and its application. *Surface Science Reports*, 66(1):1 – 27, 2011.

[53] C. Kittel. *Introduction to Solid State Physics*. Wiley, 2004.

[54] B.D. Cullity. *Elements of X-ray Diffraction*. Addison-Wesley series in metallurgy and materials. Addison-Wesley Publishing Company, 1978.

[55] Joint Committee on Powder Diffraction Standards, editor. *Powder Diffraction File*, ASTM, Philadelphia, PA, 1992.

[56] Pedro Sousa. *Chromium dioxide-low temperature thin film growth, structural and physical properties*. PhD thesis, Faculdade de Ciências, Universidade de Lisboa, 2008.

[57] P. Tonndorf, R. Schmidt, P. Böttger, X. Zhang, J. Börner, A. Liebig, M. Albrecht, C. Kloc, O. Gordan, D. R. T. Zahn, S. M. de Vasconcellos, and R. Bratschitsch. Photoluminescence emission and raman response of monolayer MoS_2, $MoSe_2$, and WSe_2. *Opt. Express*, 21(4):4908–4916, Feb 2013.

[58] G. W. Shim, K. Yoo, S. Seo, J. Shin, D. Y. Jung, I. Kang, C. W. Ahn, B. J. Cho, and S. Choi. Large-area single-layer $MoSe_2$ and its van der waals heterostructures. *ACS Nano*, 8(7):6655–6662, 2014. PMID: 24987802.

[59] D. Nam, J. Lee, and H. Cheong. Excitation energy dependent raman spectrum of $MoSe_2$. *Scientific Reports*, 5(17113), 2015.

[60] M. O'Brien, N. McEvoy, D. Hanlon, J. N. Coleman, and G. S. Duesberg. Mapping of low-frequency raman modes in cvd-grown transition metal dichalcogenides: Layer number, stacking orientation and resonant effects. *Scientific Reports*, 2016.

[61] Elisabete Rita. *Properties and local environment of p-type dopants and photoluminescent rare-earths implanted into zon single-crystals*. PhD thesis, Faculdade de Ciências, Universidade de Lisboa, 2008.

[62] S. S. Iyer and Y. H. Xie. Light emission from silicon. *Science*, 260(5104):40–46, 1993.

[63] T. Trupke, J. Zhao, A. Wang, R. Corkish, and M. A. Green. Very efficient light emission from bulk crystalline silicon. *Applied Physics Letters*, 82(18):2996–2998, 2003.

[64] A. G. Cullis, L. T. Canham, and P. D. J. Calcott. The structural and luminescence properties of porous silicon. *Journal of Applied Physics*, 82(3):909–965, 1997.

[65] M. V. Wolkin, J. Jorne, P. M. Fauchet, G. Allan, and C. Delerue. Electronic states and luminescence in porous silicon quantum dots: the role of oxygen. *Physical Review Letters*, 82(1):197, 1999.

[66] M. L. Brongersma, A. Polman, K. S. Min, E. Boer, T. Tambo, and H. A. Atwater. Tuning the emission wavelength of si nanocrystals in SiO_2 by oxidation. *Applied Physics Letters*, 72(20):2577–2579, 1998.

[67] M. L. Brongersma, A. Polman, K. S. Min, and H. A. Atwater. Depth distribution of luminescent si nanocrystals in si implanted SiO_2 films on si. *Journal of Applied Physics*, 86(2):759–763, 1999.

[68] K. Murakami, T. Suzuki, T. Makimura, and M. Tamura. Si nanocrystallites in SiO_2 with intense visible photoluminescence synthesized from SiO_x films deposited by laser ablation. *Applied Physics A*, 69(1):S13–S15, 1999.

[69] X. Wen, P. Zhang, T. A. Smith, R. J. Anthony, U. R. Kortshagen, P. Yu, Y. Feng, S. Shrestha, G. Coniber, and S. Huang. Tunability limit of photoluminescence in colloidal silicon nanocrystals. *Scientific reports*, 5, 2015.

[70] A. J. Kenyon, P. F. Trwoga, C. W. Pitt, and G. Rehm. The origin of photoluminescence from thin films of silicon rich silica. *Journal of Applied Physics*, 79(12):9291–9300, 1996.

[71] M. Molinari, H. Rinnert, and M. Vergnat. Visible photoluminescence in amorphous SiO_x thin films prepared by silicon evaporation under a molecular oxygen atmosphere. *Applied Physics Letters*, 82(22):3877–3879, 2003.

[72] A. S. Zyubin, Y. D. Glinka, A. M. Mebel, S. H. Lin, L. P. Hwang, and Y. T. Chen. Red and near-infrared photoluminescence from silica-based nanoscale materials: Experimental investigation and quantum-chemical modeling. *The Journal of chemical physics*, 116(1):281–294, 2002.

[73] F. T. Rabouw, N. M. B. Cogan, A. C. Berends, W. van der Stam, D. Vanmaekelbergh, A. F. Koenderink, T. D. Krauss, and C. de Mello Donega. Non-blinking single-photon emitters in silica. *Scientific reports*, 6, 2016.

[74] W. C. Choi, M. Lee, E. K. Kim, C. K. Kim, S. Min, C. Park, and J. Y. Lee. Visible luminescences from thermally grown silicon dioxide thin films. *Applied physics letters*, 69(22):3402–3404, 1996.

[75] A. A. Shklyaev, A. V. Gorbunov, and M. Ichikawa. Excitation-dependent blue shift of photoluminescence peak in 1.5–1.6 μm wavelength region from dislocation-rich si layers. In *2010 11th International Conference and Seminar on Micro/Nanotechnologies and Electron Devices*, pages 59–63. IEEE, 2010.

[76] L. Kumari, Y. Ma, C. Tsai, Y. Lin, S. Y. Wu, K. Cheng, and Y. Liou. X-ray diffraction and raman scattering studies on large-area array and nanobranched structure of 1d moo2 nanorods. *Nanotechnology*, 18(11):115717, 2007.

[77] B. B. Wang, K. Ostrikov, T. van der Laan, K. Zheng, R. Shao, M. K. Zhu, and S. S. Zou. Growth and photoluminescence of oriented $MoSe_2$ nanosheets produced by hot filament cvd. *RSC Adv.*, 6:37236–37245, 2016.

Appendix A

Table 5.1: **Raman and PL peaks of samples 5-20.** Raman peaks corresponding to $MoSe_2$ of the background of samples 5 to 20, plus the PL peak position and intensity for each sample.

			Raman peaks			Photoluminescence peaks		
Sample	E_{1g} (cm^{-1})	A_{1g} (cm^{-1})	E^1_{2g} (cm^{-1})	B^1_{2g} (cm^{-1})	$E^1_{2g} - A_{1g}$ (cm^{-1})	Peak position (nm)	FWHM	PL intensity (arb. units)
5	168.7	241.8	283.2	349.1	41.4	-	-	-
6	167.8	240.6	286.6	-	46.0	-	-	-
7	-	240.6	287.6	-	47.0	-	-	-
8	169.9	240.0	285.2	351.5	45.2	797	27	1.7×10^6
9	-	-	-	-	-	-	-	-
12	169.0	240.6	286.4	353.5	45.8	791	26	8.3×10^5
13	-	-	-	-	-	-	-	-
14	-	242.7	287.0	-	44.3	-	-	-
15	168.7	241.7	286.0	352.3	44.3	797	34	1.9×10^6
17	-	-	-	-	-	-	-	-
18	170.3	241.1	286.1	352.1	45.0	792	31	1.4×10^6
19	169.0	241.7	286.3	352.5	44.6	-	-	-
20	169.5	240.6	286.7	352.9	46.1	792	30	4.2×10^5

Appendix B

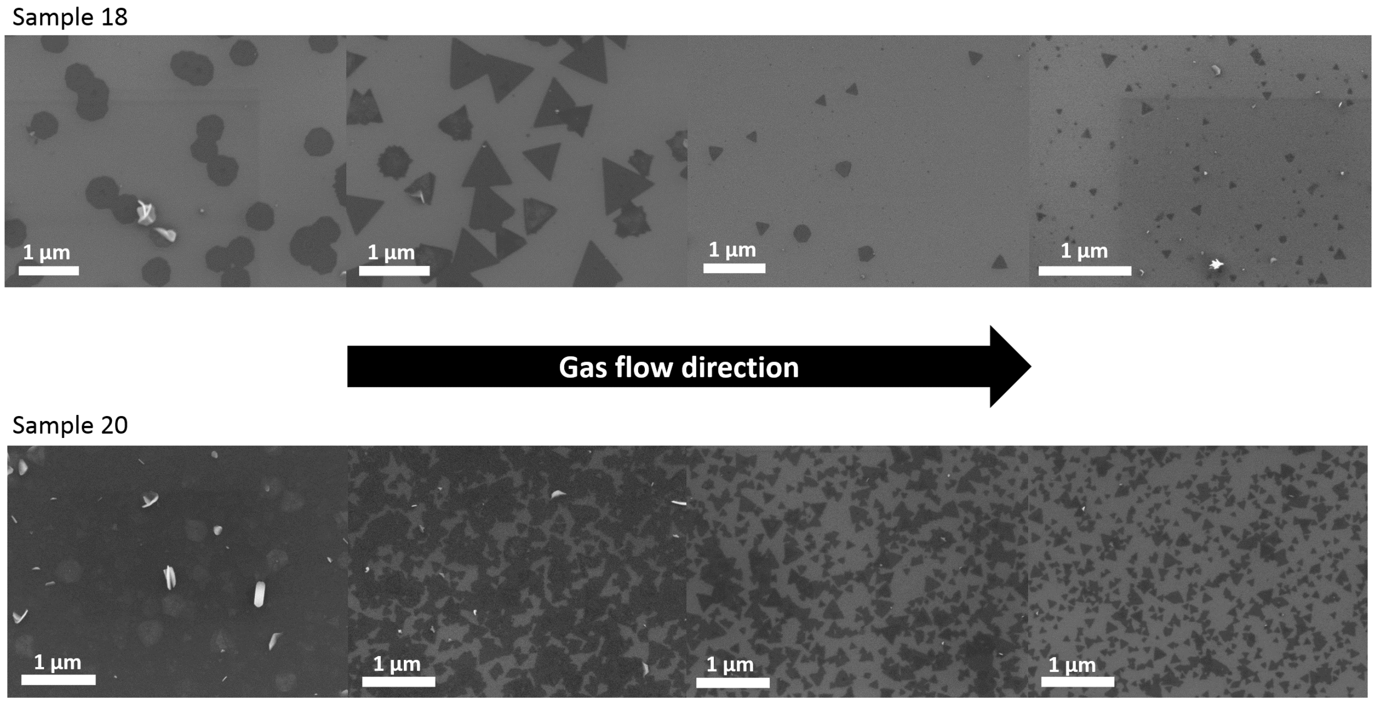

Figure 5.1: **Morphology evolution of deposited layers in samples 18 and 20.**